Impact of the Boundary Layer on Pointing and Tracking in Airborne Free-Space Laser Communication Links

by

Ross Aaron Conrad

B.S. Astronautical Engineering
United States Air Force Academy, 2006

Submitted to the Department of Aeronautics and Astronautics
in partial fulfillment of the requirements for the degree of

Master of Science in Aeronautics and Astronautics

at the

MASSACHUSETTS INSTITUTE OF TECHNOLOGY

June 2008

Author . . . .
Department of Aeronautics and Astronautics
June 6, 2008

Certified by. . . . .
Prof. John J. Deyst
Professor of Aeronautics & Astronautics
Thesis Supervisor

Certified by. . . . .
Dr. Jeffrey M. Roth
Technical Staff, MIT Lincoln Laboratory
Thesis Supervisor

Accepted by . . . .
Prof. David L. Darmofal
Associate Department Head, Chair, Committee on Graduate Students

Report Documentation Page

1. REPORT DATE	2. REPORT TYPE	3. DATES COVERED
01 JUN 2008	**N/A**	**-**

4. TITLE AND SUBTITLE	5a. CONTRACT NUMBER
Impact of the Boundary Layer on Pointing and Tracking in Airborne Free-Space Laser Communication Links	5b. GRANT NUMBER
	5c. PROGRAM ELEMENT NUMBER
6. AUTHOR(S)	5d. PROJECT NUMBER
	5e. TASK NUMBER
	5f. WORK UNIT NUMBER

7. PERFORMING ORGANIZATION NAME(S) AND ADDRESS(ES)	8. PERFORMING ORGANIZATION REPORT NUMBER
Massachusetts Institute Of Technology	**CI08-0020**

9. SPONSORING/MONITORING AGENCY NAME(S) AND ADDRESS(ES)	10. SPONSOR/MONITOR'S ACRONYM(S)
The Department of the Air Force AFIT/ENEL, Bldg 16 2275 D Street WPAFB, OH 45433	11. SPONSOR/MONITOR'S REPORT NUMBER(S)

12. DISTRIBUTION/AVAILABILITY STATEMENT

Approved for public release, distribution unlimited

13. SUPPLEMENTARY NOTES

The original document contains color images.

14. ABSTRACT

15. SUBJECT TERMS

16. SECURITY CLASSIFICATION OF:			17. LIMITATION OF ABSTRACT	18. NUMBER OF PAGES	19a. NAME OF RESPONSIBLE PERSON
a. REPORT	b. ABSTRACT	c. THIS PAGE	**UU**	**119**	
unclassified	**unclassified**	**unclassified**			

Impact of the Boundary Layer on

Pointing and Tracking in Airborne

Free-Space Laser Communication Links

by

Ross Aaron Conrad

Submitted to the Department of Aeronautics and Astronautics
on June 6, 2008, in partial fulfillment of the
requirements for the degree of
Master of Science in Aeronautics and Astronautics

Abstract

Free-space laser communication is a developing technology with enormous potential to revolutionize the way people communicate across the globe. Of specific interest are air-to-space lasercom links. Such a link experiences atmospheric scintillation, platform jitter, and boundary layer turbulence. This research investigated the tracking challenge using a focal plane array sensor with centroid and peak tracking algorithms. Also investigated was the use of a deformable mirror to recreate optical phase distortions from boundary layer turbulence. Experiments were conducted with realistic channel effects for multiple look angles between a subsonic aircraft at 29 kft and geosynchronous satellite. Performance was determined by power delivered to an optical fiber. The results show that the two tracking algorithms can differ by up to one decibel of fiber power, with centroid tracking generally performing best. Conclusions are highly dependent on aircraft and spacecraft parameters but point towards centroid tracking for maximizing received power.

Keywords: Lasercom, FPA Tracking, Boundary Layer Disturbances, Deformable Mirror

Thesis Supervisor: Prof. John J. Deyst
Title: Professor of Aeronautics & Astronautics

Thesis Supervisor: Dr. Jeffrey M. Roth
Title: Technical Staff, MIT Lincoln Laboratory

Acknowledgments

This work would not have been possible without the help of the fine people in Group 66, Advanced Lasercom Systems and Operations, at MIT Lincoln Laboratory. I would like to thank my advisors Jeffrey Roth and John Deyst who helped guide and counsel me throughout my research. Also essential were Bill Wilcox who helped with computer and networking issues, Tim Williams who tirelessly checked the alignment of the Tracking Testbed optics before my experiments, Steven Michael who developed the fade and boundary layer time series, and Bob Murphy who designed & understands the tracking system inside-out. I am very grateful to all of them for sharing their time and their expertise.

Contents

List of Figures

12

List of Tables

Chapter 1

Introduction

Overview

Free-space laser communication is a developing technology with enormous potential to revolutionize the way people communicate across the globe. Immense data rates are possible using infrared wavelengths that are not subject to the same frequency allocation restrictions present at radio wavelengths. These shorter wavelengths also offer power savings and increased security due to their narrow beamwidth. Laser terminals can be located on any platform, including space vehicles, aircraft, ships, and ground stations, enabling a high speed network without the cabling and large antennas required today by fiber optic and radio frequency (RF) systems. This chapter will describe the problem being investigated and the scope of this thesis.

1.1   Problem

A free-space laser communication link, commonly referred to as lasercom, is being investigated as a successor to RF technology on airborne and space-based platforms. A lasercom link between an aircraft and spacecraft would allow for rapid flow of information from sensors to users. This link is unique, because in addition to platform jitter and atmospheric scintillation, there are disturbances caused by an aircraft's boundary layer. The boundary layer causes the air to have a time varying index of refraction

which imparts a nonuniform, dynamic phase disturbance across a wavefront. These phase disturbances are especially pronounced on a transmitted optical beam due to its short wavelength. The disturbances tax a lasercom terminal's tracking system and reduce received power into a single-mode optical fiber. This thesis will investigate the boundary layer phenomenon for a hemispherical terminal geometry and ways to mitigate its effect on communication and link stability through tracking.

1.2 Scope of work

The work presented here explores two methods of focal plane tracking for a wide range of look angles and turbulence conditions, realistic to a lasercom link between an airborne and geostationary orbiting (GEO) satellite. All results and conclusions are based on experiments conducted using MIT Lincoln Laboratory's Tracking Testbed. The testbed is capable of realistically recreating the disturbances a propagating optical beam experiences, including fading, jitter, round trip delay, and phase distortions. Also included is work done on the replication of boundary layer turbulence using a deformable mirror to induce phase distortions on an optical wavefront. This method provides a way of exploring in the laboratory the effect of an aircraft boundary layer on a lasercom system. Background information on the optical channel and testbed, as well as a complete discussion of the experimental results is also provided.

Summary

Free-space lasercom in the atmospheric environment is a challenge further complicated by an aircraft's boundary layer. The potential benefits of lasercom, especially high data rates, make the technology notably desirable for an air-to-space link. This chapter provided an outline of the problem that is to be answered by this research and the scope of the investigation. The following chapters will delve deeper to provide background on the problem, describe the laboratory testbed which the experiments were conducted with, and explain the results of those experiments.

Chapter 2

Background

Overview

Lasercom between space-based and airborne platforms has a tremendous amount of complexity. This chapter aims to provide background information in key areas and explain how they relate to the experimentation. Key areas that will be discussed include lasers, channel effects such as atmospheric scintillation and jitter, boundary layer disturbances, and establishing a lasercom link.

2.1   History of Lasercom

As an emerging technology, free-space laser communication is being researched by government agencies and industry. Several government funded programs have built experimental lasercom terminals to test the readiness of the technology. The Geosynchronous Lightweight Technology Experiment (GeoLITE) program was a laser communications experiment launched by the National Reconnaissance Office. Another program, the Airborne Laser Experiment (ALEX), provided an airborne terminal that looked out a conformable window on an aircraft. GeoLITE and ALEX were successful in demonstrating space-to-ground and space-to-air lasercom links.

Building on the success of these two programs, the Air Force's Transformational Satellite (TSAT) program is investigating laser terminals for use as geosynchronous

crosslinks and for links with high-flying airborne assets. This next generation constellation will use lasercom as a long-haul backbone at speeds of 10–40 gigabits per second (Gb/s). For comparison, the current MILSTAR II constellation takes about 2 minutes to transmit a 24-megabyte, high-resolution image; at 10 Gb/s it would take a fraction of a second. This system is being designed to provide 20–50 simultaneous airborne users with rapid connectivity via lasercom links, as well as 8000 conventional RF links for lower data rate users [10].

The natural inclination is to expand this technology beyond space and deeper into the atmospheric environment. Short distance ground-to-ground systems are commercially available, often used for connecting buildings in urban environments where installing conventional fiber connections is too costly [17]. Research continues to be conducted in all aspects of lasercom technology, both by government funded research and private enterprise.

2.2   Lasers

The characteristics unique to the laser are what make a free-space laser communication system possible. During propagation through the atmosphere, light encounters obstacles that can change its intensity, phase, wavelength, and polarization. Using a laser light source, many of these challenges are reduced because of its characteristics of monochromaticity, coherence, and directionality.

The property of monochromaticity is most easily defined as meaning that the light has one color, a uniform wavelength. Laser light is produced through the process of stimulated emission, which produces photons of nominally identical frequencies. To a much smaller degree, randomly phased spontaneous emissions may also exit the laser output mirror. The nominal frequency therefore acquires additional frequencies resulting in what is called the Schawlaw-Townes linewidth, a measure of the monochromaticity of light. Mechanical vibration of the laser cavity can alter its length and changes in pressure or temperature can vary the index of refraction of the gain medium. These mechanisms work to change the emitted frequency from

the laser cavity [16, 5]. The narrow linewidth of laser light allows for several closely spaced frequencies to be used simultaneously, greatly increasing the amount of data transfered over a link. The spacing of these frequencies must allow room for spectral broadening that occurs from modulating the carrier with a high-rate data signal, as well as the effects just described.

Also notable to the laser is its degree of coherence. Coherence is a measure of the degree of phase correlation that exists in the radiation field of a light source at different locations and times. Coherence consists of two components: spatial and temporal. Spatial coherence is a measure of the phase uniformity across an optical wavefront whereas temporal coherence is a measure of the degree of monochromaticity of the light. If both are known, a confident prediction of the phase at any point within the laser's coherence length can be determined, given the phase at a specific time and place. Laser light has a phase, energy, direction, and polarization identical to that of the amplified light wave in the laser cavity. Thus, the emitted light is both temporally and spatially coherent. After long propagation distances, the wavefront can be assumed planar and in-phase as shown in Figure 2-1, ideal for carrying encoded data.
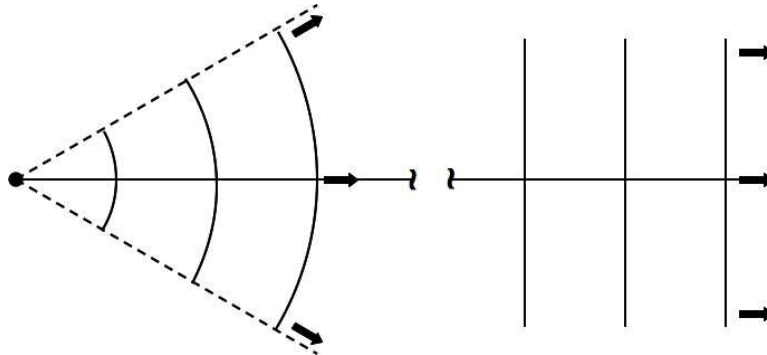
Figure 2-1: Light emitted from a coherent source (laser) can be assumed to have a planar wave and phase front once sufficiently far from the source.

Directionality is a measure of how well a light source's energy can be directed. A laser has very small angular spread, evident from its well-defined beam. This means that a laser's irradiance, the power per unit area, is very high. As a result, the transmit powers in a laser communication system can be relatively moderate

compared to RF sources. A typical communication beam has an angular spread of 10 μrad which spreads to only a few hundred meters over the distance from the Earth to geosynchronous orbits. Laser light can also be pulsed at rates unachievable in RF, allowing for multi-Gb/s data encoding. The properties of monochromaticity, coherence, and directionality set lasers apart from other light sources and are exactly what is needed for a free-space optical communication system.

2.3   Channel Effects

The channel that free-space lasercom occurs over is not benign. Platform disturbances, the atmosphere, weather, and distance all affect the ability to sustain a stable link. Figure 2-2 shows all of the disturbances added to the channel within the Tracking Testbed. This section will describe each disturbance and its effect on an optical beam.
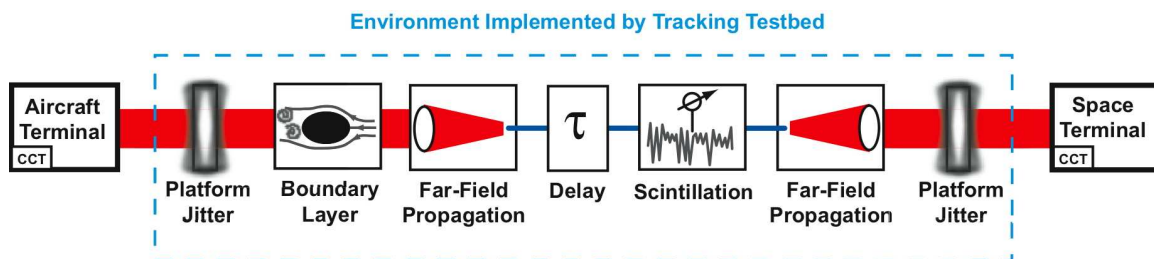
Figure 2-2: Illustration of the channel environment implemented by the Tracking Testbed.

2.3.1   Platform Jitter

No platform is completely free of vibration, which causes jitter on a transmitted beam. On a satellite, sources of vibration include thrusting operations, solar array movements, momentum wheels, and pointing motors. For an aircraft terminal, vibration derives from steering motors, aircraft engines, hydraulic systems, and atmospheric turbulence. Even terrestrial based terminals will experience unwanted vibration (e.g., building sway, construction, ventilation fans). When precise pointing

is required, suppression of vibration and compensation for jitter are imperative to enable effective link pointing, acquisition, tracking, and error-free transmission [25].

Jitter can be characterized through measurements made on actual platforms. Using an inertial sensor as a detector, a fast steering mirror is often able to compensate for the resulting pointing errors. A terminal may also be situated such that it is isolated from the majority of platform vibration by damping mounts. The remaining jitter on the beam is known as residual jitter and it affects pointing accuracy during both the acquisition process and tracking.

2.3.2 Atmospheric Scintillation & Absorption

Atmospheric disturbances have a tremendous impact on a lasercom signal. If the atmosphere was a homogeneous medium, with time-invariant optical properties, communication through it would be simple. In reality the presence of temperature gradients leads to local density variations that act like lenses to disperse and refract light from the laser beam, causing intensity variations across the beam width.

The atmosphere consists of many molecules that can absorb light, causing loss to an optical signal. Figure 2-3 shows the absorption properties of common molecules in the atmosphere, carbon dioxide and water being the largest absorbers at laser wavelengths. The wavelength chosen for free-space lasercom is 1.55 μm due to its low absorption. Conveniently, many commercial off the shelf (COTS) optical components are available at this wavelength, driving down costs.

As may be expected, atmospheric fading due to scintillation is dependent on altitude and elevation angle. Scintillation has the effect of non-uniformly diffracting the beam, causing fading, and is what causes stars to twinkle at night. This effect is most pronounced at small elevation angles and low altitudes where an optical signal has to propagate a greater distance within the atmosphere. Figure 2-4 shows the convention that will be used to describe the look angle from an aircraft. Azimuth and elevation angles are positive as drawn, and the origin is located at the optical terminal.

Atmospheric effects become more pronounced for low-altitude aircraft and ground-based terminals due to increased atmospheric density and weather [21]. Weather ef-
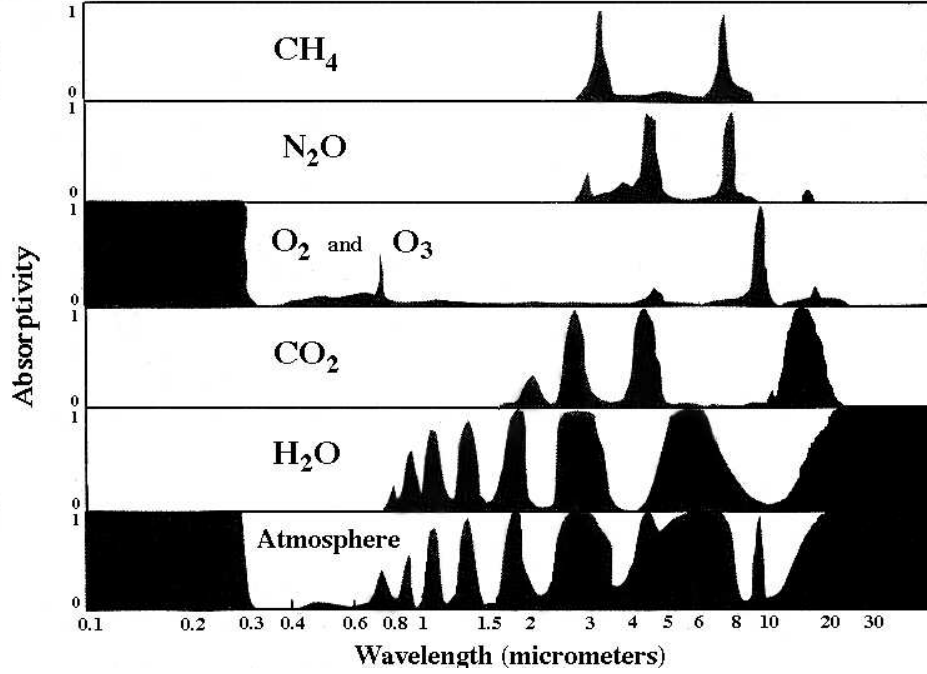
Figure 2-3: Absorptivity vs. wavelength within the atmosphere for several common molecules, zero meaning no absorption and one meaning total absorption. Light at $\lambda = 1.55~\mu m$ experiences minimal absorption.

fects, such as clouds, fog, and precipitation contribute to signal power fading through scattering and absorption [22]. This is a compelling reason to initially demonstrate lasercom between a high-flying aircraft and a satellite well above the horizon, minimizing the atmospheric path-length.

Propagation of laser light through the atmosphere can be simulated to produce a time series of received power for a range of look angles and altitudes. The experiments in this thesis utilized previously generated time series of atmospheric scintillation for multiple elevation angles. Although fading might not be uniform across the beam aperture, in these experiments it is assumed that the aperture size is small compared to the atmospheric fluctuations, meaning the beam experiences uniform fading. It is also assumed that there are no phase distortions from fading.

Steven Michael at MIT Lincoln Laboratory (LL) created the scintillation time series used in these experiments with a time dependent wave optics code developed at LL called Parallel Optical Propagation Software (POPS) [15]. This software discretizes the atmosphere into a series of independent phase screens. These phase

26
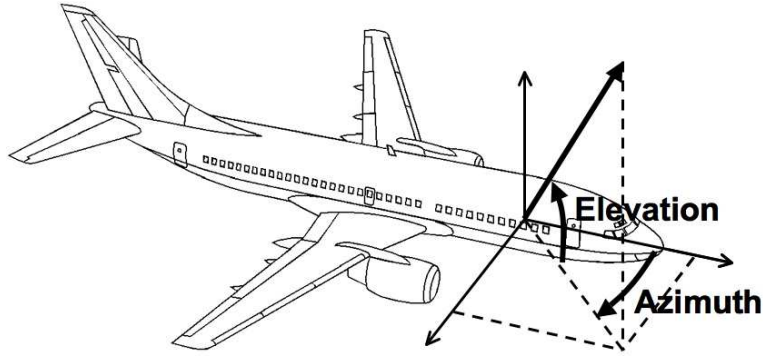
Figure 2-4: Illustration of direction convention for look angle azimuth and elevation.

(a) Light, 45 deg   (b) Moderate, 20 deg   (c) Heavy, 10 deg
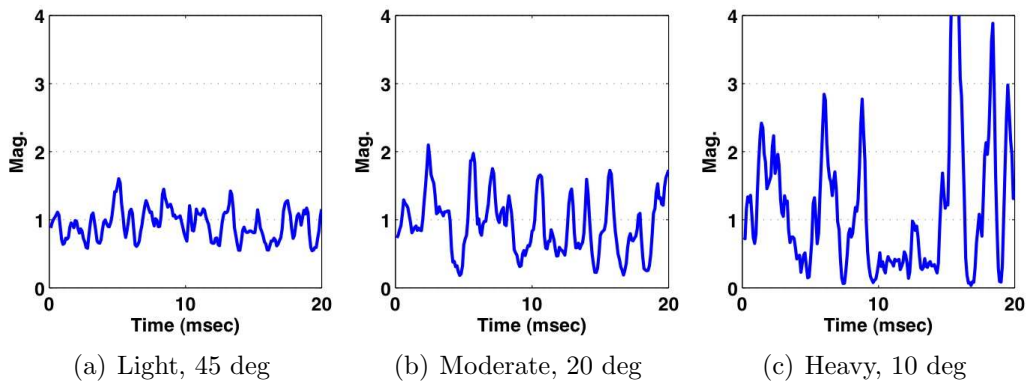
Figure 2-5: Fading magnitudes for three test elevation angles showing increased fluctuation with decreased elevation.
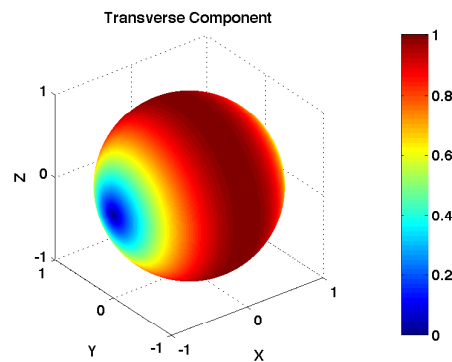
Figure 2-6: Illustration of transverse component of velocity for aircraft traveling along x-axis.

screens are based on the Kolmogorov model, which describes the nature of atmospherically induced perturbations to a wavefront. Between each screen is a vacuum that a Gaussian beam is sent through. When the beam encounters a screen, the beam is convolved with the Green's function for a paraxial radiator. The effect of wind can be added to the simulation by having various phase screens shift position over time. The magnitude of the fading is a function of the turbulence strength which can be adjusted in the simulation. The resultant 15-sec long scintillation time series used in these experiments accurately model the fading a beam would experience while propagating through the atmosphere. Figure 2-5 shows how the magnitude of fading increases as elevation angle decreases.

Fading on a moving platform also varies with azimuth. The time scale of the scintillation will be at a minimum when viewed perpendicular to the aircraft's motion because the channel is rapidly passing through different pockets of atmosphere. As the look angle moves forwards or backwards, the time scale of these disturbances increases. The transverse component (v_t) of the aircraft's velocity (v_0) is defined by Equation 2.1 for elevation (θ) and azimuth (ϕ) angles; Figure 2-6 illustrates the transverse component's magnitude over a unit sphere. This is a simplified description of the atmospheric fading a moving platform sees (e.g., neglects ambient wind speed) but serves the purposes of these experiments.

$$v_t = v_0[cos^2(\phi)sin^2(\theta) + sin^2(\phi)]^{\frac{1}{2}} \tag{2.1}$$

2.3.3 Propagation Delay

Even though communicating at the speed of light, there is propagation delay due to the great distances traveled through free-space. The delay can be significant when the link includes a geosynchronous Earth orbiting (GEO) satellite. Equations 2.2-2.5 show the calculation of round-trip propagation delay for an aircraft (A/C)-to-GEO link (ω = angular velocity, T = orbital period, r = orbital radius, d = propagation distance).

28

$$\omega_{GEO} = \frac{2\pi}{T} = \frac{2\pi}{86164 \; sec} = 7.292 \cdot 10^{-5} \; rad/sec \tag{2.2}$$

$$r_{GEO} = \sqrt[3]{\frac{\mu}{\omega_{GEO}^2}} = \sqrt[3]{\frac{3.986 \cdot 10^{14}}{(7.292 \cdot 10^{-5})^2}} = 42165 \; km \tag{2.3}$$

$$d = r_{orbit} - r_{earth} - h_{aircraft} = 42165 \; km - 6371 \; km - 10 \; km = 35784 \; km \tag{2.4}$$

$$t_{delay_{GEO}} = \frac{2 \cdot d}{v} = \frac{2 \cdot 35784 \; km}{3 \cdot 10^5 \; km/sec} \approx 0.24 \; sec \tag{2.5}$$

This 0.24 sec delay must be accounted for by using a point ahead mirror (PAM); otherwise, the sent signal would miss the target due to the small beamwidth and high relative velocity of these platforms. When a satellite is in a low earth orbit (LEO) this delay is much less. A LEO satellite may orbit at an altitude of $\sim$ 300 km. The propagation delay in this case, as calculated in Equation 2.6, may be as little as 40 msec if the satellite is directly overhead. The consequence of the lessened delay is that the relative velocity difference is much greater for A/C-LEO links, which will still require point-ahead compensation.

$$t_{delay_{LEO}} = \frac{2 \cdot d}{v} = \frac{2 \cdot 300 \; km}{3 \cdot 10^5 \; km/sec} \approx 40 \; msec \tag{2.6}$$

2.4   Boundary Layer

Boundary layer turbulence around the aircraft also affects the optical beam. Although seemingly similar to scintillation-induced fading, boundary layer effects pose unique challenges in air-to-space and air-to-air lasercom links. The boundary layer phenomenon, also known as aero-optics, refers to the wavefront distortion of a uniform plane wave propagating through turbulence [3, 20, 26]. The turbulence induced air density fluctuations result in variations in the index of refraction, which cause the

effective path length to vary across the beam width. Because the wavelength of laser light is short, 1.55 μm in these experiments, small variations in optical path length can create significant phase distortions across the aperture. These distortions cannot be corrected with inertial sensing. There is no power loss due to the phase distortions.

2.4.1 Turret Shape

In the case of a space-to-air transmission, the signal passes through the boundary layer once. For air-to-air, there are transitions through two boundary layers, meaning that a previously distorted wavefront will be further distorted. Careful design and placement of the optical terminal can minimize the effect of these distortions. In a typical sub-sonic configuration, compressible airflow moves over the aircraft and optical terminal. This terminal may be contained in either a dome mounted on top of the fuselage, within a wing-mounted pod, or behind a window that is conformal to the aircraft fuselage. If the terminal is intended to communicate with satellites, its field-of-regard (FOR) should include the entire sky, while allowing normal flight operations of the aircraft. If the terminal is intended to communicate with other aircraft or ground assets, its design should provide for an unobstructed FOR in all directions. Figure 2-7 illustrates four turret designs that might be considered for a lasercom aircraft terminal.
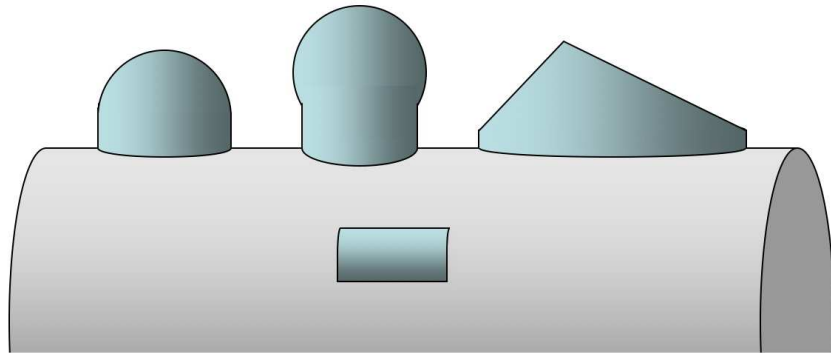
Figure 2-7: Illustration of four turret designs for an airborne lasercom terminal.

In a window configuration a glass window is mounted flush with the skin of the aircraft and the terminal looks through it. This setup does not cause any additional

disturbances to the boundary layer turbulence, but at the cost of a limited FOR per terminal. To have a clear view of the sky, several of these terminals would have to be positioned around the aircraft to provide required intervisibility with adjacent lasercom stations. This configuration increases system complexity but minimizes impairments due to boundary layer effects. The Lasercom Airborne Flight Test System (AFTS) used a conformal window to demonstrate air-to-ground lasercom [9].

A dome configuration offers a much greater FOR but induces turbulence. A glass dome mounted on top of an aircraft fuselage with a beam director located at the center of curvature allows a single laser terminal to see the entire overhead sky. A hyper-hemispherical dome on a cylindrical pedestal allows an even greater FOR for elevations at or below the horizon. While this is a desirable shape for maximum FOR, it is a very undesirable shape for aerodynamics, creating a lot of turbulence. Flow over the front of the dome is fairly uniform but it then becomes detached and turbulent as it travels over the rest of the dome (see Figure 2-11) [6]. Due to the turbulent nature of the air, the induced phase change is time variant and presents a challenge to the dome configuration [3]. Adaptive optic correction is one possible option but complicates the communication system, increasing size, weight, and power (SWaP) [13].

An alternative is to try different enclosure shapes to find out if there is an optimum geometry that minimizes phase distortions. A cone shaped enclosure with a flat window has been discussed, along with terminals within streamlined wing-mounted pods. A small aperture size is desirable as this will minimize the size of the enclosure, but it comes at the cost of reducing received power. It is unlikely that aero-optic effects can be completely avoided in this problem.

2.4.2   Computational Fluid Dynamics

To explore the nature of the boundary layer further, Lincoln Laboratory has managed several trade studies to create computational fluid dynamics (CFD) simulations of different dome locations and shapes on several aircraft. Lockheed Martin looked at mounting a dome on the Air Force's U-2 reconnaissance airframe. The two lo-
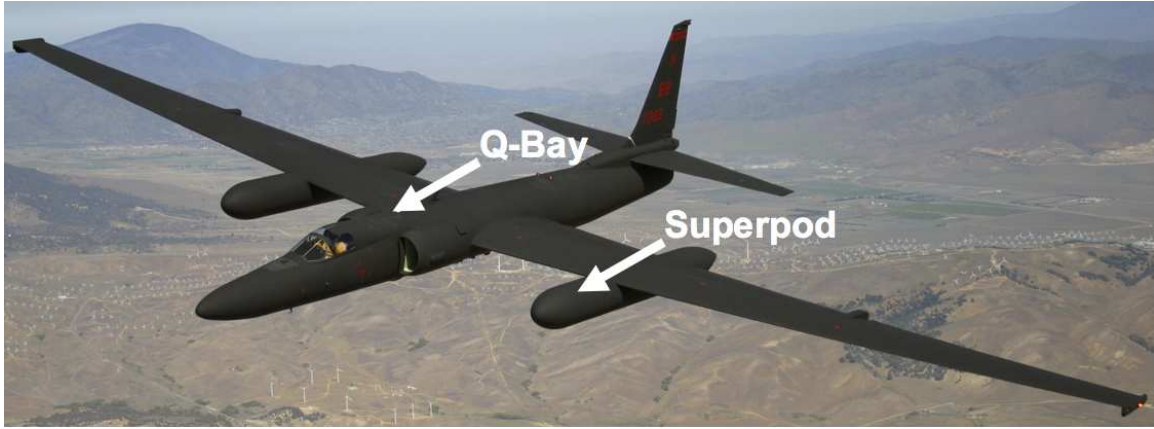
Figure 2-8: Potential lasercom terminal locations on a U-2 reconnaissance aircraft [8].
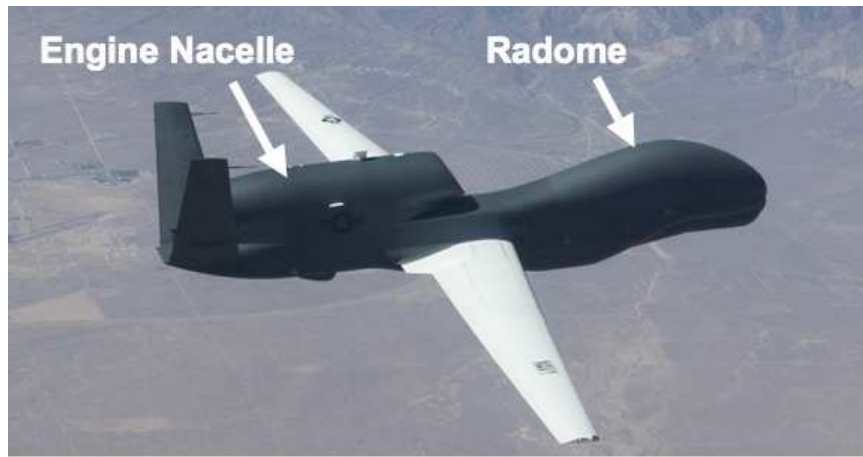
Figure 2-9: Potential lasercom terminal locations on a Global Hawk unmanned aerial vehicle [14].

cations considered were on the top of a super-pod, a torpedo shaped pod mounted beneath the wing, and on the Q-bay, an area behind the cockpit where sensors are commonly located. Northrop Grumman conducted similar simulations on the Global Hawk unmanned aerial vehicle (UAV), positioning a dome on its radome and engine nacelle. These locations are labeled for the U-2 and Global Hawk in Figures 2-8 & 2-9, respectively.

The CFD and aero-optical analysis trade studies have been used to investigate the transmission of a laser beam through the aerodynamic flow-field around a turret/airframe combination. Of specific interest are high frequency phase aberrations and tip/tilt jitter induced by the boundary layer. Due to the computationally inten-

sive calculations involved, these trade studies produced data for a simplified geometry that was only 80 msec in duration. While shorter than desired, the data provides a starting point for experimentation.

This short length of data is useful in showing the degree of boundary layer turbulence for a given look angle. Statistical models of the boundary layer would require much longer simulation times due to their many variables, such as altitude, velocity, dome geometry, and look angle. With greater processing power it may be possible to generate statistics for a specific set of conditions, but the computational investment is too great to accomplish this task in a timely period. Future use of the LL Grid, a multi-node high performance computing center at Lincoln Laboratory, may make this possible [1].

For the research reported here, CFD data produced by Lockheed Martin–Fort Worth, TX was used. The data models flow over a hyperhemispherical dome mounted on a cylindrical fuselage. This simulation uses realistic conditions for an airborne optical terminal: 16-in diameter dome, altitude of 29 kft, speed of Mach 0.7. Snapshots of the flowfield for this configuration are shown in Figures 2-10 and 2-11.

This geometry creates a quasi-static turbulence area in front of the dome, a transonic area to the top and sides, which then transitions rapidly to a very turbulent area to the rear of the dome where large eddies are created in the downstream flow. Figure 2-12 shows slices of density in the dome's wake. The dome is not an ideal geometry for minimizing phase distortions but favorable for maximizing terminal FOR. Success of this setup depends on the terminal's tracking system, to see if the beam received at the aperture is suitable for tracking.

2.4.3   Optical Effect

Boundary layer turbulence causes variations in atmospheric density which alter the air's index of refraction in a nonuniform manner across the aperture. The index of refraction determines the speed at which light is transmitted through a medium. Variations in this parameter effectively change the propagation distance and thus the phase of the light.

(a) Side View   (b) Top View
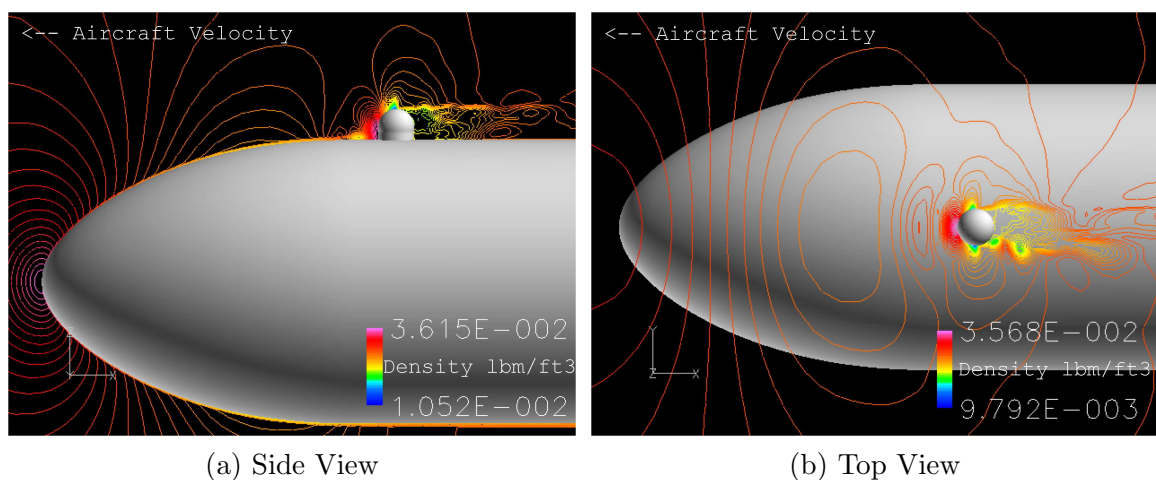
Figure 2-10: Density contours around a 16-in diameter hyper-hemispherical turret on a fuselage at 29 kft, Mach 0.7 (lbm/ft^3).

(a) Side View   (b) Top View
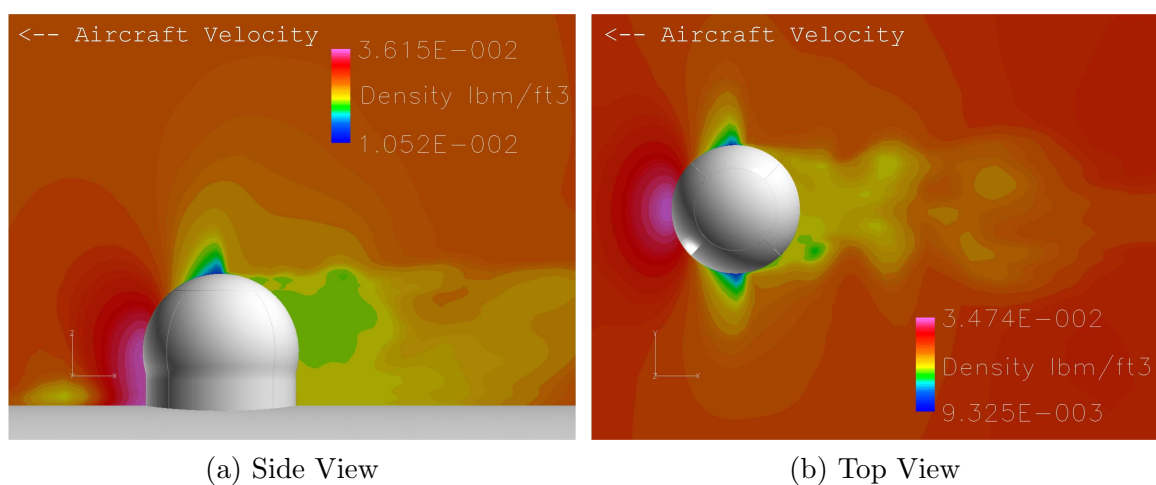
Figure 2-11: Magnified view of density field around a 16-in diameter hyper-hemispherical turret on a fuselage at 29 kft, Mach 0.7 (lbm/ft^3).
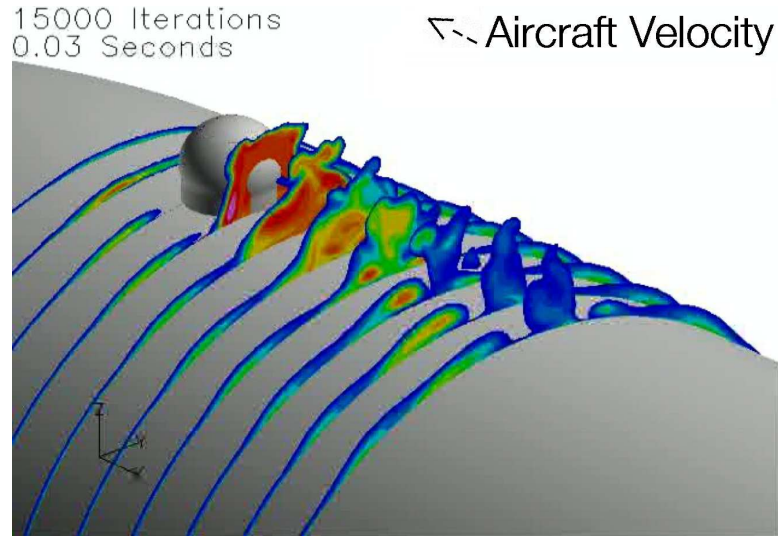
Figure 2-12: Slices showing downstream density fluctuations caused by a hyper-hemisphere turret configuration.

The optical path distance (OPD) can be calculated across an aperture from the CFD results. First, a look angle and aperture size are chosen. Next, a cylinder with the aperture diameter and orientation of the look angle is placed into the CFD mesh. This cylinder represents the path that a beam travels through. Finally, an aperture resolution is chosen and the density is integrated over the length of the cylinder. This result gives the effective OPD across the aperture. The process is then repeated for each time step to create a time series of OPD variations for look angle and aperture size.

2.5 Pointing, Acquisition, and Tracking

Establishing a laser communication link between a spacecraft and aircraft is no small feat. Work from previous lasercom programs has led to field-proven methods of acquiring another lasercom terminal and tracking it. This section will discuss a notional method for establishing an air-to-space link, followed by a discussion of the pointing and tracking challenges inherent to lasercom.

2.5.1 Establishing a Link

This paragraph will discuss a notional acquisition sequence. The first step in establishing a link is for an aircraft terminal to scan a wide-angle beacon beam, labeled as the acquisition beam in Figure 2-13, towards the calculated position of the spacecraft terminal. Once the spacecraft detects the acquisition beam, it returns a narrow downlink beam in the direction of the aircraft, accounting for point-ahead offset due to the motion between platforms. The aircraft terminal then detects the spacecraft downlink beam, stops scanning, and points a stable beacon beam at the spacecraft. If a stable return is received from the spacecraft, the aircraft turns on its narrow uplink beam. Both terminals now track to each other's narrow beam, which will be used for communication. Figure 2-13 illustrates this process.
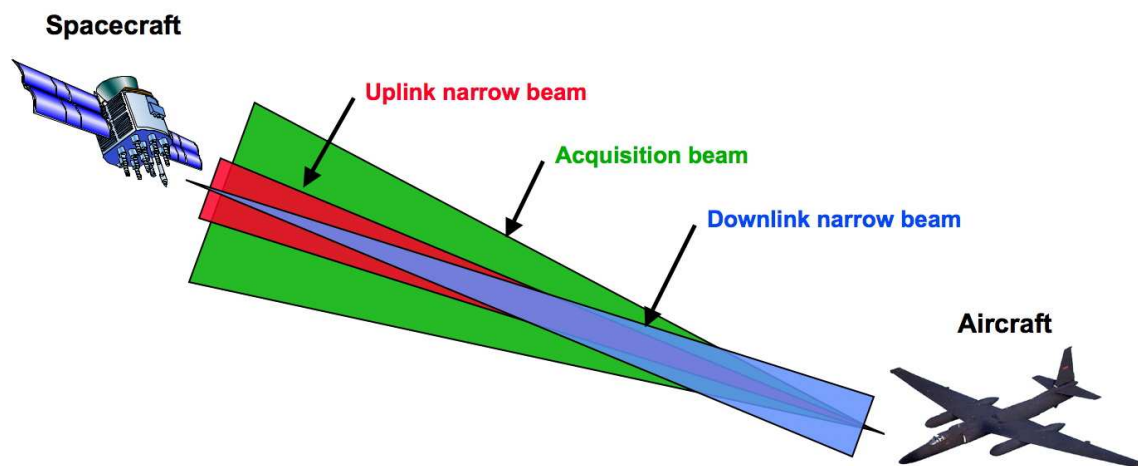
Figure 2-13: Illustration of beams used in a notional air-to-space acquisition process.

2.5.2 Pointing

Pointing is the act of using a movable mirror or other means to direct a beam in a desired direction. Common methods of directing beams are to use mechanical devices such as steering mirrors or gimbals. Gimbals are usually slow and have a very large FOR, whereas steering mirrors are typically fast and have a small FOR. A typical arrangement is to use one mirror for coarse steering and a second for fine steering. In

the future, electro-optic devices such as optical phased arrays may provide nonmechanical, electronic beam steering [11]. These devices alter their index of refraction to turn a beam, acting similarly to a blazed grating.

Determining Position

Before acquisition may begin, the acquiring terminal must know where to point its beam. To do this it must know its own position and velocity as well as the recipients'. For an aircraft, this information can be provided by global positioning system (GPS) and an inertial navigation system (INS). Satellite position and velocity can be calculated from ephemeris data. These quantities tell the aircraft terminal, with some degree of certainty, where to look in the sky for the satellite. A calculation of relative velocity between the two platforms will determine the point ahead angle the terminals must apply to accommodate for their motion. This is very important due to the narrow beamwidths and high velocities of these platforms [18].

Position Uncertainty

Due to the resolution limits of sensors and calibration of pointing mechanisms, there will remain a static uncertainty in the pointing angle. In addition, platform jitter will add a dynamic error to pointing. The combination of these factors creates a region of uncertainty. A terminal must therefore scan its beam over this uncertainty region in order to locate the other terminal. There are many methods of scanning an area, such as a raster or spiral scan of a broader beacon beam, or very fast dither or spiral scan of a narrow communications beam. A spiral scan is the most efficient way of scanning the uncertainty region. If there is large uncertainty in the recipient's position, scanning this region may take a significant amount of time and slow the acquisition process [7].

2.5.3 Tracking

Tracking is necessary to compensate for platform jitter and boundary layer disturbances. The fluctuations in OPD from an aircraft's boundary layer can cause a beam's spot to festively dance on the aperture, stressing the capabilities of the tracking system to stay in step. For small disturbances a quadrant detector (quad cell) may be adequate, but for large disturbances, wide field-of-view tracking is done with a focal plane array (FPA). The FPA is read by a digital signal processor (DSP) where the incident light is converted into an error signal of azimuths and elevations that are sent to a fast steering mirror (FSM), counteracting the disturbance. The algorithms used within the DSP are the topic of these thesis experiments.

Tracking Algorithms

Two primary types of tracking using an FPA were investigated in these experiments. The first is peak tracking (PT), which identifies the brightest pixel on the screen and directs the FSM to point at it. This is a very simple algorithm to implement and can be run at high speeds. The brightest pixel is assumed to indicate where the beam is most intense and therefore has the most power. For a non-distorted beam this would be the center of the beam spot.

The second method is centroid (or center-of-mass, COM) tracking where the COM of light intensity on the FPA is calculated and this becomes the pointing direction. This is useful for cases where there is a broad distribution of light; however, it is more computationally demanding. Also, it can be speculated that the centroid of the beam will change at slower rates than the peak pixel does, somewhat easing the requirements on the tracking mirror. The COM is not limited to discrete FPA pixel locations like the PT, possibly enhancing tracking performance.

Most other FPA tracking methods are derived from one of these two methods. A method known as windowed centroid involves creating a window around the peak pixel and calculating the COM within this window. The window can vary in size from several to dozens of pixels. At the small extreme it becomes a peak tracker and

at the large extreme it is a COM tracker. A variation of COM tracking is to only look at pixels with intensities above a threshold level. This threshold COM method mitigates the impact of noisy pixels on the FPA. Another scheme is to use the FPA as a quad cell centered on the peak pixel. This digital quad cell could simplify system design if it operated at the bandwidth of an actual quad cell.

A somewhat different concept is to define a window, say a circle with radius of several pixels, and position it on the FPA image such that it contains the most power. Its center would become the pointing direction. This is a significantly more complicated operation and leads to consideration of the limitations of FPA tracking: frame rate of the camera and processing speed within the DSP. The primary problem with more elaborate tracking methods is that they require more computation time, which reduces the bandwidth of the tracking system. Due to these restrictions and the limits of the Tracking Testbed cameras and processors, only peak and centroid tracking were experimented with in this thesis.

Summary

In summary, this chapter reviewed several important areas of a lasercom link between a space-based and airborne platform and how they relate to the experimentation. Disturbances to an air-to-space lasercom link include atmospheric fading, aircraft boundary layer turbulence, and platform jitter. Pointing, acquisition, and tracking in a lasercom link also pose a significant challenge. This background information will aid in understanding the experimental setup and results presented in the next two chapters.

Chapter 3

Hardware

Overview

The chapter will describe the many components that make up the Tracking Testbed at MIT Lincoln Laboratory. It will also detail the characterization of the deformable mirror used for emulating an aircraft boundary layer's effect on a free-space beam. Notes will also be included to highlight aspects of the tracking system that will be experimented with in the following chapter.

3.1 Lincoln Laboratory Tracking Testbed

The Tracking Testbed is an experimental laboratory in which lasercom tracking schemes can be tested experimentally in a realistic deployed environment. This environment mimics a satellite and aircraft lasercom terminal, both with transmit and receive capabilities, as well as the atmospheric channel and far-field propagation. This section will describe the major components and hardware of the Tracking Testbed.

3.1.1 Spacecraft Terminal

Within the Tracking Testbed the spacecraft terminal simulates an on-orbit lasercom terminal. It is equipped with a quadrant detector (quad cell) which acts as an ac-

quisition sensor. There is also a focal plane array (FPA) used as a tracking sensor. Closed loop tracking is carried out with a fast steering mirror (FSM). A second FSM functions as a point ahead mirror and is used in the transmit path to inject an angular offset between the transmit and receive beams, as would be used if the terminals were moving in relation to each other. Finally, a fiber launch assembly (FLA) is used to transmit signals into free-space. Figure 3-1 shows a schematic of the spacecraft terminal's tracking system. Various aperture sizes can be simulated by adjusting the transmitted and received power levels. For these experiments a 12-in (300-mm) spacecraft terminal aperture was used.
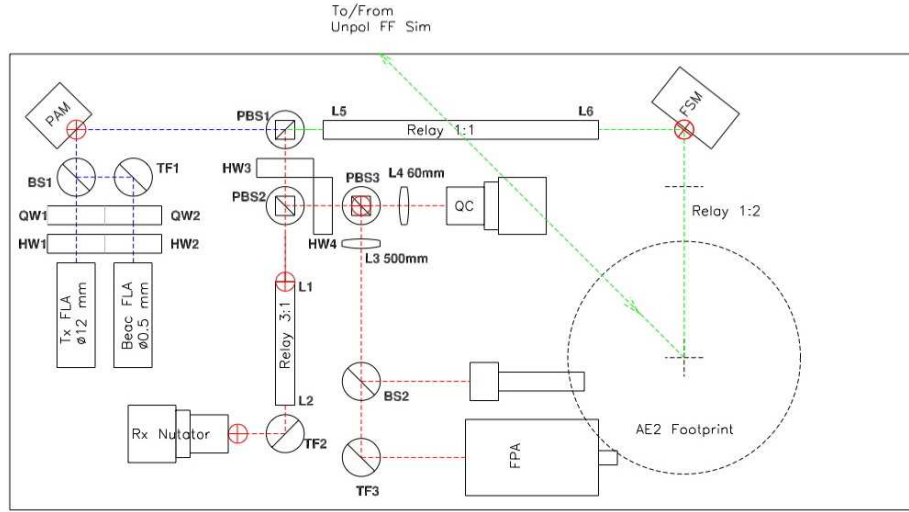
Figure 3-1: Schematic of spacecraft terminal tracking system.

3.1.2 Aircraft Terminal

The aircraft terminal simulates an airborne lasercom terminal and has a similar layout to the spacecraft terminal. It is equipped with an identical set of tracking sensors, FSM, and control electronics. Incoming light is received on the FPA for coarse tracking and the quad cell for fine tracking. It also has a common receive and transmit path. A schematic of the aircraft terminal is shown in Figure 3-2. Various aperture sizes can be simulated in the same manor as on the spacecraft terminal. For these experiments a 1.5-in (35-mm) aircraft terminal aperture was used.
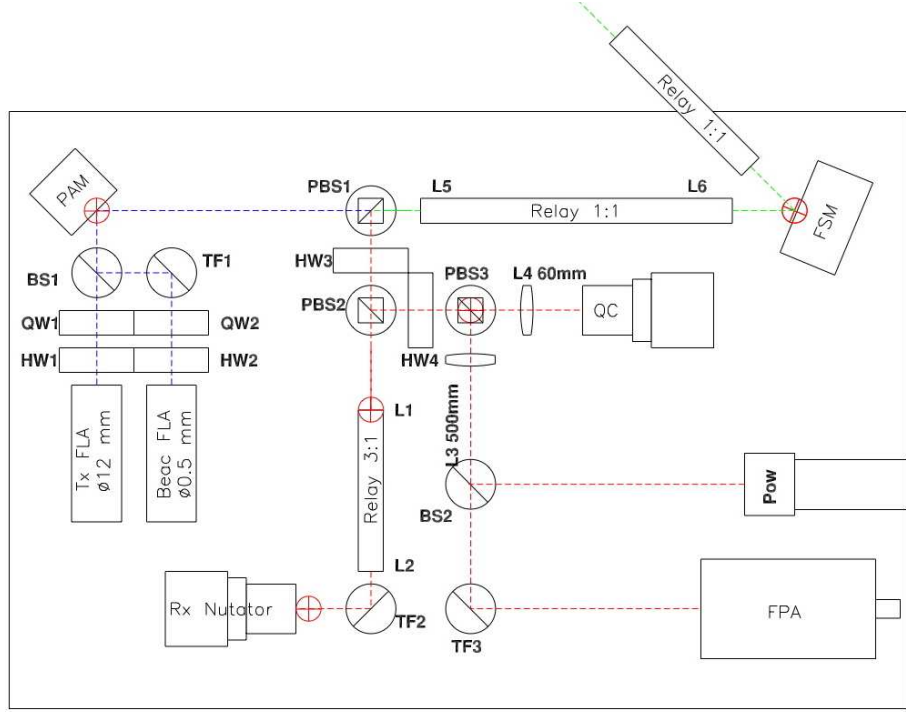
Figure 3-2: Schematic of aircraft terminal tracking system.

3.1.3 Channel Emulator

The channel emulator is used to recreate, in the laboratory, the link environment a fielded lasercom system would experience. Here the free-space beam is put into fiber to receive fading and delay. Atmospheric fading is applied to the signal using COTS Lithium Niobate electro-optic modulators. Propagation delay is accomplished through the use of a regenerative laser on the aircraft terminal's transmit path. After the delay, the beam is returned to free-space from fiber. A schematic for the channel emulator is shown in Figure 3-3.

3.1.4 Far-Field Simulators

The purpose of the far-field simulators is to add platform jitter and far-field propagation effects to the Tracking Testbed. Each simulator has a disturbance mirror which applies jitter, of a similar range of frequencies as would occur on a spacecraft or aircraft, to the signal. Also included is an overfilled fiber launch array (OFLA) which
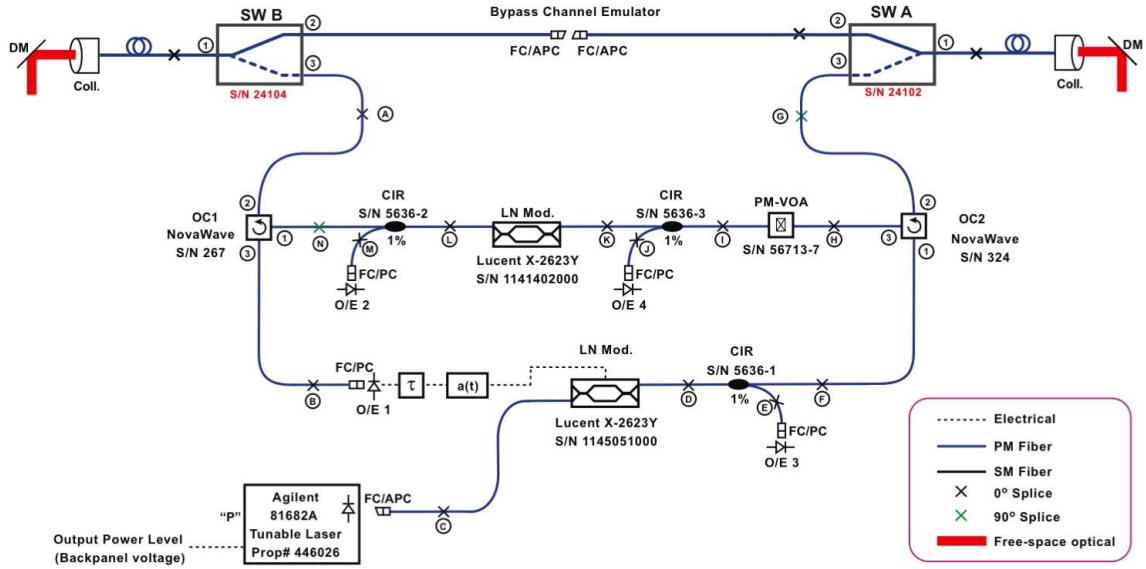
Figure 3-3: Schematic of channel emulator.

mimics far-field propagation by flattening the irradiance profile to the other terminal. This allows the terminals to be located in close proximity, rather than thousands of miles apart as with an actual A/C-GEO link.

3.1.5   Data Acquisition System

One of the most useful tools of the Tracking Testbed is its Data Acquisition System (DAS). The DAS can record high and low rate data at 4000 Hz and 0.5 Hz, respectively. Over one hundred parameters are recorded in the telemetry and saved into a single file which can be extracted later for data analysis. Some of the available parameters include power levels at both terminals, tracking sensor error signals, and terminal temperatures. Monitors show live displays of user specified telemetry to give immediate feedback of system performance. This system allows for experiments to be run in rapid succession with high precision results.

3.2 Deformable Mirror

This section describes emulating the effect of an aircraft's boundary layer (BL) turbulence in the laboratory using a micro-electro-mechanical system (MEMS) deformable mirror (DM). This is accomplished through surface deformation, which alters the path length across the beam width, resulting in an optical path difference (OPD). Using CFD time series already in terms of OPD for an aperture, the effect can be created across the DM's surface.

3.2.1 Specifications

The deformable mirror used in these experiments was manufactured by Boston Micromachines Corporation. It contains 140 actuators arranged in a 12×12 array, corners excluded. The actuators are attached to a thin membrane coated with gold foil. Each actuator is capable of 3.5-μm deflection and the actuated surface is 4.8-mm square. The actuators deflect electrostatically to applied voltages between 0 and 220 volts, causing a displacement of the reflective surface. Figure 3-4 shows an image of the DM assembly. A description of several experiments done to verify the DM's characteristics is contained in Appendix B.
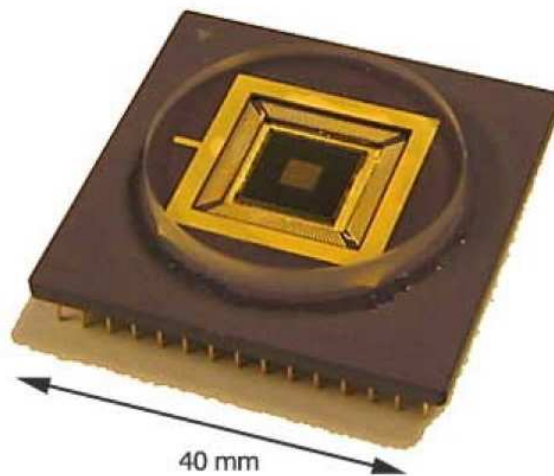
Figure 3-4: Boston Micro Machines deformable mirror used for boundary layer emulation [2].

3.2.2 Actuator Characterization

The ability to accurately recreate the OPD from the CFD data first involved characterizing the DM's actuators. To do this, a look-up table (LUT) had to be generated, organized such that displacements are correlated with applied voltage. Next, the LUT had to be used to create a voltage file that corresponds to a file of boundary layer OPD data. For each required OPD, a corresponding voltage is found from the LUT. Finally, this voltage file is streamed to the mirror at a rate of 2 kHz to recreate the dynamics of the boundary layer.

3.2.3 Look-Up Table Development

The first step, development of a LUT to linearize the DM, was by far the most time consuming aspect of this process. To get a clear picture of what the mirror's surface looks like, a Fizeau interferometer (ZYGO 1550-nm Mark IV) was used to take an image of a reflected wavefront from the DM's surface. This image is 316×232 pixels and contains the OPD data in waves for the DM's surface. This data has a significant tilt associated with it, due to the design of the glass that protects the DM, which had to be removed before further analysis could be done. Using the flat mounting surface as a reference the DM's tilt was calculated, preventing any influence that the shape of the DM's surface might have on determining tilt. This process was accomplished in MATLAB and is illustrated in Figure 3-5.

The next step was to determine what pixel in the OPD image corresponded best to each of the 140 actuators. To do this, an initial OPD measurement was taken as a reference. Next, the first actuator was deflected and another OPD measurement taken. The difference between this measurement and the reference indicated where the center of the deflected actuator was located. This process was then repeated for the 139 remaining actuators, identifying the position of each. This worked well assuming the mirror mount was not moved or adjusted for the remainder of testing, otherwise the mapping process had to be repeated to update the positions. This map condensed the interferometer OPD data from 316×232 pixels to 12×12 pixels as

46
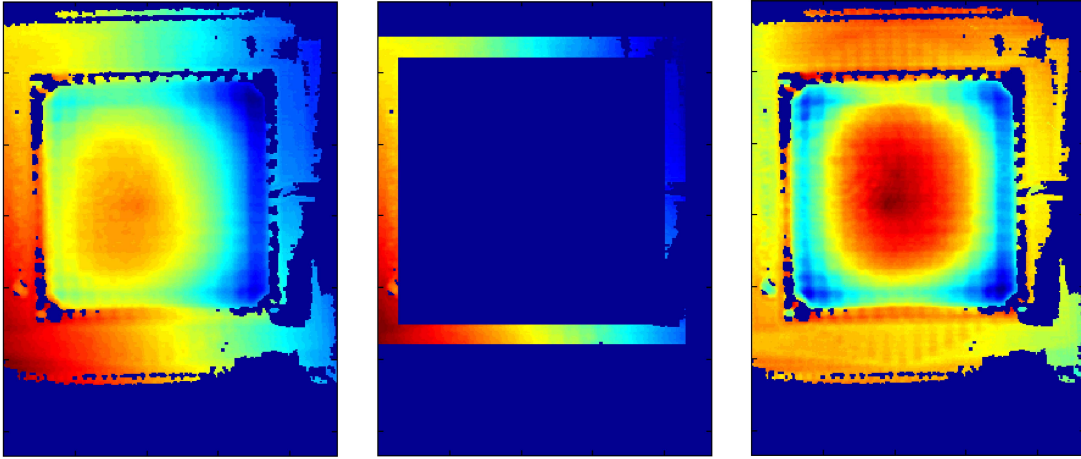
Figure 3-5: Removal of tilt from interferometer OPD image of the DM. Tilt in the image (left) is calculated by looking at the flat mounting surface only (center), and then removed from the entire image (right).

shown in Figure 3-6. Using the 12×12 pixel image, a direct correlation can be made between the voltage to an actuator and its displacement.

This relationship, between actuator displacement and voltage, was now developed. The idea was that with enough points of displacement for given voltages, a curve could be fit to that data. This curve would indicate how much voltage needed to be applied for any amount of displacement within the DM's range. The approach was to take measurements of the OPD from the DM's surface when uniform voltages were applied
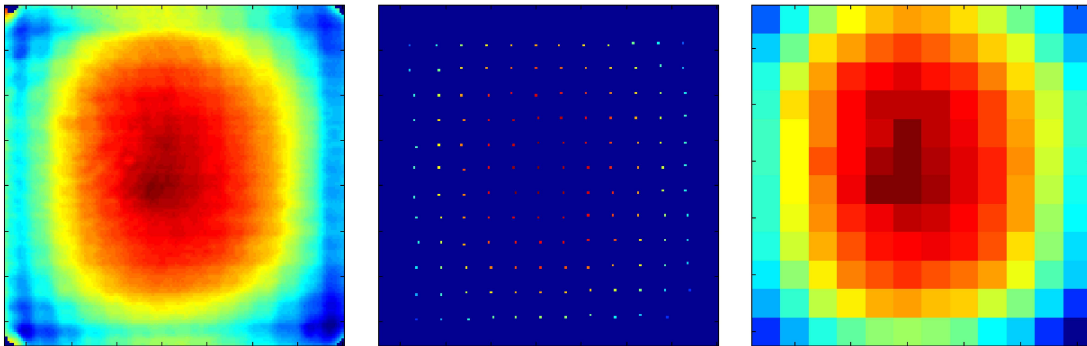
Figure 3-6: Reduction of OPD image (left) to 12 x 12 actuator image (right) by sampling at each actuator's location of maximum influence (center).

47

to all actuators, and then create plots of displacement versus voltage for each actuator. A best fit line could then be applied to the data and using interpolation, a LUT could be developed for all the actuators for any displacement. A sample curve is shown in Figure 3-7. This process can then be iterated upon, using the LUT from the previous iteration to create flat surfaces on the DM for each displacement, and repeating the curve fit. Because the surface is nearly flat, there should be minimal mechanical interaction forces from the membrane between neighboring actuators. This process will now be explained in detail.
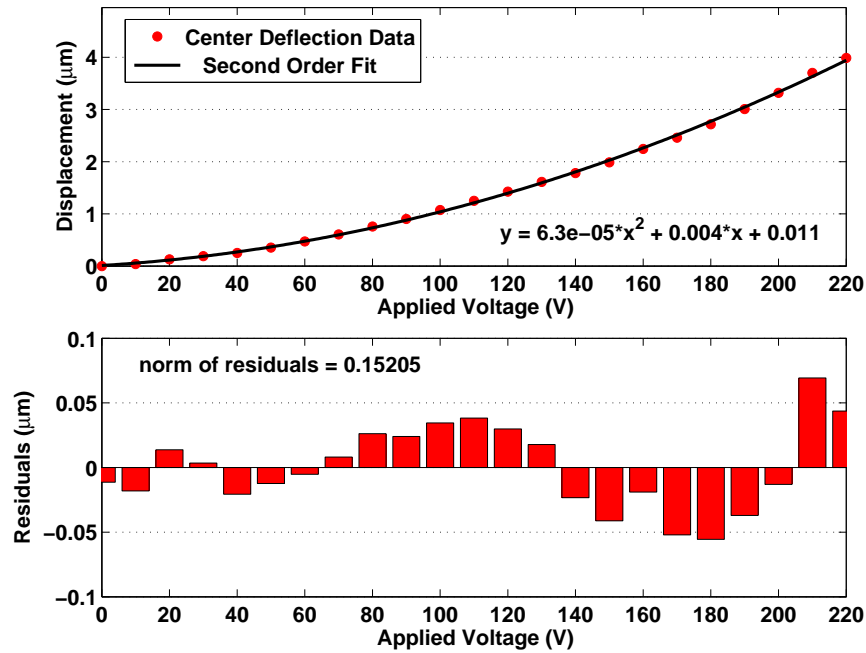
Figure 3-7: Plot of displacement and residuals vs. voltage for the DM's center with a second-order fit.

The method used to create the table was to first collect OPD data at 10 volt increments between 0–220 volts. Above 180 volts, displacements started to become so great that the interferometer could not always determine the correct OPD. Data would be missing from steep discontinuities at the edges of the DM because the light was reflected out of the interferometer's view. Once displacements became greater than a quarter wavelength, it was also possible that the interferometer would mistake the sign or magnitude of a displacement, unless there was enough data present to

48

show a smooth slope connecting the edges to the center. To counteract this effect, it helped to step down the edge actuators a bit to reduce the slope at the edges. A uniform voltage of 160 volts along the edges was sufficient to ease the slope problems when average surface voltages became greater than 160 volts. Unfortunately, on the first attempt this method of easing the edge slopes hadn't been discovered, resulting in essentially useless data for uniform displacements above 180 volts.

Using the 0–170 volt data with an additional point of 3.5 μm displacement at 220 volts, the performance specification for the DM, a best fit line was applied for each actuator. The addition of the 220 volt point was an assumption but it encouraged the fit to follow the correct shape beyond 170 volts. A fourth-order polynomial was used to provide a tight fit to the data. A purely second-order fit did not seem to capture the observed behaviors within the data, and with 19 sample points a fourth-order polynomial does not over fit. The fit was applied using MATLAB's `polyfit` function and the function `polyval` was then used to evaluate the fitted curve at displacements between 0–4 μm at 10-nm increments. The reason for evaluating the fit all the way to 4 μm was because experimentation showed that some of the DM's actuators were capable of deflecting beyond the 3.5-μm specification, as seen earlier in Figure 3-7. This yielded a table with dimensions 401×144. A displacement of 400 nm refers to row 41, and actuator 30 is listed in column 32. Even though the corners are inactive, they were included in the table as a column of zeros. The `reshape` command was used to go between a 12×12 matrix and a 1×144 vector. By using a vector representation of the surface instead of a matrix, the dimension of the linearization LUT was reduced to 2d rather than 3d. This first iteration linearization table was titled "LUT 1" and provided a starting point for subsequent iterations.

Using LUT 1, a set of measurements was taken to determine how flat a surface it generated at 250-nm increments between 0–4000 nm. The row of voltages corresponding to the specified amount of displacement was taken from LUT 1, reshaped into a 12×12 matrix, and sent to the DM. Due to the edge slope effects described earlier, when the commanded displacement became greater than 2000 nm, the edges were set to a uniform 160 volts. By doing this, it would be more difficult to implement

a curve fit to the edges, but the quality of the overall OPD data was much greater, allowing measurements to be taken all the way to the 4000-nm displacement level.

In order to define performance of the linearization table, the root mean square (RMS) error, peak-to-valley (PV) maximum, and mean height were used as judging criteria. For high quality optics, PV performance of less than a tenth of a wavelength (0.1 waves) and RMS error less than a fiftieth of a wavelength (0.02 waves) is considered acceptable. If the DM was capable of producing a flat surface that met these specifications over a wide displacement range, the linearization table was viable. A wavelength of 1550 nm was used for all calculations. The surface over which these criteria were applied was defined as a variable diameter circle, centered on the DM. In order to eliminate the additional distortions caused by the fixed edges of the DM, the diameter was taken as being 75% of the distance between actuators located on opposite edges. By Equation 3.1, the diameter is 3.3 mm. For additional comparisons, the circle diameter can be changed.

$$d = 400 \ \mu m \times 11 \times 75\% = 3.3 \ mm \tag{3.1}$$

Mean height was calculated as the average OPD over the circle. The results for LUT 1 can be seen in Figure 3-8. The PV plot hovers around 0.1 waves and the RMS error is mostly under 0.02 waves. Towards the minimum and maximum displacements, both increase above the goal, especially when above 3000 nm. The linearity of the surface displacement is also poor.

Using LUT 1, a similar process was used to create an improved LUT. With valid displacement data throughout the performance range, the `polyfit` function could now be used across the entire range instead of a limited range as before. This time an eigth-order fit was applied to each actuator's displacement curve. Proceeding to such a high order function ensured a tight fit and hopefully a better linearization. The edges were treated in a different manner than before. Their voltages only varied between 0–2000-nm displacements, so the fit was applied to this range. Beyond this range, the fit curve was continued until the slope became negative. At this point,
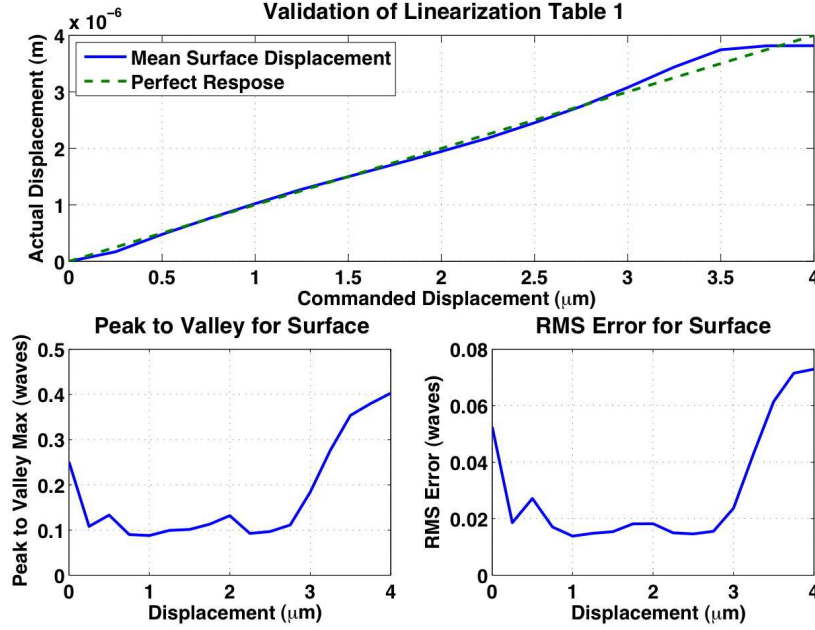
Figure 3-8: Mean surface displacement, peak-to-valley error, and RMS error for linearization LUT 1.

the remaining displacement voltages up to 4-μm displacement were equal to this maximum. This allowed for extrapolation of the data and would be accurate between 0–2000 nm. This linearization table was titled LUT 2.

The results from the validation of LUT 2 in Figure 3-9 show a much more linear nature than initially shown in LUT 1. This is attributed to the fact that the measurements were essentially flat, unlike those for LUT 1. An initial slump in the displacement is due to the need to flatten out the inherent curvature of the DM. Afterwards, the slope is steady and shows no non-linear characteristics. The PV and RMS results also show an improvement over those from LUT 1, lingering lower longer and at larger displacements than before.

Once again, an additional iteration was done. A new set of measurements was taken using LUT 2. This was done again in 250-nm increments from 0 to 4000 nm. Above displacements of 2000 nm, the edges were set to 160 volts to maintain a smooth slope. This time a new approach was taken to fit the data. Instead of using the `polyfit` function to create a best fit line for the data, the MATLAB function `interpl` was used to interpolate linearly between the data. The edges also received
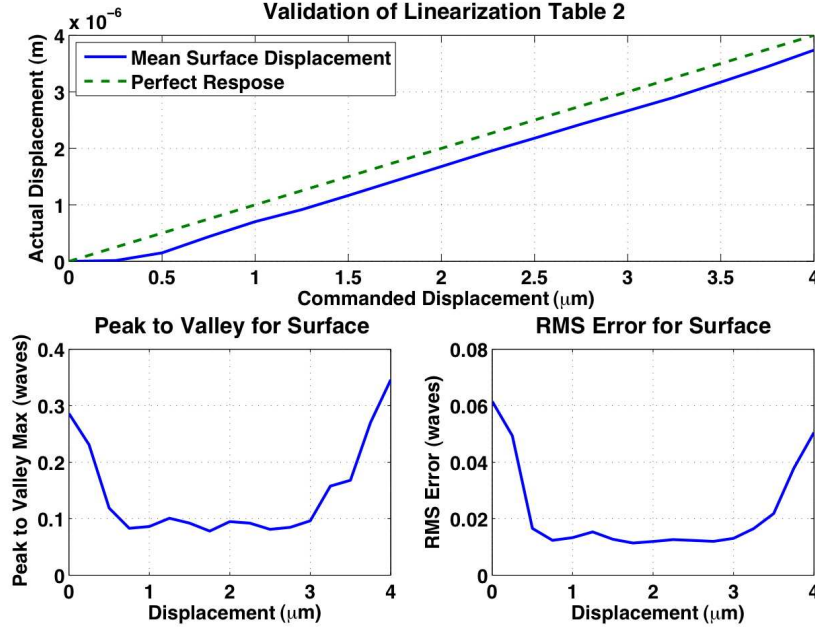
Figure 3-9: Mean surface displacement, peak-to-valley error, and RMS error for linearization LUT 2.

a different treatment than before. To extend their displacements beyond 160 volts, MATLAB's `spline` function was used. This function extends a curve based on a set of data points, allowing for extrapolation. Within the data, the `interp1` function was still used. The resulting linearization table was titled LUT 3. The results in Figure 3-10 show a very linear displacement, PV maximums less than one-tenth of a wave over a large range of displacements, as well as very low RMS error over the surface. The LUT was also given higher resolution by incrementing the displacements by 1 nm instead of 10 nm.

The interpolation and extrapolation method used to create LUT 3 were repeated one last time on the data collected implementing LUT 3, creating LUT 4. While also good, it did not improve over LUT 3. The results from this fourth table are shown in Figure 3-11.

In order to be certain of which linearization table was best the previous analysis was repeated, but now the diameter of the circular aperture was changed to 50%, 75%, 85%, and 95% of maximum. At each of these sizes the average RMS and PV max were calculated and tabulated in Table 3.1. Based on the results obtained from
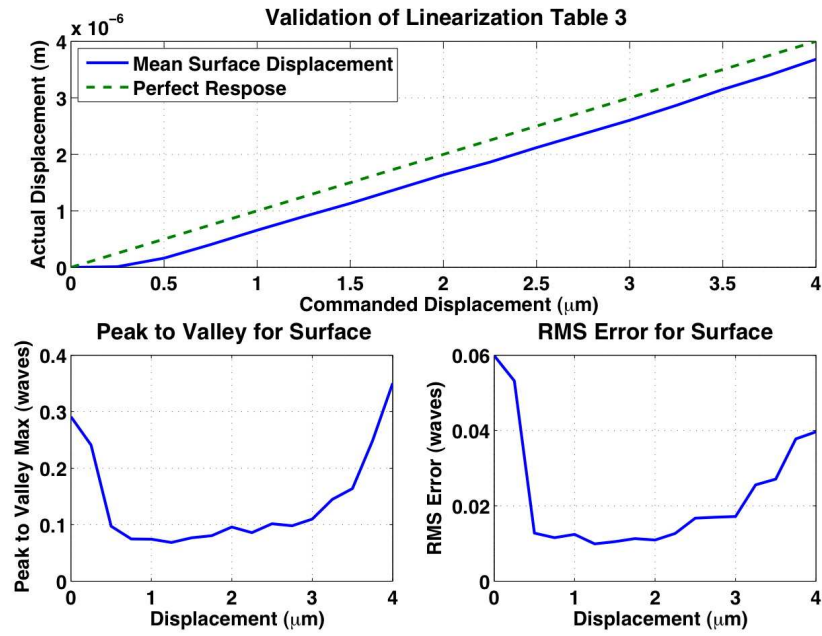
Figure 3-10: Mean surface displacement, peak-to-valley error, and RMS error for linearization LUT 3.
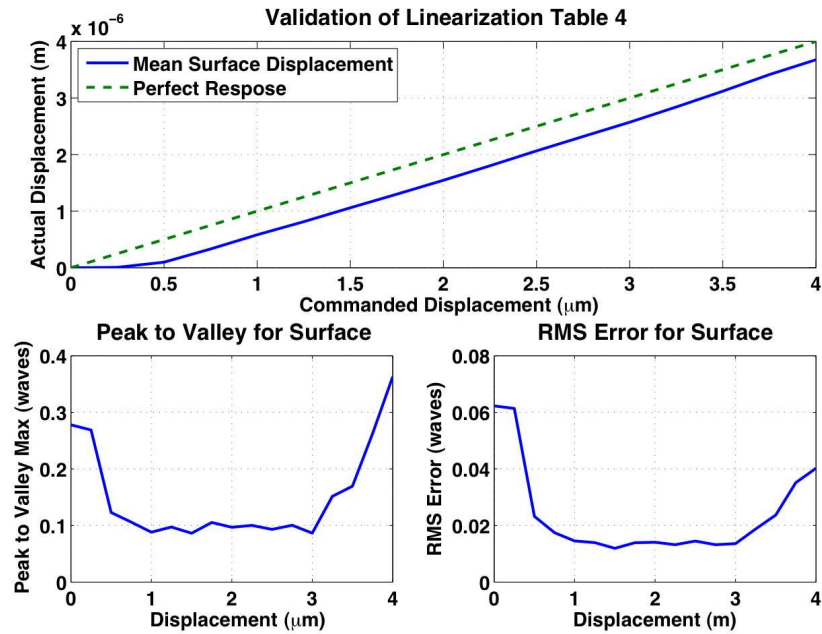
Figure 3-11: Mean surface displacement, peak-to-valley error, and RMS error for linearization LUT 4.

Table 3.1: RMS and peak-to-valley error analysis of four linearization look-up tables for several aperture sizes ($\lambda = 1550$ nm).

Aperture Diameter (% of maximum)	Mean RMS Error [λ], across 0–4000 nm			
	50%	**75%**	**85%**	**95%**
LUT 1	0.0240	0.0302	0.0447	0.0870
LUT 2	0.0161	0.0224	0.0317	0.0665
LUT 3	0.0148	0.0227	0.0312	0.0629
LUT 4	0.0165	0.0238	0.0327	0.0725
	Mean RMS Error [λ], across 500–3500 nm			
LUT 1	0.0178	0.0229	0.0343	0.0667
LUT 2	0.0110	0.0140	0.0193	0.0435
LUT 3	0.0106	0.0150	0.0199	0.0410
LUT 4	0.0118	0.0159	0.0209	0.0478
	Mean PV Max [λ], across 0–4000 nm			
LUT 1	0.1384	0.1174	0.3373	0.5485
LUT 2	0.0990	0.1451	0.2606	0.4577
LUT 3	0.0903	0.1414	0.2694	0.4556
LUT 4	0.1019	0.1515	0.2526	0.5043
	Mean PV Max [λ], across 500–3500 nm			
LUT 1	0.1104	0.1438	0.2775	0.4659
LUT 2	0.0715	0.1026	0.1830	0.3749
LUT 3	0.0699	0.0979	0.1964	0.3453
LUT 4	0.0793	0.1080	0.1721	0.3878

the four linearization tables, LUT 3 has the lowest RMS and PV error over a wide range of aperture sizes. Therefore, LUT 3 was deemed the best LUT for moving forward to recreate the BL effects.

3.2.4   Evaluation of Zernike Shapes

Now that the DM was evaluated for creating flat surfaces, its ability to create other surfaces was evaluated next. The shapes chosen to evaluate were Zernike polynomials. Zernike polynomials are an orthogonal basis set, used for describing aberrations on a circular aperture, and are often used to characterize errors in manufactured optical components. The simplest Zernike is piston, a vertical displacement of the entire surface, followed by tilt, and then other optical aberrations such as focus, astigmatism,

defocus, and coma. These aberations continue to increase in complexity as the order grows. The mathematical basis for each shape is expressed in polar coordinates. Figures 3-12 & 3-13 show the lower-order Zernike shapes that the DM attempted to reconstruct. More details about Zernike polynomials can be found in Appendix A.

To put these circular shapes onto the square DM, a square was inscribed on the circle and then divided into a 12×12 array of points. This matrix is labeled as "Commanded" in Figures 3-12 and 3-13. By reducing to a square, the coma and spherical aberrations lose some detail because changes continue to occur beyond the inscribed square. To the right of the commanded surface is the surface produced by the DM. Both images are scaled equally in waves of OPD. The outside edges of the data were removed, reducing them from 12×12 to 10×10 arrays. This prevents the edge interactions from interfering too much with the desired displacements.

Comparing these two arrays, the mean of the RMS error for each pixel was calculated for each shape and is listed in Table 3.2. The results from this testing proved that the linearization LUT was adequate for also reproducing Zernike shapes on the DM. In the lowest-order terms (astigmatism and tilt) the RMS error was very low. Based on the low resolution of the DM, only 12×12 actuators, it was unlikely that a complex circular shape would be possible to recreate. Therefore, it was expected that error would increase with complexity. This was evident in coma and spherical which had more error associated with them. This is partly attributable to actuator coupling effects; with such large displacements occurring in close proximity to other actuators, the actuators experience mechanical forces from the surface membrane. The large spherical error may also be due to poor centering of the shape's displacement, thus causing the DM to be physically unable to recreate the shape. With the exception of primary spherical aberration, the RMS error for these surfaces was less than one-twentieth of a wave.

3.2.5   OPD Playback Files

The CFD data of OPD was for a 4-in (102-mm) circular aperture inscribed within a 64×64 pixel square at a sample rate of 100 kHz with a length of only 82.02 ms.
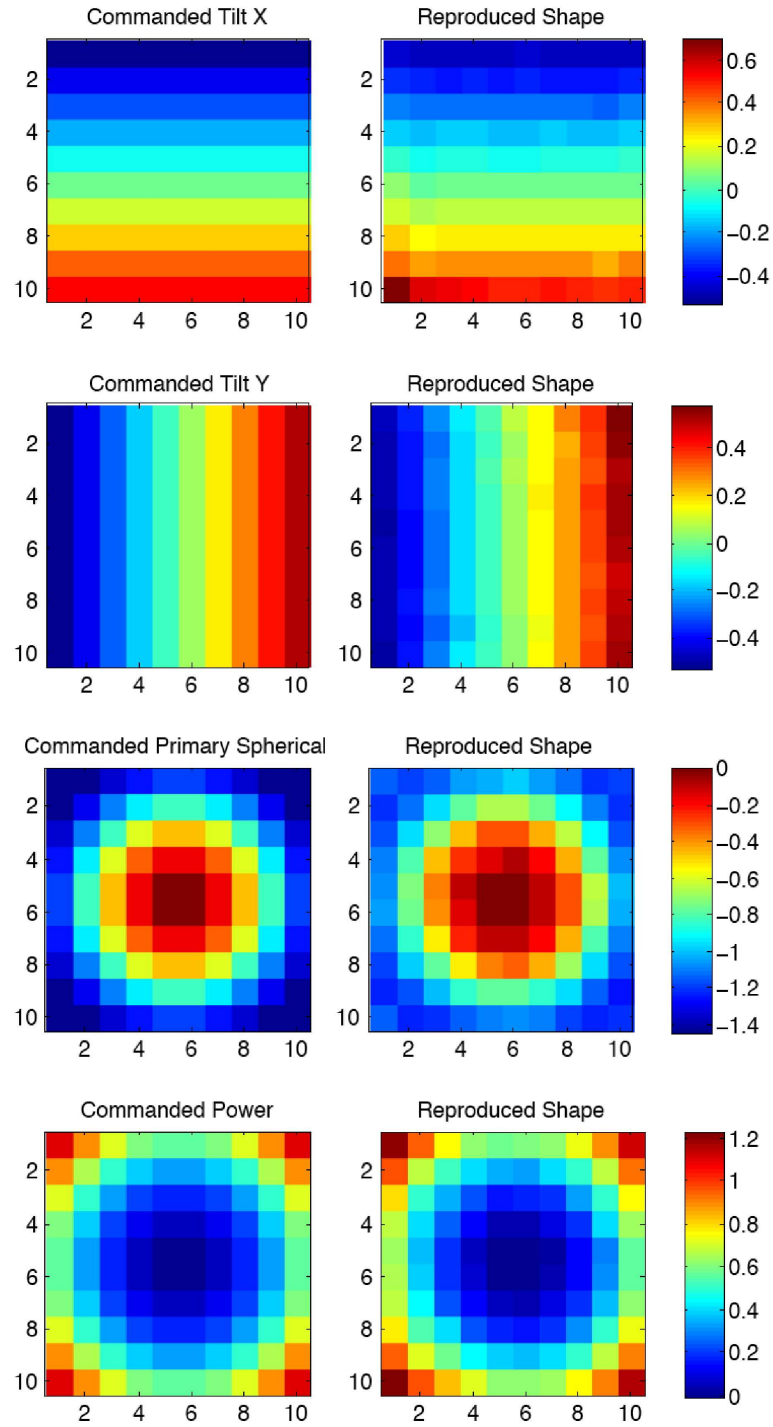
Figure 3-12: Comparison of ideal surfaces and deformable mirror replicated surfaces of lower-order Zernike shapes.
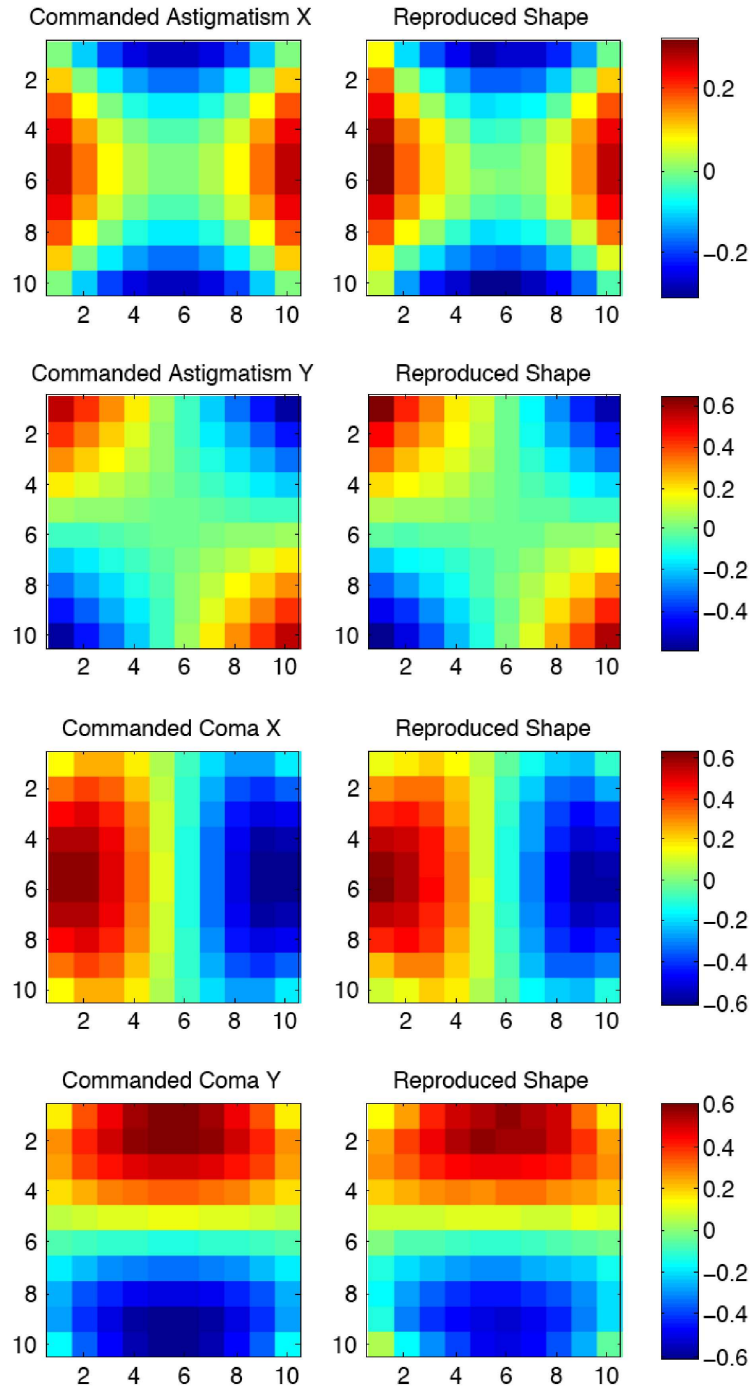
Figure 3-13: Comparison of ideal surfaces and deformable mirror replicated surfaces of higher-order Zernike shapes.

Table 3.2: RMS error between theoretical and experimental Zernike surfaces produced by deformable mirror ($\lambda = 1550$ nm)

Parameter	RMS Error [λ, waves]
Astigmatism X	0.019
Astigmatism Y	0.012
Coma X	0.021
Coma Y	0.040
Tilt X	0.023
Tilt Y	0.014
Primary Spherical	0.138
Power	0.036

This rate and size had to be modified for use by the DM. By sampling every fiftieth frame of the data, the rate was reduced to 2 kHz, the fastest the mirror is expected to be able to operate. To prove that the exclusion of higher frequencies didn't cause a loss from high frequency contributions within the boundary layer, a calculation was carried out of the disturbance frequencies present within the CFD data. By taking the Fourier Transform of the standard deviation for each frame of the OPD data, the power spectrum can be determined.

A plot of cumulative percentage of power captured versus frequency is shown in Figure 3-14. For a look angle of 0° azimuth, 10° elevation, approximately 85% of the power is contained within frequencies less than 500 Hz. This plot shows that as the look angle becomes more turbulent, a wider range of frequencies is needed to capture a high percentage of the power. For forward look angles, over 95% of the power is captured by 1 kHz. When looking out the back of the turret, higher frequencies are present within the turbulence and in the worst case only about 75% of the power is captured by 2 kHz. Therefore, DM rates of 2 kHz are adequate but not ideal for reproducing these boundary layer effects.

With a symmetric problem such as this, complimentary look angles should have identical power spectra. Figure 3-15 compares complimentary look angles and it is evident that the angles do not match identically, especially in the 135°/225° azimuth

case. This leads to the conclusion that a longer simulation time is needed for improved reproduction of more turbulent, backwards look angles.
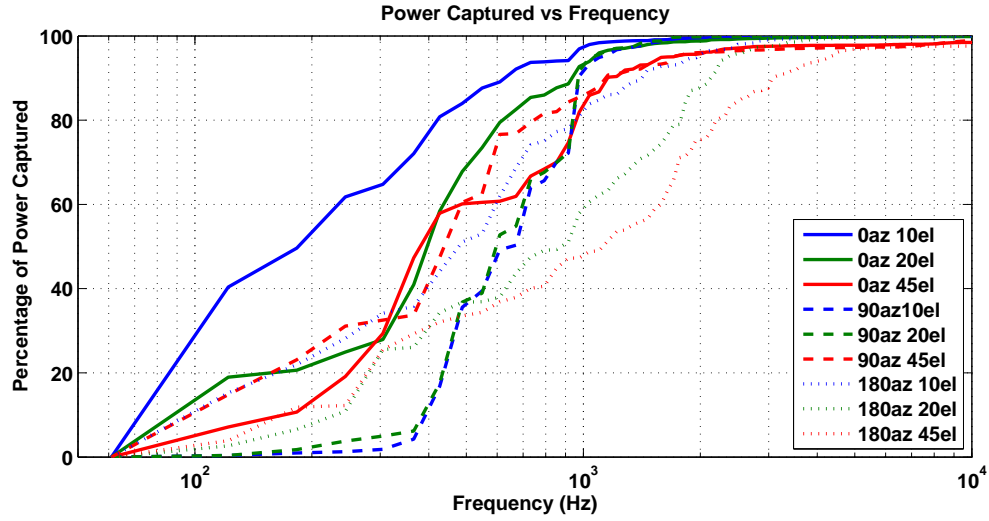
Figure 3-14: Power contained within frequencies of CFD data for various look angles, elevations grouped by color, azimuths grouped by pattern.
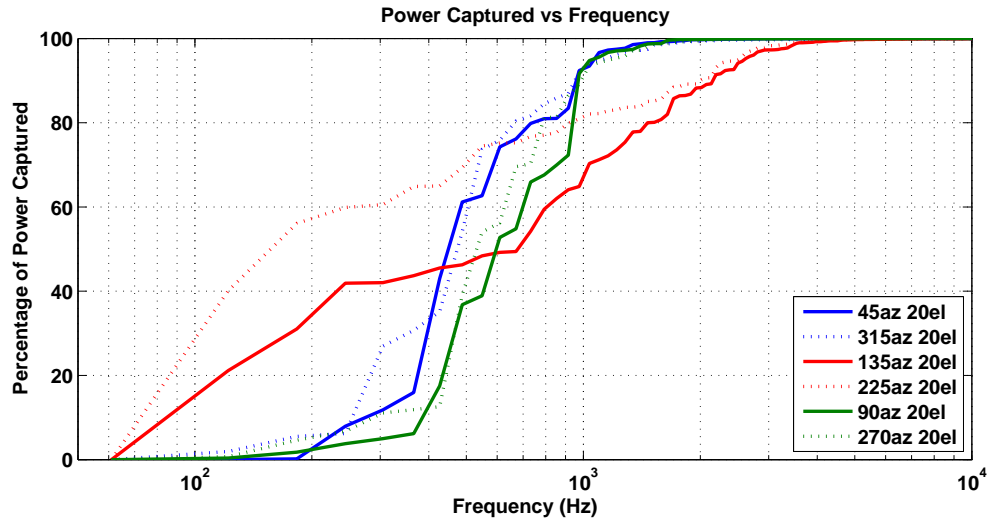
Figure 3-15: Comparison of power contained within frequencies of CFD data for complimentary look angles, paired by color.

The 2 kHz CFD data was then further reduced to a 12×12 array by sampling every fifth pixel. This process is illustrated in Figure 3-16. Due to the circular aperture, there were no data in the corners of this reduced array. The values of absent pixels were determined by averaging pixels that directly touched their sides. With all this

accomplished, the CFD OPD data were now in a form that could easily be converted to voltages and sent to the DM. A MATLAB routine was used to match the desired displacement with a voltage, for each actuator in each frame of the file. To create a smaller 1.5-in (35-mm) diameter aperture, the same process was used but over a 1.5-in square centered on the 4-in aperture CFD data. At this resolution a 2×2 pixel square equated to one actuator on the DM, so the mean value of the square was used. No special treatment was given to the corners since data existed for these areas.
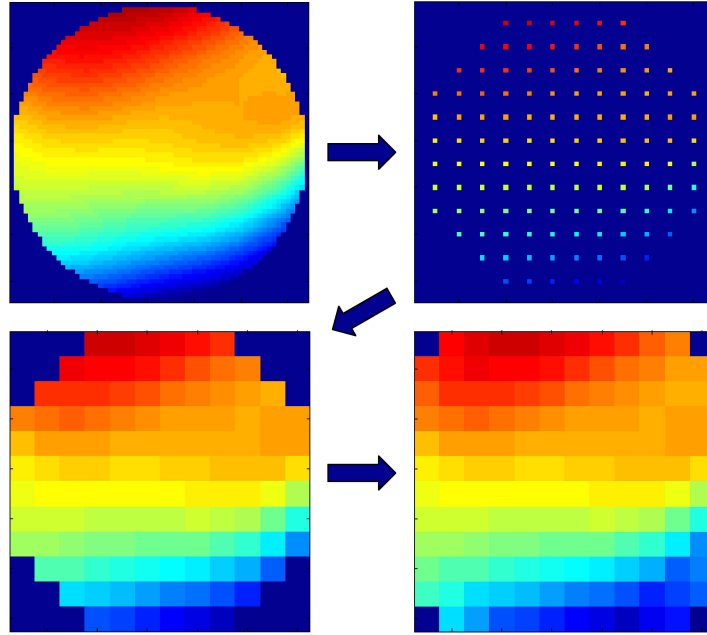
Figure 3-16: Illustration of the process for reducing the CFD OPD data to the DM.

Using LUT 3, the OPD data was transformed into an array of voltages. Sampling every 50th frame, the file length worked out to be 165 frames. This short time interval had to be lengthened in order to provide continuous simulation in the Tracking Testbed. One idea was to loop the file over and over but this would leave a discontinuity at the end of each loop. This discontinuity might be significant and would occur very frequently, possibly affecting tracking and acquisition. A second idea was to play the file back and forth which prevents any abrupt jumps in the data. Working with the resources available, the second method was the most viable way to express the CFD data during the experiments. The behavior of the boundary layer may not

be completely realistic in reverse, but this is a limitation present in the emulation. By playing the file back-and-forth, the file length is doubled to 0.164 sec, resulting in a 330×144 matrix of voltages. Bill Wilcox at LL wrote a LabVIEW Real-Time interface to stream these frames of voltages to the DM at 2 kHz.

3.2.6 Table Evaluation of CFD Data

At this point, further validation of the static performance of the DM could be performed using the CFD data. It was found earlier that the DM could accurately recreate Zernike shapes, but how it would perform in recreating the more complex patterns of boundary layer turbulence remained to be seen. To find out, the first 15 frames of CFD data for two look angles were sent to the DM, one-by-one, and measured by the interferometer. These measurements were then reduced down into a 12×12 matrix for comparison to the actual CFD data. For the calculation of RMS error between the two, each was normalized to its own mean and edges were trimmed, reducing it to a 10×10 matrix. For the look angle $90°$ azimuth, $45°$ elevation, the mean RMS error for the 15 frames was 0.0285 waves. For the look angle $180°$ azimuth, $45°$ elevation, the mean RMS error for the 15 frames was 0.0234 waves. Both of these errors are consistent with the more complicated Zernike shapes tested before.

The likely sources of error are coupling effects between actuators and the low resolution of the DM's surface. These errors are for the surface itself; when a beam is reflected off it they will double, an unfortunate but unavoidable effect. This was the motivation for driving errors as low as possible with the linearization table. One final measurement was taken of the flattest surface generated by the linearization table. From the earlier results, RMS error was at a minimum when there was a displacement of 1250 nm. At this setting, the DM has an RMS error of 0.012 waves over a 4.4-mm diameter circle and 0.009 waves over a 3.6-mm diameter circle (both centered on the DM, as measured by the interferometer). This served as a baseline measurement for comparison when the DM was integrated into the Tracking Testbed.

When integrated, the RMS error increased slightly to 0.03 waves as measured by a wavefront sensor. This is attributed to alignment of the wavefront sensor which was

highly sensitive to alignment changes, and possibly the different measurement equipment. The DM also caused a 0.73-dB loss which was compensated for by increasing the spacecraft terminal's laser power.

Dynamic performance of the DM is not easily checked. The ZYGO interferometer is made for fine static measurements that take a few seconds to acquire, making that technique unsuitable when the DM is framed at 2 kHz. A method to measure the phase front of a wave at the intended frame rate using the focal-plane image intensity pattern on a high speed camera is being developed at Lincoln Laboratory but is not yet realized. Frame shots from the tracking camera were captured to examine the intensity pattern on the focal-plane due to boundary layer effects and several are shown in Figure 3-17. These images show how a Gaussian beam can be greatly distorted due to the boundary layer. The system used for tracking this beam will now be discussed.
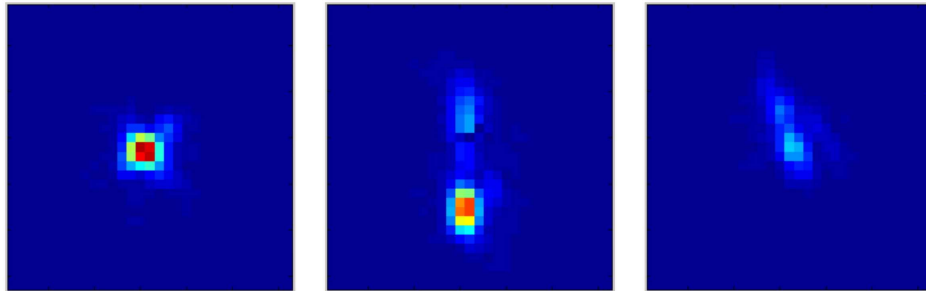
Figure 3-17: Experimental results of beam dispersion due to the boundary layer at the focal plane for look angles at 45 deg elevation, 0 deg azimuth (left), 90 deg azimuth (center), and 180 deg azimuth (right).

3.3 Pointing & Tracking System

The pointing and tracking system for a lasercom terminal involves several sensors and steering mirrors. These components complete the pointing, acquisition, and tracking (PAT) system. A block diagram showing the major components of this system is shown in Figure 3-18, several of which will now be discussed in greater detail.

3.3.1 Fast Steering Mirror

The FSM used in the tracking testbed was developed at Lincoln Laboratory and is pictured in Figure 3-19. It has a bandwidth of approximately 1 kHz and a steering range of ± 2 mrad. The mirror is driven by voice coil actuators located symmetrically about the mirror pivot. Kaman sensors are used to measure mirror motion and provide feedback. Plots of the frequency response of the FSM are shown in Figure 3-20.
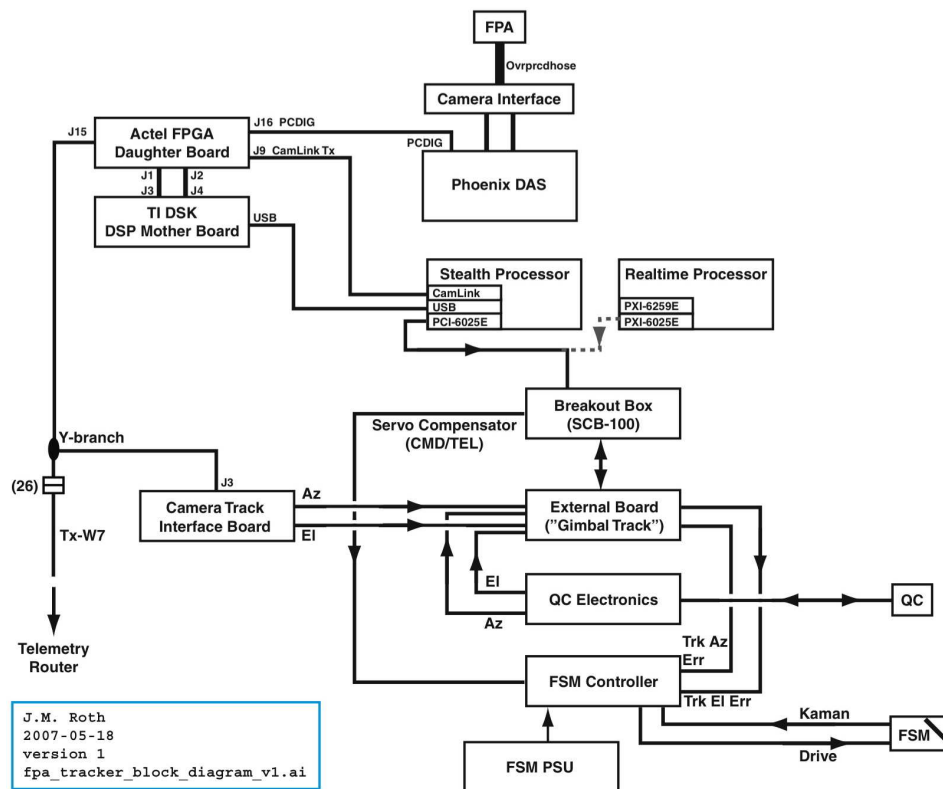
Figure 3-18: Tracking Testbed terminal tracking system block diagram.

3.3.2 Quad Cell

The quad cells used for fine tracking were also developed at Lincoln Laboratory and one is pictured in Figure 3-21a. They work by measuring the amount of light received on four quadrants. With these measurements, a DSP determines an error
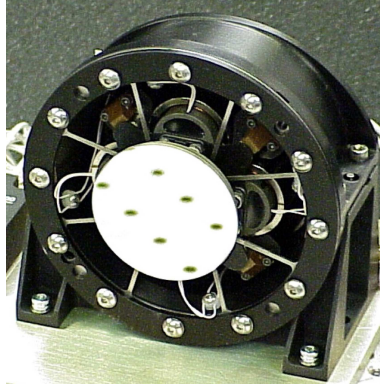
Figure 3-19: Lincoln Laboratory fast steering mirror.
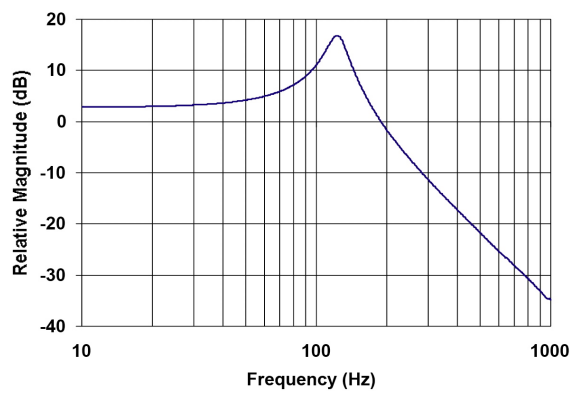
(a) Low frequencies
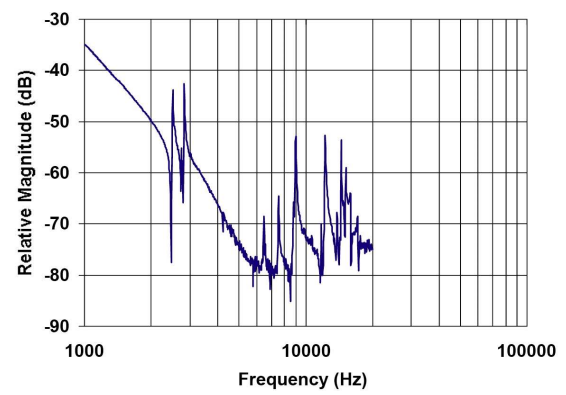
(b) High frequencies

Figure 3-20: Frequency response of MIT LL FSM.

signal consisting of an azimuth and elevation command to direct the FSM. The goal is to direct the beam such that it is received at the junction of the four quadrants. A quad cell can also provide the sum of the incident power on the four quadrants, which is analogous to a measure of the total power on aperture. This sensor is very fast over a narrow field of view (FOV) and is ideal for fine tracking; however, if disturbances become large the beam may drift off the FOV of the sensor. In this case the tracking system must revert to a sensor with a wider FOV, such as an FPA.
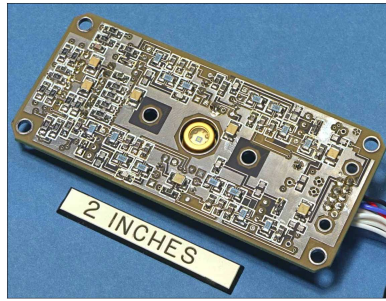
(a) LL quad cell   (b) Phoenix InGaAs camera

Figure 3-21: Tracking sensors used within the spacecraft and aircraft terminals for fine (a) and coarse (b) tracking.

3.3.3 Focal Plane Array

An FPA is contained within a camera and can serve as a wide FOV tracking sensor. The FPA used in the Tracking Testbed is a commercially available Phoenix InGaAs camera, made by Flir Systems. This camera has a 320×256 pixel FPA that operates at 345 frames per second in full window mode [19]. On the Tracking Testbed the FOV does not necessitate full window operation. By reducing the active area of the FPA to 64×128 pixels, the frame rate increases to 2367 frames per second. Taking the Nyquist sampling criteria into consideration, the FPA should at best be able to handle disturbance of up to 1183 Hz. This rate also corresponds well with the bandwidth of the FSM. A photograph of the camera is shown in Figure 3-21b.

3.3.4 Tracking States

Within the tracking system there are conditions that must be met for the terminal to move from acquisition to tracking modes. These different modes are referred to as terminal states and are real-time controlled by a finite state machine. The state machines begin in idle, waiting states and advance to tracking states. Once a terminal has reached a tracking state there is a requirement on the amount of received power at the aperture for it to remain in that state. If a power loss occurs due to scintillation or another disturbance, the terminal must decide whether to remain in the current state or regress to a lower state. The term regression is used to describe a drop in state experienced by the terminal. If impairments cause a link to fail, a terminal may regress all the way back to search modes in efforts to reacquire the other terminal.

The regression rate defines how long a terminal waits before regressing and attempting to reestablish the former state. In some cases the fading will only be temporary and the beam will reappear quickly. In other cases the beam may have been lost entirely and acquisition needs to be reinitiated. For these experiments two regression times were used: a fast regression of $\sim$1 msec and a slow regression of $\sim$3 msec. The behavior of the terminal states can vary significantly based on the regression speed and the type of disturbances applied to the beam and terminal.

Summary

The Tracking Testbed is a sophisticated tool capable of emulating realistic links between two lasercom terminals. This chapter described the major components of the Tracking Testbed, including the terminals, channel emulator, and PAT system. It also described the development of a LUT for the deformable mirror, used for emulating aircraft boundary layer turbulence. Using this testbed, it is possible to explore differences in tracking behavior and received power for different tracking algorithms and look angles.

Chapter 4

Experimentation

Overview

The goal of this research is to investigate tracking in a realistic lasercom link between an aircraft and spacecraft. Therefore, the experimentation was designed to compare centroid and peak FPA tracking while a link was undergoing platform jitter, atmospheric fading, and boundary layer disturbances. This chapter will describe the experimentation undertaken and its results.

4.1 Experimental Setup

Conducting experiments on a system with many variables is difficult because in order to investigate thoroughly the number of experiments needed skyrockets. This is very much the case with the Tracking Testbed. It is known that the behavior of boundary layer disturbances changes, depending on the look angle from the turret. This means many look angles are needed to begin to understand the BL's effect on tracking. In order to limit the number of experiments, look angles were constrained to the combinations of azimuths of 0°, 45°, 90°, 135°, and 180° and elevations of 10°, 20°, 45°, and 90°. This results in 16 unique look angles that cover half the total FOV. This half is assumed to be a mirror image of its opposite; thus, the entire FOV is covered.

As explained in Chapter 2, the intensity of atmospheric fading increases with decreasing elevation angle. Boundary layer disturbances and the time scale of atmospheric fading vary mostly with azimuth. To better understand what the chosen elevation angles mean in terms of an aircraft-satellite link, Figure 4-1 illustrates coverage area for several altitudes of one satellite and Figure 4-2 shows worldwide coverage for a five satellite geostationary constellation.
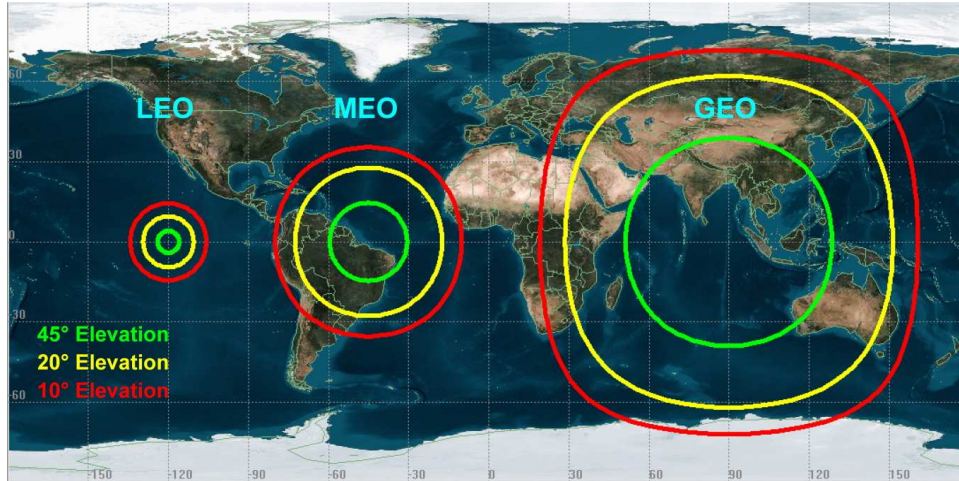
Figure 4-1: Coverage areas for three satellite altitudes and elevation angles from an airborne turret (29 kft): LEO–200 km, MEO–2,000 km, GEO–35,800 km.
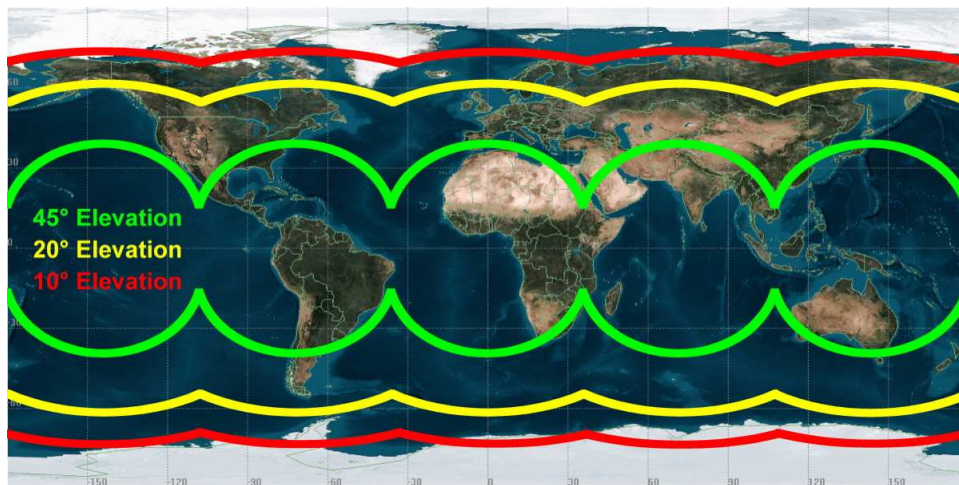
Figure 4-2: Global coverage area of a five satellite geostationary constellation for three elevation angles from an airborne turret (29 kft), corresponding to test scenarios performed.

Peak and centroid FPA tracking would be tested at each of the chosen look angles.

In addition, the tracking system's regression speed could be altered. This value controls the amount of time the tracking system waits for light to reappear during a long fade or other extreme disturbance. A slow and fast setting were available and both were tested. These experiments used symmetric tracking algorithms and regression rates at the aircraft and spacecraft terminals. This is not to say that this is the best method. It may be that pairing different algorithms and regression rates could offer additional improvements; however, to limit the number of experiments this was not investigated.

Experiments can be run with jitter, boundary layer disturbances, and atmospheric fading. The most interesting and realistic results involve all three disturbances so that is what was done. Several additional tests were added to characterize the system for these conditions with varying levels of disturbances. The end result was to conduct 66 unique tests.

4.2 Method

In order to conduct this many tests, a test plan was drafted and carefully followed to ensure accurate results. The figures of merit that would determine which setup was best were how much power was delivered to fiber, in both aircraft and spacecraft terminals, as well as power on the FPA and quad cell. This information would tell if peak versus centroid tracking or slow versus fast regression speeds were significantly different.

After conducting many of the experiments, it was discovered that over the course of a day, power levels within the Tracking Testbed could fluctuate significantly. In some cases, these fluctuations were enough to make comparisons between experiments unreliable (see Figure 4-3). The need for a reference power level for each experiment was recognized, and the test procedure was modified to include a disturbance-free period at the end of each experiment. This provided a best case power level, greatly increasing the accuracy of comparisons between experiments.

Once the experiments were completed, the data saved by the telemetry system
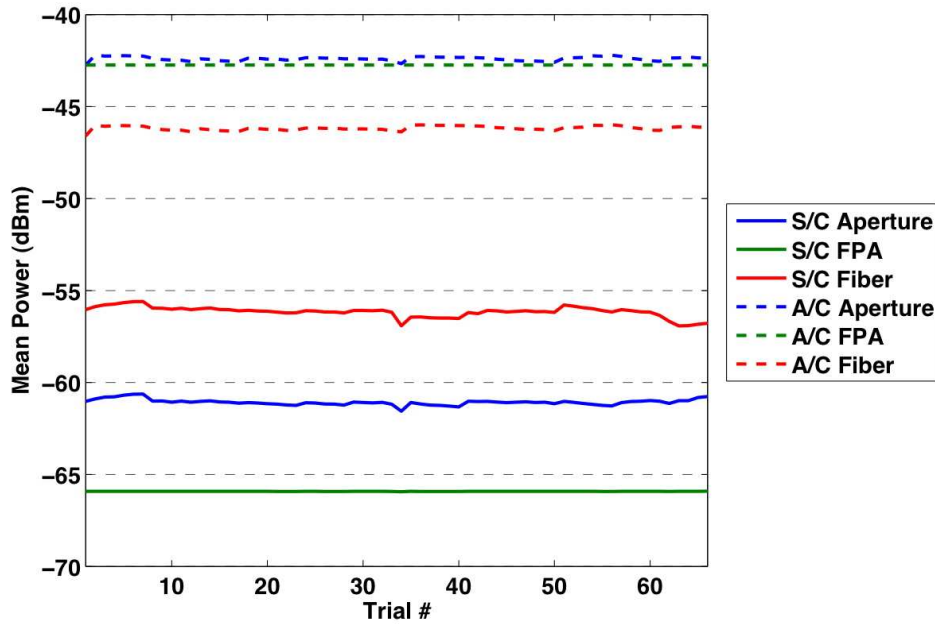
Figure 4-3: Plot of reference power levels showing fluctuations over the course of experiments.

was accessed to compute the mean and standard deviation at two points during each experiment: A period during which disturbances were enabled and the link was stable, as well as a period after which the disturbances had been disabled, providing a disturbance-free reference. With these values, differences between the tracking methods could be identified through statistical analysis.

A problem discovered after the completion of all the experiments was that the calculation of the transverse component of the aircraft's velocity, used in determining the fading time scale for each look angle, had been done incorrectly. The formula in Equation 2.1 was missing the square root. This increased the time scale of the fading, especially at low elevations and forward and backward-facing azimuths. As a result, fade durations were longer than necessary, creating a more demanding tracking environment. If these experiments are repeated in the future, better tracking performance may be observed at those look angles compared to these results.

70

4.3 Parameters of Interest

Three telemetry parameters were chosen to be monitored at each terminal: Power Density on Aperture, FPA Peak Pixel Power, and Fiber Power. Each provides a unique viewpoint of the system performance. Power Density on Aperture ($dB[\frac{W}{m^2}]$) is a measure of the radiance onto the terminal aperture and is useful for looking at the effects of atmospheric fading. FPA Peak Pixel Power ($dB[\frac{W}{m^2}]$) is the intensity of the brightest pixel on the FPA, which can be used as a measure of the spatial spread of the optical beam. This spreading reduces the sensitivity of the tracking system and is due to the boundary layer induced wavefront distortions, which lessen the peak on-axis intensity of the beam. Finally, Fiber Power (dBm) is the power that is finally steered into the optical fiber for use by the communication system. To compare tracking algorithms, all three of these parameters are useful to look at, with fiber power given the most consideration.

All of these parameters vary in magnitude during an experiment. Figure 4-4 plots these parameters versus time for a typical acquisition. At 15 sec the aircraft terminal (center plot) begins scanning for the spacecraft terminal (top plot). At 37 sec the terminals spot each other and a stable link is established. Power levels rise but still fluctuate at this point due to the disturbances in the channel. Mean power levels are recorded to evaluate tracking performance for the applied disturbances. Between 58–62 sec disturbances are removed and power levels stabilize. At this point the reference power level can be taken for each parameter. Occasional spikes in the data are the result of system noise and are avoided for mean and standard deviation calculations.

4.4 Experimental Results Format

Given the large amount of experimental data, a summary of the results requires some detailed discussion. Results are shown graphically using bullseye plots, of which an example is shown in Figure 4-5. Each region represents an azimuth and elevation pair (look angle). Azimuth increases in a clockwise direction, with 0° oriented vertically
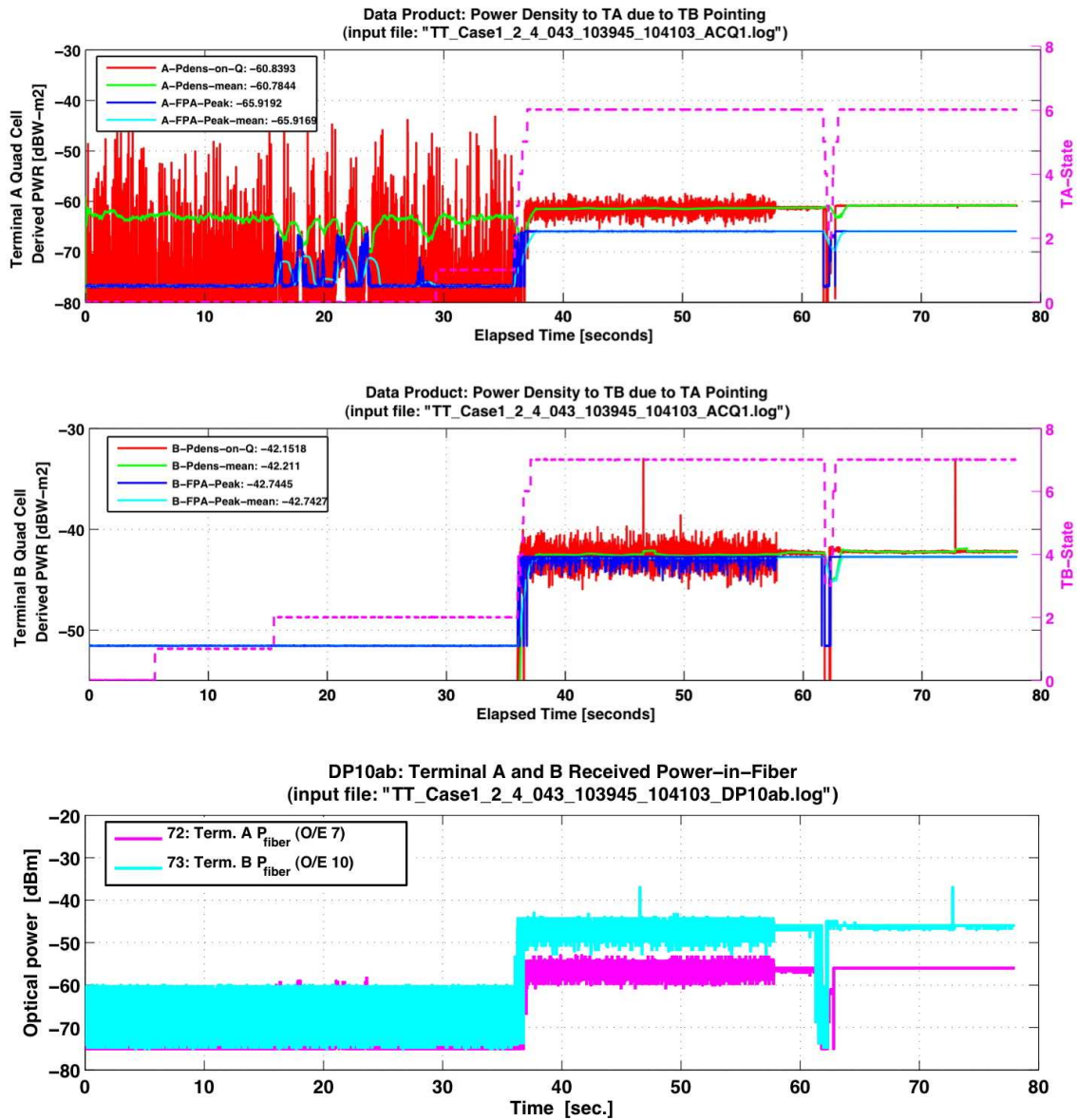
Figure 4-4: Plots from an experimental acquisition showing power levels of all parameters of interest for the spacecraft terminal (top), aircraft terminal (center), and fiber power (bottom) on both terminals.

on the page, and is measured relative to the nose of the aircraft (shown in Figure 2-4). Elevation angle increases towards the center of the plot, with 10° above the astronomical horizon for the outermost ring, increasing to 90° in the center circle for zenith. It may help to think of the plot as looking at the inside of an umbrella spread overhead. The 90°/270°, 10° (Az, El) and 180°, 10° look angles are colored gray because no stable links were achieved under these harsh conditions.
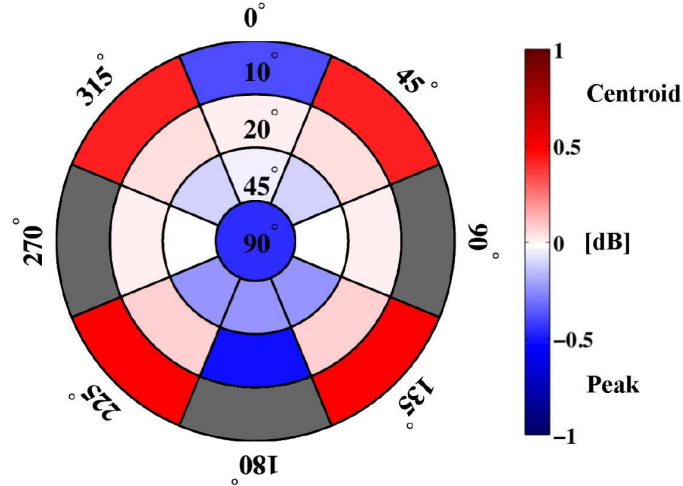
Figure 4-5: Sample Bullseye Plot with azimuth increasing clockwise and elevation increasing towards center. Scale is in dB. Grayed areas represent unstable links.

Light, moderate, and severe disturbances correspond to 45°, 20°, and 10° elevation angles, respectively. In addition to the results presented within this chapter, Appendix C contains a complete collection of tabulated data and figures displaying the results from all experiments.

4.5 Fiber Power Results

The best overall algorithms for maximizing power to the optical fiber are presented in Figures 4-6a and 4-6b for the spacecraft and aircraft terminals, respectively. These figures are based on mean power alone and do not take into account possible differences due to link behavior. What can be observed from Figure 4-6a is that centroid algorithms outperform peak in all but four cases at the spacecraft terminal. Peak performs slightly better in forward-looking, low turbulence cases at 45° elevation. Peak

73

also did well in the 180° azimuth, 20° elevation case. A preference for fast regression is shown with only five cases of slow regression being best. These cases are for a few forward-looking angles.

The aircraft terminal shows a slightly different story in Figure 4-6b. While still showing a preference for centroid tracking algorithms, slow regression is more common than for the S/C. Fast regression appears to be preferable for forward-looking cases. Peak, fast regression is now best in forward-looking cases at 45° elevation. It also works best in rear facing cases at 135°/225° azimuth, 20° elevation. To put a scale to these differences, Figures 4-7 and 4-8 display the dB difference on fiber power between peak and centroid tracking methods for slow and fast regression, respectively. Greater differences are seen on the aircraft terminal than on the spacecraft terminal, and generally speaking, the differences increase as elevation decreases. The following subsections will provide more discussion of these results.

4.5.1   Light Disturbances

Light disturbances cause few problems for the tracking system as a whole. For some forward look angles, the system was able to advance to fine tracking using the quad cell. Looking at Tables C.1 and C.2 at the dB difference between centroid and peak, these differences are mostly less than a quarter of a dB. This leads to the conclusion that peak and centroid perform nearly equivalently during light disturbances, with the aircraft terminal favoring centroid and the spacecraft terminal favoring peak. It appears that regression speed can change the performance of the tracking algorithms. The differences for light disturbances are small, and either peak or centroid tracking could be used with nearly equal performance.

4.5.2   Moderate Disturbances

With moderate disturbances applied, the differences between peak and centroid begin to be more significant, especially at 90° and 180° azimuths. For slow regression cases at the spacecraft terminal, there were very insignificant differences between the

(a) Spacecraft terminal   (b) Aircraft terminal
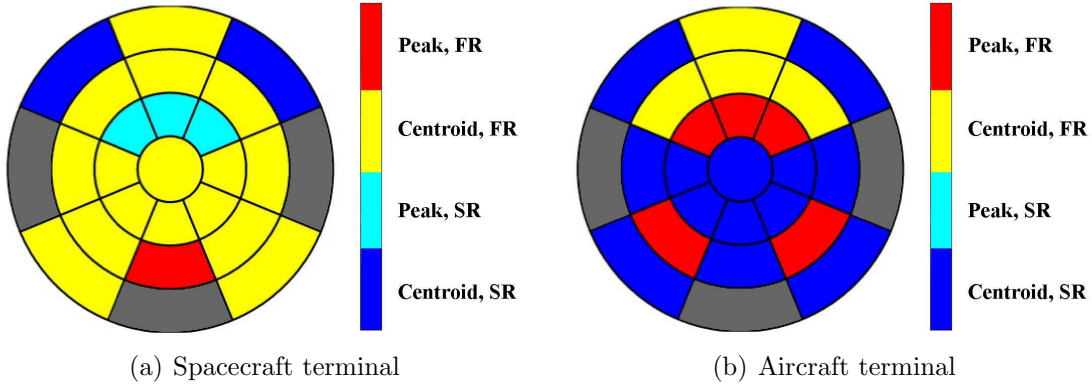
Figure 4-6: Best algorithm for maximizing power to optical fiber. Grayed areas represent unstable links. SR: Slow Regression, FR: Fast Regression

(a) Spacecraft terminal   (b) Aircraft terminal
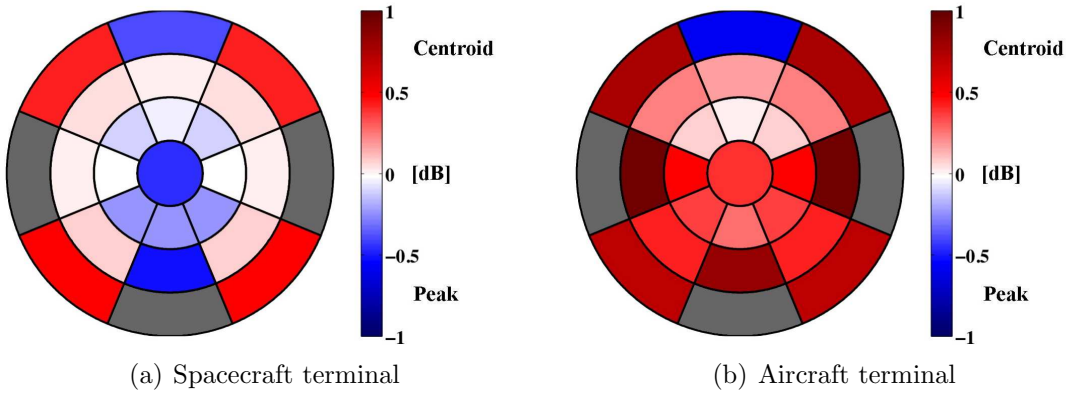
Figure 4-7: Difference (dB) in fiber power between tracking methods for slow regression, positive (red) for centroid and negative (blue) for peak.

(a) Spacecraft terminal   (b) Aircraft terminal
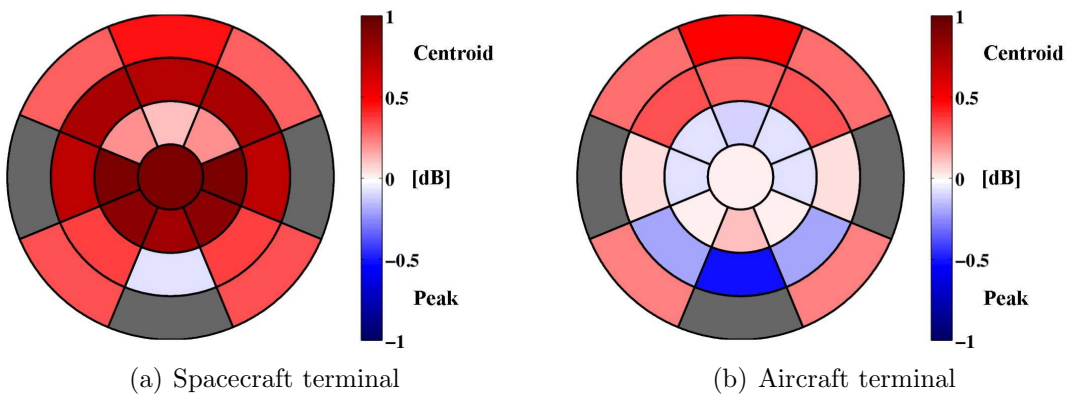
Figure 4-8: Difference (dB) in fiber power between tracking methods for fast regression, positive (red) for centroid and negative (blue) for peak.

two, except for the 180° case in which peak was best. The aircraft terminal greatly favored centroid tracking throughout, providing almost a 1-dB improvement over peak tracking at 90°. Fast regression favored centroid tracking on the spacecraft terminal. The aircraft terminal also favored centroid except for 135°/225° and 180° azimuth cases in which peak did better.

4.5.3 Severe Disturbances

Heavy fading, along with boundary layer disturbances, make this a very difficult tracking environment. A 10° elevation angle is considered to be the extreme limit for lasercom due to the degree of atmospheric fading. In fact, the 90° and 180° azimuth cases were so turbulent that a stable link was unachievable. Due to this, these azimuths will be excluded from discussion. The 0° azimuth case was somewhat marginal and represents the limit of the system, mainly due to atmospheric fading with a long time scale. For the slow regression cases, both terminals showed peak tracking performing best in the 0° azimuth case with centroid being best elsewhere. Fast regression cases showed centroid outperforming peak on both terminals.

4.6 FPA Peak Pixel Results

The best performing algorithm for each look angle, with regards to FPA peak pixel power, are shown in Figure 4-9. The experiments revealed that centroid tracking algorithms outperformed peak algorithms for the majority of look angles with a few exceptions. Figures 4-10 and 4-11 show the difference (in dB) between the two algorithms for both regression rates.

It is immediately apparent that the peak pixel power differences between the tracking methods and regression times are much less than they were for fiber power. It can also be observed from the figures that the cases in which peak tracking performed best, it was only marginally better. The next sections will describe these results in greater detail.

(a) Spacecraft terminal   (b) Aircraft terminal
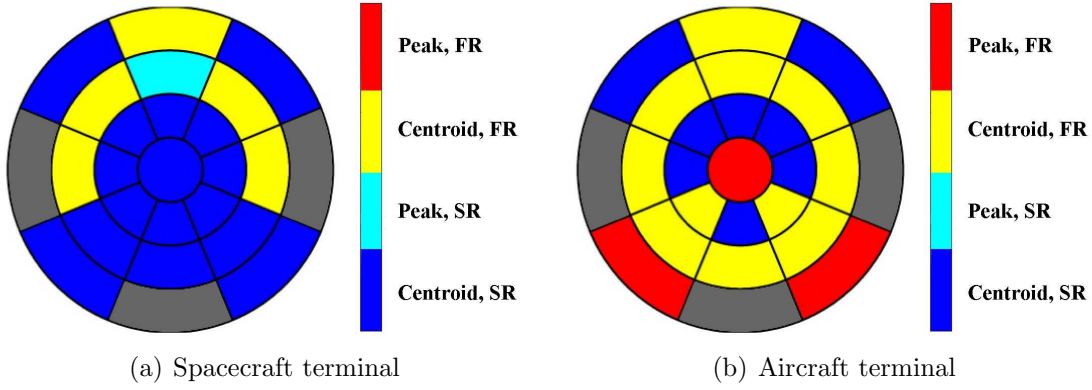
Figure 4-9: Best algorithm for maximizing mean peak pixel power on the FPA. Grayed areas represent unstable links. SR: Slow Regression, FR: Fast Regression

(a) Spacecraft terminal   (b) Aircraft terminal
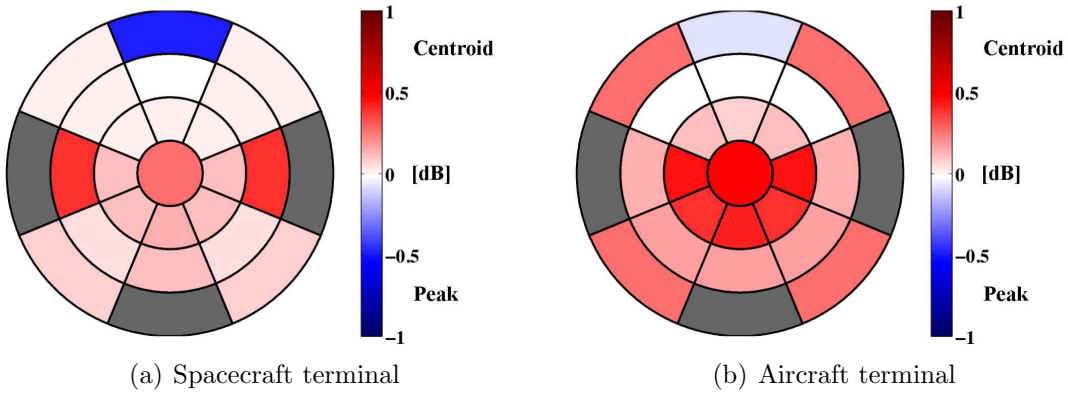
Figure 4-10: Difference (dB) in FPA peak pixel power between tracking methods for slow regression, positive (red) for centroid and negative (blue) for peak.

(a) Spacecraft terminal   (b) Aircraft terminal
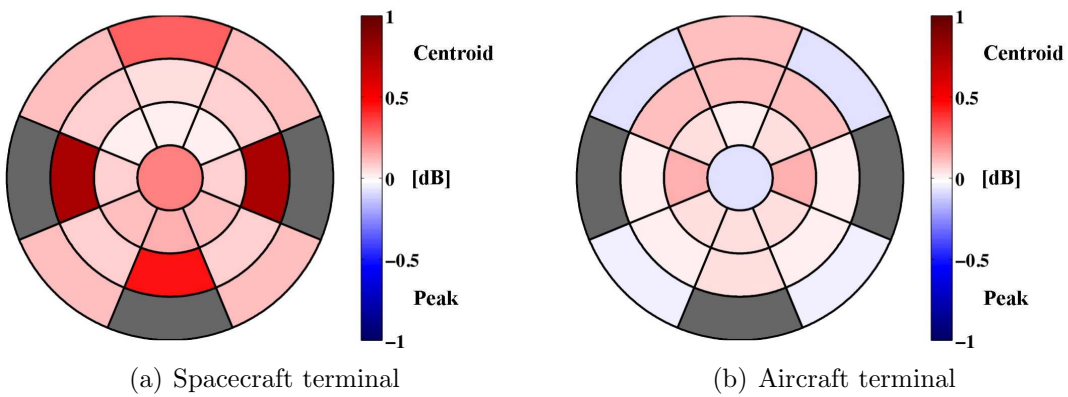
Figure 4-11: Difference (dB) in FPA peak pixel power between tracking methods for fast regression, positive (red) for centroid and negative (blue) for peak.

4.6.1 Light Disturbances

During light disturbances, for forward look angles, there is little distinction between centroid and peak tracking. Centroid algorithms dominated on the spacecraft terminal for all azimuths, showing a preference for slow regression speeds. Centroid, slow regression was best for the aircraft terminal except at 135°/225° azimuths where centroid, fast regression performed better. Peak tracking was only marginally best for overhead look angles.

4.6.2 Moderate Disturbances

Centroid tracking performed best at all azimuths except 0°, where peak was marginally better. Major differences between peak and centroid were seen on the spacecraft terminal at 90°/270° azimuths in Figures 4-10a and 4-11a. This was not observed on the aircraft terminal, where differences between peak and centroid were all relatively minor, especially for forward look angles.

4.6.3 Severe Disturbances

For the case of 10° elevation, centroid tracking is again the best performing for peak pixel power. One notable exception is in Figure 4-10a at 0° azimuth, where peak is significantly better than centroid. Due to the extreme fading at this look angle, it is possible that this test had a marginal link and the result is not accurate. Although peak tracking was best at this look angle for slow regression, centroid tracking with fast regression was still the best overall.

4.7 Power Density on Aperture Results

Looking at Figure 4-12, it can be concluded that power density on aperture is maximized with centroid algorithms, consistent with fiber power and peak pixel power. However, this parameter did have the most occurrences of peak tracking as best, primarily in the moderate disturbance band of 20° elevation. Figure 4-13 shows that the

differences between peak and centroid are quite large for slow regression, compared to fast regression differences in Figure 4-14. These results will now be explored in greater detail.

4.7.1 Light Disturbances

As has been the case previously, forward facing azimuths show little difference between peak and centroid tracking. The small scale of these disturbances are treated in a similar manner by each. Peak algorithms do show a more significant difference in performance over centroid for rear facing azimuths in Figures 4-13a and 4-14a. This is only true on the spacecraft terminal. The behavior observed on the aircraft terminal is consistent with previous results, showing a preference for centroid tracking for rear-facing azimuths.

4.7.2 Moderate Disturbances

The most notable experiment for $20°$ elevation is at $180°$ azimuth. A strong preference for peak tracking, in both the slow and fast regression cases, was observed on the spacecraft terminal. Marginal link conditions at this azimuth may have contributed to the result. The previous two parameters also show varying results for this look angle. Almost no differences were seen at other azimuths for slow regression.

4.7.3 Severe Disturbances

In severe disturbance cases centroid tracking was best, except at $0°$ azimuth for slow regression, where peak tracking was better. As mentioned with the previous two parameters, it is not known whether this is a true result or the result of a marginal link. For the remaining azimuths, Figure 4-13b shows an average gain of about 0.5 dB for using centroid tracking.

(a) Spacecraft terminal　　　　　　　　　　　　(b) Aircraft terminal
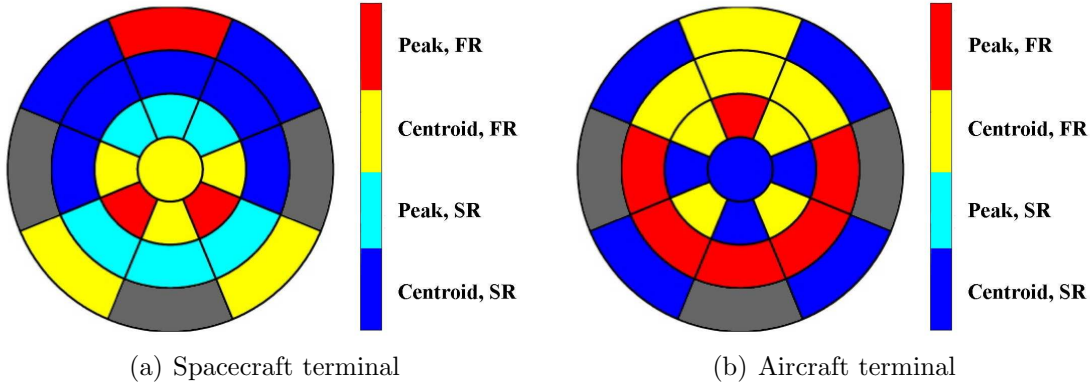
Figure 4-12: Best algorithm for providing maximum power density on aperture. Grayed areas represent unstable links. SR: Slow Regression, FR: Fast Regression

(a) Spacecraft terminal　　　　　　　　　　　　(b) Aircraft terminal
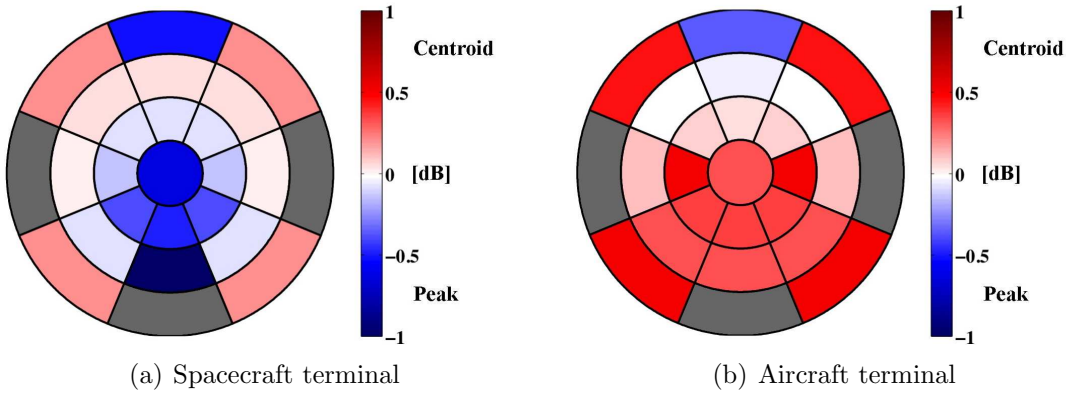
Figure 4-13: Difference (dB) in power density on aperture between tracking methods for slow regression, positive (red) for centroid and negative (blue) for peak.

(a) Spacecraft terminal　　　　　　　　　　　　(b) Aircraft terminal
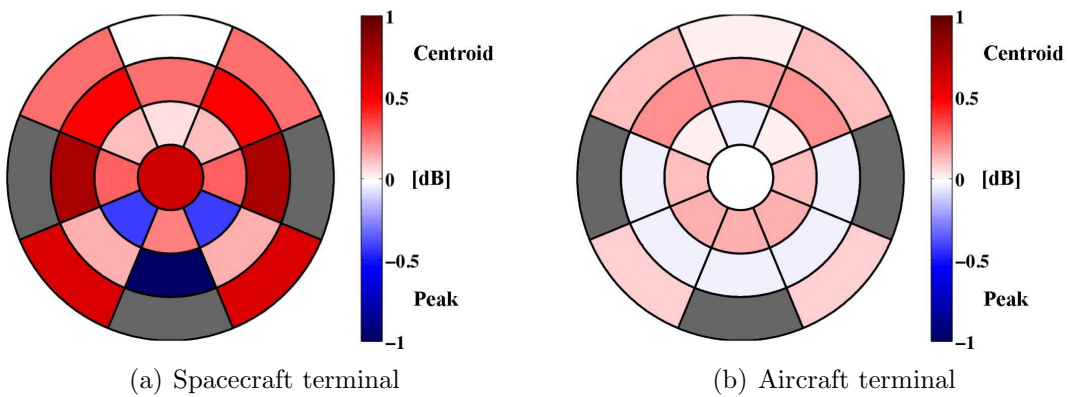
Figure 4-14: Difference (dB) in power density on aperture between tracking methods for fast regression, positive (red) for centroid and negative (blue) for peak.

4.8 Statistical Analysis

In order to make definitive statements about experimental results, a statistical analysis must be performed. For these experiments, the mean and standard deviation of the power levels were calculated from data sampled at 500 Hz for 5 sec. Using this data, centroid and peak populations could then be compared by conducting a Z test. The test statistic is calculated by Equation 4.1 with substitution of the experiment means ($\bar{x}$, $\bar{y}$), standard deviations (σ_1, σ_2), and sample sizes (m, n). To use this test, both populations must be approximately normal, independent of each other, and randomly sampled [4].

$$Z = \frac{\bar{x} - \bar{y}}{\sqrt{\frac{\sigma_1^2}{m} + \frac{\sigma_2^2}{n}}} \tag{4.1}$$

The two experiments are clearly independent because one method is not reliant on the other. Random sampling is satisfied by not handpicking the data points. The last requirement, a normally distributed population, is harder to ensure. In statistics, the central limit theorem states that any sufficiently large population will have a normal distribution. The population size of 2500 points is very large and histograms of the data are bell-shaped, indicative of a normal distribution. Assuming that the power measurements are normally distributed, all of the requirements are satisfied.

To determine whether the two methods are different, a two-tailed 99% confidence interval can be created. This corresponds to a Z value that satisfies $|Z| > 2.58$. If this value is exceeded, a claim can be made with 99% confidence that the methods are different. This threshold is made deliberately high to avoid any unintended consequences from assuming a normal distribution. Tables 4.1 and 4.2 contain the calculated Z scores between peak and centroid tracking for the two regression rates. Positive values signify that centroid tracking was better and negative values mean that peak tracking was best. Larger Z scores represent increasing confidence.

By examining Tables 4.1 and 4.2, it is seen that some Z scores are very large whereas others are quite small. Many are above the 99% threshold of ±2.58. For

aircraft terminal fiber power, Table 4.1 shows most look angles prefer centroid tracking at a statistically significant level. For the spacecraft terminal fiber power, it can be seen that peak tracking is preferred at 45° elevation, switching to centroid for stable links at 10° elevation. The other parameters can be examined similarly.

4.9 FPA Tracking Experiment

The findings from this research indicate that the differences between peak and centroid FPA tracking algorithms are often small. Although the FPA and FSM have very high bandwidths, closing the tracking loop results in about a tenfold reduction in bandwidth ($\sim$100 Hz). To see how this affects the FPA error signals, an additional experiment was conducted with only boundary layer disturbances. A look-angle of 90° azimuth, 20° elevation was chosen due to its bimodal nature, a case where peak and centroid algorithms can produce very different results. Data was collected for both tracking algorithms. The FPA error signals for each were then compared and are shown in Figure 4-15. It can be seen that the peak algorithm has discrete values whereas centroid is smooth, as expected.

Next, the signals were run through a 100-Hz filter in Simulink to see what effect a reduction in bandwidth might have. These results are labeled "Filtered" and are also shown in Figure 4-15. Distinctions between peak and centroid are much less distinguished after this filter. This may explain why peak and centroid had similar results, even at the more challenging look angles when the algorithms are most distinct.

Summary

These experiments show that in general, centroid tracking provided more power to the optical terminal than peak tracking. In mild turbulence and mild fading environments, both methods performed similarly. In more turbulent environments, the decision must be made on a case-by-case basis. Many of the differences between peak and centroid tracking are statistically significant. The improvement from picking one method over another can save up to 1 dB of optical power to fiber.

Table 4.1: Z test statistic scores between centroid (positive values) and peak (negative values) tracking using slow regression time. Significant scores are colored red for centroid and blue for peak.

Test Case	Azimuth (deg)	Elevation (deg)	Spacecraft Terminal Power			Aircraft Terminal Power		
			Aperture	FPA	Fiber	Aperture	FPA	Fiber
1.1	0	45	-2.62	3.91	-1.58	1.46	6.99	0.25
1.2	45	45	-3.16	7.91	-3.73	2.53	10.26	2.23
1.3	90	45	-1.39	3.26	-0.43	17.18	15.97	8.33
1.4	135	45	-2.91	4.41	-3.32	12.18	12.05	5.67
1.5	180	45	-7.55	5.66	-3.96	12.33	14.02	4.94
1.6	0	90	-4.32	6.12	-5.09	11.19	12.41	5.45
2.1	0	20	0.55	-0.48	0.55	-1.11	-0.76	2.64
2.2	45	20	0.86	0.86	0.73	-0.57	-0.76	4.01
2.3	90	20	0.20	7.38	0.29	2.30	2.65	10.06
2.4	135	20	-1.38	3.27	1.17	6.00	5.38	6.35
2.5	180	20	-1.44	1.35	-4.38	5.52	3.04	6.97
3.1	0	10	-2.84	-7.70	-2.93	-3.60	-1.21	-5.15
3.2	45	10	1.81	0.87	4.16	4.29	5.18	6.80
3.3	90	10	–	–	–	–	–	–
3.4	135	10	1.81	2.98	4.52	4.97	4.35	6.22
3.5	180	10	–	–	–	–	–	–

Table 4.2: Z test statistic scores between centroid (positive values) and peak (negative values) tracking using fast regression time. Significant scores are colored red for centroid and blue for peak.

Test Case	Azimuth (deg)	Elevation (deg)	Spacecraft Terminal Power			Aircraft Terminal Power		
			Aperture	FPA	Fiber	Aperture	FPA	Fiber
1.1	0	45	1.74	-1.16	3.36	-1.44	0.03	-3.68
1.2	45	45	3.35	3.71	7.11	0.44	3.64	-3.28
1.3	90	45	2.47	2.41	16.44	4.05	5.20	-1.54
1.4	135	45	-0.66	4.44	15.04	5.11	1.69	0.39
1.5	180	45	3.48	6.16	15.16	4.78	2.40	2.16
1.6	0	90	2.23	4.81	13.20	-0.37	-2.16	0.25
2.1	0	20	4.10	6.22	12.74	2.66	3.56	4.92
2.2	45	20	7.75	8.31	13.64	3.65	4.65	5.65
2.3	90	20	8.56	14.33	7.85	-1.14	0.34	0.59
2.4	135	20	1.88	4.46	5.75	-0.97	0.86	-3.28
2.5	180	20	-2.67	5.35	-0.90	-0.81	0.84	-4.19
3.1	0	10	-0.14	6.11	4.32	0.38	2.16	4.76
3.2	45	10	2.14	3.44	3.16	0.98	-1.32	2.31
3.3	90	10	–	–	–	–	–	–
3.4	135	10	4.90	3.71	3.45	0.70	-0.92	2.03
3.5	180	10	–	–	–	–	–	–
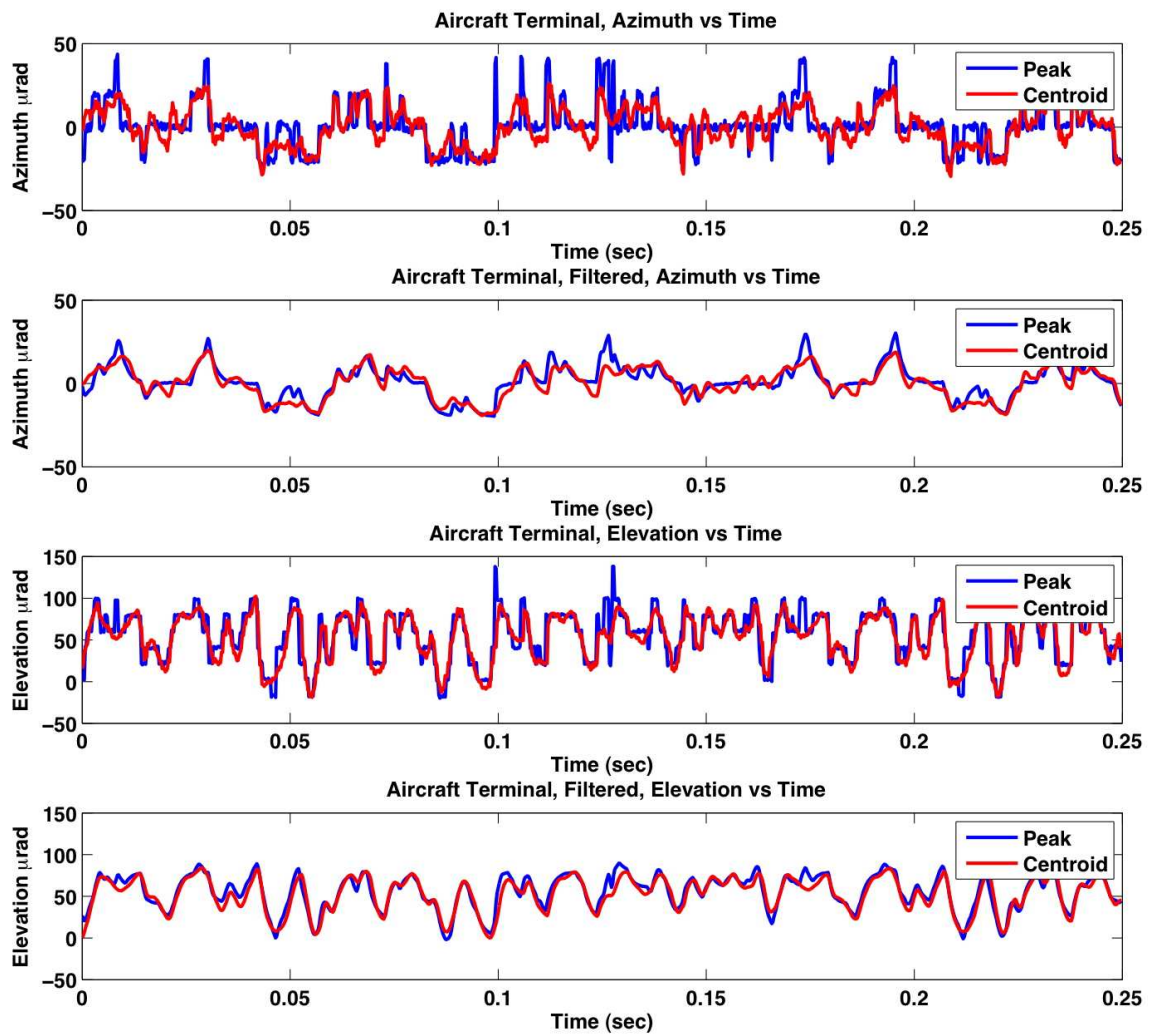
Figure 4-15: FPA azimuth and elevation error signals for peak and centroid tracking algorithms. Differences become less distinct once run through a 100-Hz filter.

Chapter 5

Conclusion

Overview

The scope of this thesis was to investigate two methods of focal plane tracking for a wide range of look angles and turbulence conditions, realistic to a lasercom link between an aircraft and spacecraft. The experiments were conducted using the MIT LL Tracking Testbed, which is capable of realistically recreating the disturbances on an optical beam propagating in the atmosphere. Also investigated was the replication of boundary layer turbulence using a MEMS deformable mirror, providing a means of emulating in the laboratory the effect of an aircraft boundary layer on a transversing optical beam. This chapter will provide a summary of the findings from this research and experimentation and offer suggestions for future research.

5.1   Review of Experimental Results

The following sections will provide a brief summary of the findings from this research.

5.1.1 Boundary Layer Emulation with MEMS Deformable Mirror

The use of a MEMS deformable mirror for emulation of an aircraft boundary layer appears to work well. First, the deformable mirror had to be characterized so as to determine the displacement of individual actuators versus applied voltage. With this data in hand, a look-up table was developed to allow the mirror's surface to be formed to a desired shape. By converting boundary layer disturbances into optical path differences for an optical beam, the DM can replicate boundary layer induced phase distortions. Analysis on several Zernike shapes found that the RMS error for the DM's surface was routinely less than 0.04 waves ($\lambda = 1550$ nm).

While the static performance of the DM is well understood, the dynamic performance remains to be investigated. Available interferometers are not able to measure the surface deformations at the 2-kHz frame rate. However, the visual appearance of a beam undergoing boundary layer disturbances created by the deformable mirror closely matches what has been done in simulation. This indicates that the dynamic performance of the DM is acceptable for boundary layer emulation.

5.1.2 Effect of Boundary Layer

Aircraft boundary layer disturbances vary significantly with look angle. A hemispherical shaped dome positioned on top of an aircraft fuselage creates no significant dynamic fluctuations when looking forward. As air accelerates around the turret, a transonic region develops at the top and sides. This disturbance tends to be very dynamic and causes an optical beam to become bimodal. Behind the turret there is wake turbulence, which causes a beam to disperse and move across the aperture.

Boundary layer turbulence may be minimized by changing the geometry and position of the optical turret on the aircraft. Several alternative turret shapes have been proposed that may reduce turbulence, improving the aero-optics. Trades have to be made between the aerodynamic and optical properties of the design to find an optimum configuration.

5.1.3 Tracking Results

The experiments on the Tracking Testbed showed that in general, centroid FPA tracking provided more power to the terminal than peak tracking. Peak tracking may be underperforming due to the limited bandwidth of the tracking system. In mild turbulence and fading environments, both methods performed similarly. In more turbulent environments, the decision must be made on a case-by-case basis. The choice of slow and fast regression speeds also had a significant effect on link stability.

Many of the differences between peak and centroid tracking are statistically significant. The improvement from picking one over the other can increase optical power to the fiber by up to 1 dB. While not a dramatic improvement, this may translate to lower bit-error rates or allow a higher data-rate to be supported.

5.2 Future Research

There are many areas of inquiry included in this thesis that are still ongoing. The ability to rapidly develop new turret shapes using CFD analysis and conduct experiments with them on the Tracking Testbed would help to optimize the shape for lasercom and aerodynamics. The use of a faster tracking camera and more responsive fast steering mirror, along with software that could switch between tracking algorithms based on the type of beam disturbance, would improve the entire tracking system. Non-mechanical beam steering systems currently under development may offer higher bandwidths than available with FSMs and should be considered for the future.

This research was done with symmetric tracking algorithms and regression rates on the aircraft and spacecraft terminals, likely not the optimum arrangement. Additional experiments with asymmetric tracking algorithms and regression rates should be conducted. Doing so may offer additional improvements in tracking performance and received power.

An increase in DSP speed would allow for more complex tracking algorithms to be experimented with, such as those with variable window sizes and threshold levels.

The peak and centroid tracking methods tested in this thesis may not be ideal in all cases. Dynamic adjustment of the window size and threshold level based on current link conditions may significantly increase tracking and communication performance. These improvements would need to be made with attention towards increased system SWaP.

More work should also be done with deformable mirrors to improve emulation of the boundary layer. A second DM could be used within an optical terminal to remove the differences in optical path distances caused by boundary layer turbulence. It would also allow for optical beams to be corrected for phase shifts experienced when transversing the aircraft terminal's window, lessening the restraints on turret shape.

Summary

Free-space laser communication is a developing technology with the potential to revolutionize the way people communicate across the globe. The maturation of this technology will easily provide a magnitude increase in data rates over those currently available. This work will hopefully aid others in further characterizing the air-to-space link and offer insight into focal plane array tracking.

Appendix A

Zernike Polynomials

Zernike polynomials are a useful way to describe aberrations that may be present in a wavefront. While they do not work well for all types of aberrations, their form is similar to the types of aberrations commonly observed in optical tests. This makes them popular in the fields of astronomy, optics, and optometry where they are used to describe surfaces over a circular domain such as tilt, coma and astigmatism [24].

The polynomials are written in two real variables, ρ and θ, and are orthogonal over the interior of a unit circle. This makes Zernike polynomials an orthogonal basis set, where each term is determined such that it contains an appropriate amount of lower order terms, making them orthogonal. Each polynomial will average to zero over the unit circle. Table A.1 lists the first eight Zernike polynomials. Figure A shows the polynomials plotted over the unit circle. The effects of piston, tilt, coma, power and astigmatism are captured within these first few terms [23].

Table A.1: Formulas for first eight Zernike polynomials.

#	N	M	Polynomial
0	0	0	1
1	1	1	$\rho cos(\theta)$
2	1	1	$\rho sin(\theta)$
3	1	0	$-1 + 2\rho^2$
4	2	2	$\rho^2 cos(2\theta)$
5	2	2	$\rho^2 sin(2\theta)$
6	2	1	$\rho(-2 + 3\rho^2)cos(\theta)$
7	2	1	$\rho(-2 + 3\rho^2)cos(\theta)$
8	2	0	$1 - 6\rho^2 + 6\rho^4$
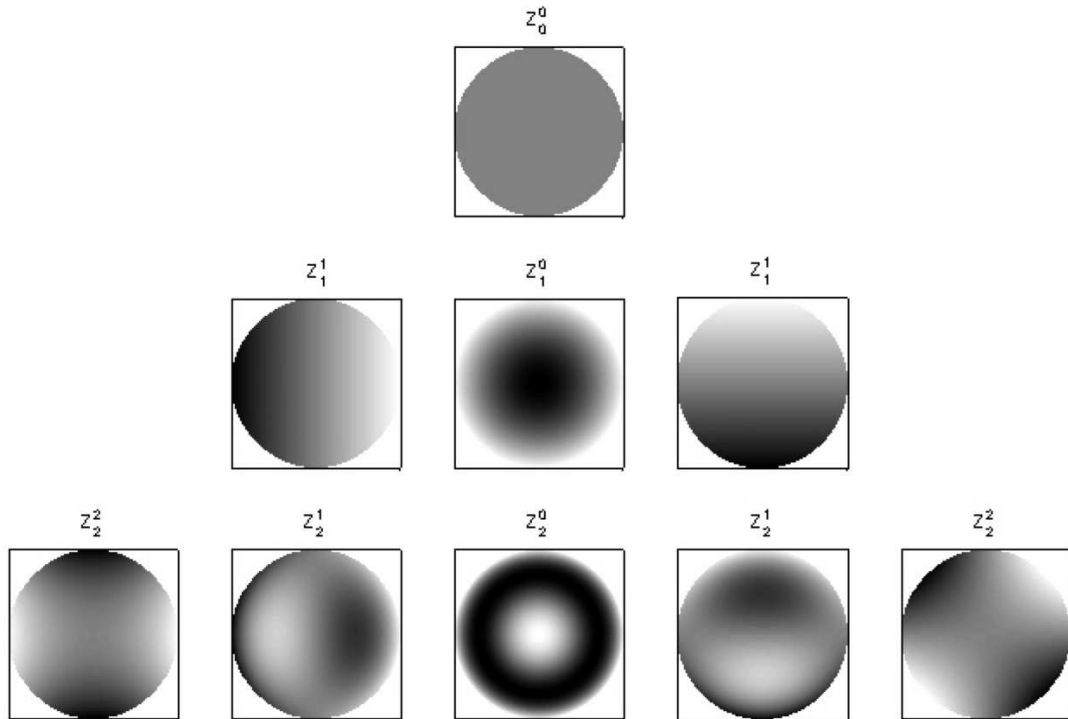
Figure A-1: First eight Zernike polynomials.

Appendix B

Deformable Mirror Specifications Verification

The deformable mirror (DM) used in the Tracking Testbed was purchased from Boston Micromachines Corp. (BMC) with a supplied list of specifications. The DM is BMC's Multi-DM with a 12×12 mirror array, 140 actuators, 12-bit resolution, 400 μm actuator pitch, 4.4 mm clear aperture, gold-coated continuous surface, and 3.5 μm maximum stroke. The purpose of this appendix is to summarize the results of tests that were done to verify key specifications supplied by BMC. These specifications are listed in Table B.1.

Table B.1: List of deformable mirror performance requirements.

Item	Value	Units	Notes
Actuator Stroke	3.5	μm	useful range
Mirror Reflectivity	> 90	%	$\lambda = 1555\ nm$
Actuator Hysteresis	< 10	nm	RMS, per actuator
Driver Bandwidth	2	kHz	
Driver Precision	12	bits	

To verify reflectivity, a tunable laser was used to reflect light off the DM and into a power meter. This measurement was then compared to that of the laser shining directly into the power meter. The experimental setup for this test is shown in Figure B-1. Polarization was controlled to ensure that it was linear and oriented horizontally.

91
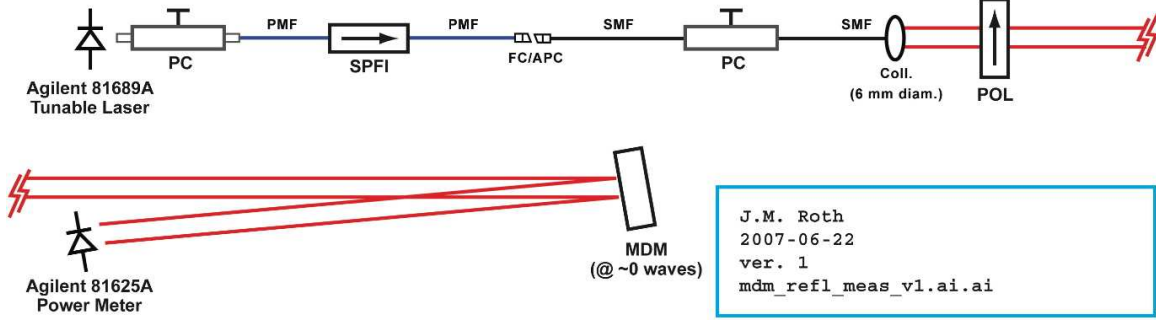
Figure B-1: Experimental setup for reflectivity testing.

The reflectivity test was done at 1540 nm, 1550 nm, and 1560 nm wavelengths. After several tests that fine-tuned the experimental setup, the power measurements showed that the mirror was over 95% reflective, meaning that the mirror exceeds the specification of 90%. A summary of the results is shown in Table B.2.

Table B.2: Results from testing of DM's reflectivity.

Wavelength (nm)	Incident Power (mw)	Reflected Power (mw)	Reflectivity
1540	0.4211	0.4039	95.92%
1550	0.4268	0.4078	95.55%
1560	0.4422	0.4209	95.18%

The stroke of each actuator is stated to be 3.5 μm. In order to verify that this is correct, the Fizeau interferometer (ZYGO 1550-nm Mark IV) displays a phase map of the waveform that can be analyzed to determine the height of any deviation on the DM. The maximum stroke of an actuator can be determined by looking at the peak-to-valley range when an actuator is at maximum deflection. The DM is rated to 220 V which is when the maximum deflection of 3.5 μm should occur.

There were difficulties in determining if each actuator was able to deflect 3.5 μm, because in order to achieve maximum deflection, the actuators surrounding it must also have significant deflection, due to coupling forces through the reflective membrane. A shape, such as a pyramid or mound, minimizes these forces and can be used to determine the maximum deflection of the center actuator. The other option is to deflect the entire surface instead of an individual actuator. Using the pyramid method to look at the center actuator, a maximum deflection of 3.8 μm at 220 V was

recorded, based off the peak-to-valley measurement. Actuators along the edges have less deflection due to the fixed edge of the membrane.

Testing for hysteresis involved monitoring the difference in a commanded shape over several sequences of commanding and neutralizing the mirror. By comparing the commanded shape to the original after several repetitions, any persistent hysteresis could be determined. The commanded shape for this test was a uniform 100-V deflection.

First, a baseline measurement was taken of a uniform 100-V charge on the mirror. Next, the mirror was cycled off and on to 100 V to approach the baseline from below. Then the mirror was set to 140 V and back to 100 V for an approach from above. This cycle was repeated five times and the average differences for the above approaches and below approaches were calculated. The difference between these averages is shown in Figure B-2. The data shows that hysteresis was minimal for almost all the actuators. A handful of actuators exceeded the 10-nm specification. These measurements were taken early on in the mirror characterization process, before the process was well refined, and actual hystersis of the DM may be less. Literature on this type of DM states that there should be essentially no hysteresis, consistent with these results [12].

Finally, precision was measured by commanding the mirror to a specific shape, taking a measurement, then varying the voltage of the center pixel by a small amount and taking another measurement. This amount was decreased until no discernable difference could be noted between it and the original shape.

This was difficult to verify. The operating range of the mirror is from 0–220 V, but deflection is not linear with voltage. Due to problems with phase data loss at large deflections, this test was conducted at 140 V, the upper limit of the voltage range where the interferometer will produce a clear image without further manipulations. Precision of 12 bits translates to 4096 distinct voltage levels over the 220-V range, yielding a distinct level about every 50 mV.

In tests, a baseline measurement at 140 V was compared to one with the center actuator at $140 + x$ V. The difference between these two measurements was taken and checked to see if movement had occurred. At this voltage level the lowest value
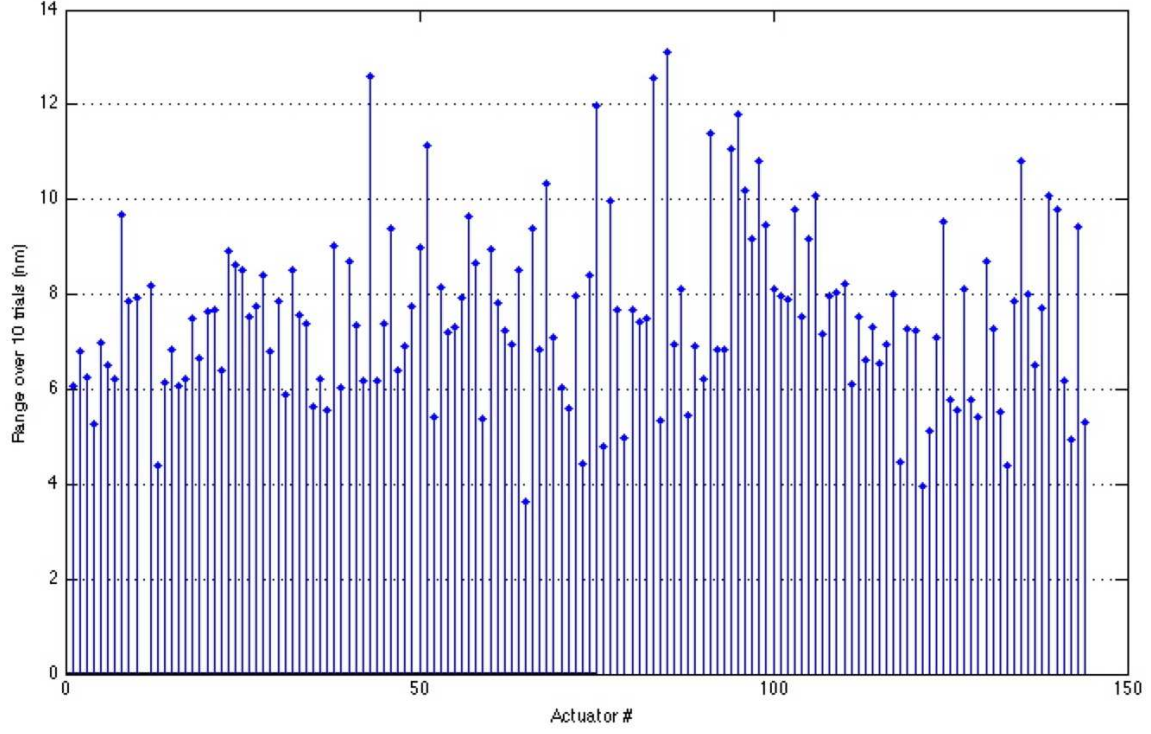
Figure B-2: Hysteresis observed for each DM actuator.

of x that still showed a change above the noise of the measurements was 500 mV. Small changes may be more evident at higher voltages where there would be greater deflections, but the experimental setup at the time would not produce clear images for that range.

This investigation found that the DM specifications tested are consistent with the reported results. The discrepancies that do exist are likely due to the limitations of the ZYGO interferometer and measurement methods. Table B.3 summarizes the findings.

Table B.3: Experimental results to verify DM specifications.

Item	Spec.	Actual	Units	Notes
Actuator Stroke	3.5	3.8	mm	useful range
Mirror Reflectivity	> 90	95.5	%	$\lambda = 1555$ nm
Actuator Hysteresis	< 10	2.3	nm	avg RMS, per actuator
Driver Bandwidth	2	2	kHz	
Driver Precision	12	12	bits	

Appendix C

Experimental Results

This appendix contains all results from experiments done on the Tracking Testbed. These results are first shown graphically using bullseye plots and are tabulated afterwards. Figure C-1 explains the setup of the bullseye plot. Azimuth increases in a clockwise direction, with 0° oriented vertically on the page, and is measured relative to the nose of the aircraft. Elevation angle increases towards the center of the plot, with 10° above the astronomical horizon for the outermost ring, increasing to 90° in the center circle for zenith.
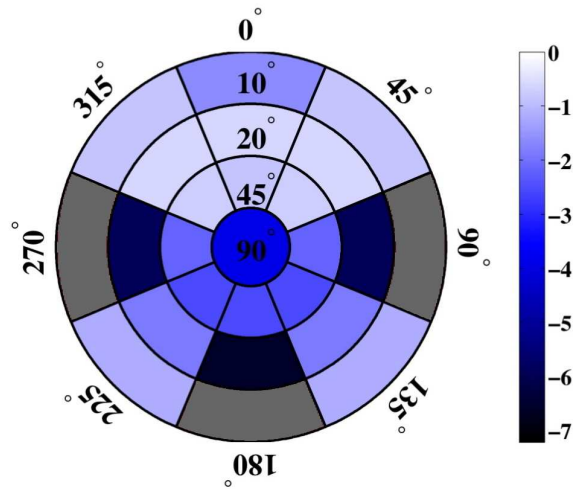
Figure C-1: Sample bullseye plot with azimuth increasing clockwise and elevation increasing towards center. Scale is in dB.

Each region of the plot represents the data from an experiment, and all share

a common scaling. The measurements of the mean are in decibels (dB) power and are relative to a disturbance free case. Therefore, a 0-dB measurement of the mean represents no loss, whereas a -5-dB measurement of the mean represents a loss of 5 dB, compared to the disturbance free reference. The measurements of standard deviation are done in a similar manner. A measurement of 0 dB means no increase in standard deviation, whereas a measurement of 10 dB means the standard deviation has increased 10 dB, relative to the disturbance free reference. Means and standard deviations are calculated from 5-sec samples taken at 500 Hz.

Experiments were done at 45° intervals of azimuth between 0–180°. As a result of the turret's symmetry, these experimental results are mirrored about the center line to complete the plot. Regions colored gray signify that disturbances were too great at that look angle to support a stable link. Subplots in Figures C-2–C-13 use the following tracking schemes: **a)** Centroid, slow regression, **b)** Peak, slow regression, **c)** Centroid, fast regression, **d)** Peak, fast regression. Tables C.1–C.4 contain mean and standard deviation data of fiber power for both the spacecraft and aircraft terminals. Tables C.5–C.8 and Tables C.9–C.8 do the same for power density on aperture and FPA peak pixel power, respectively

Also included are tables of acquisition times, terminal states, and link behavior. These additional merits help define the reliability of the link for each look angle, completing the picture for the experiments. Acquisition times are calculated by how long it takes for the terminal to enter tracking mode after having spotted the other terminal and are listed in Tables C.13 and C.14. Tables C.15 and C.16 contain state information for each experiment. Terminal states were mentioned in Chapter 4 but not defined. State 6 for the aircraft terminal and state 5 for the spacecraft terminal are focal plane array coarse-tracking modes. State 7 for the aircraft terminal and state 6 for the spacecraft terminal are quad cell fine-tracking modes. Anything less than these are different modes of the acquisition process. Finally, link behavior indicates how stable a link was for the given conditions and is listed in Tables C.17 and C.18.
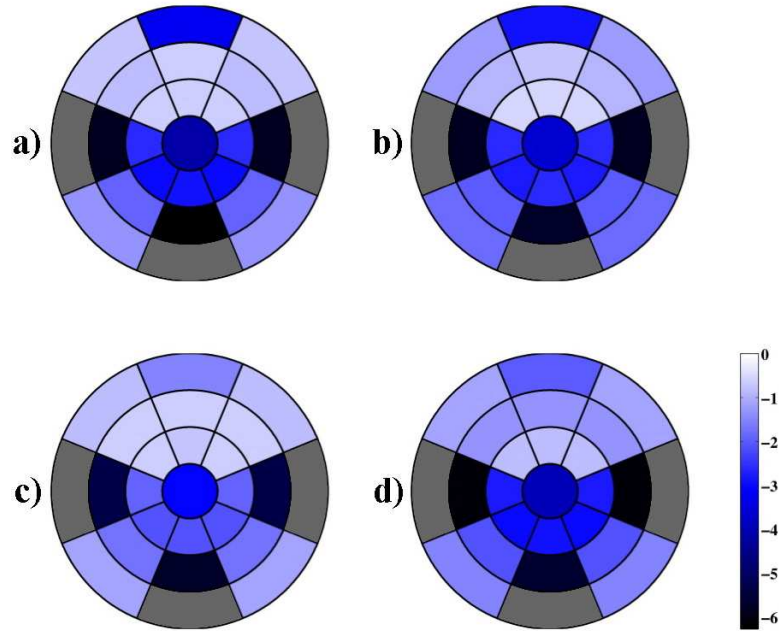
Figure C-2: Spacecraft Terminal Fiber Power, decrease in mean power due to distur-bances (dB).
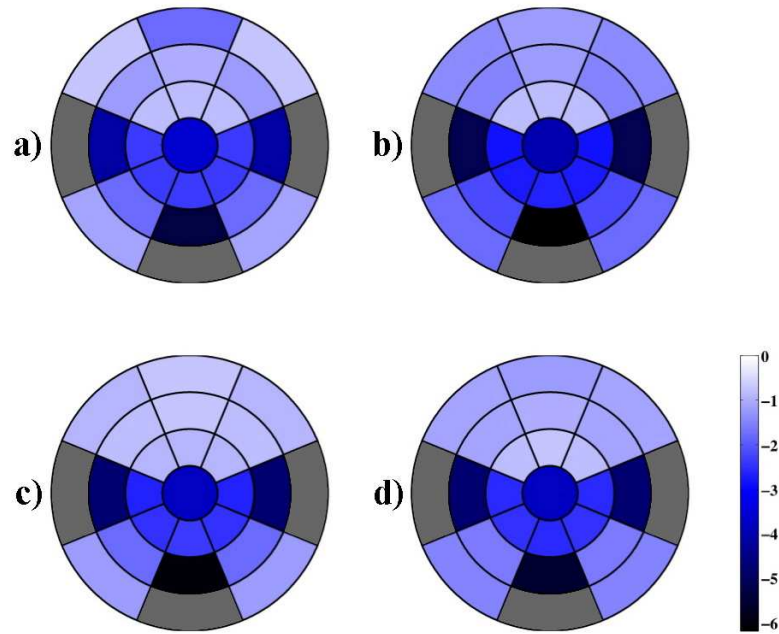
Figure C-3: Aircraft Terminal Fiber Power, decrease in mean power due to distur-bances (dB).
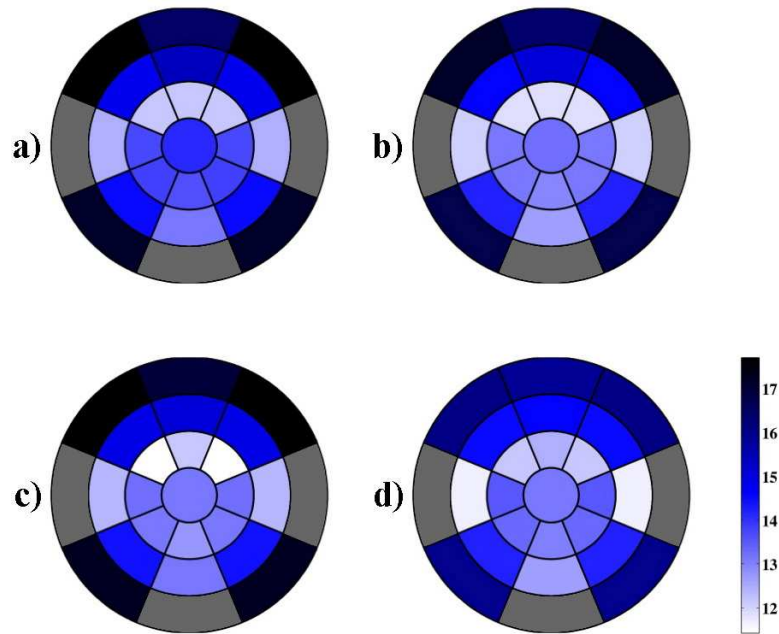
Figure C-4: Spacecraft Terminal Fiber Power, increase in standard deviation due to disturbances (dB).
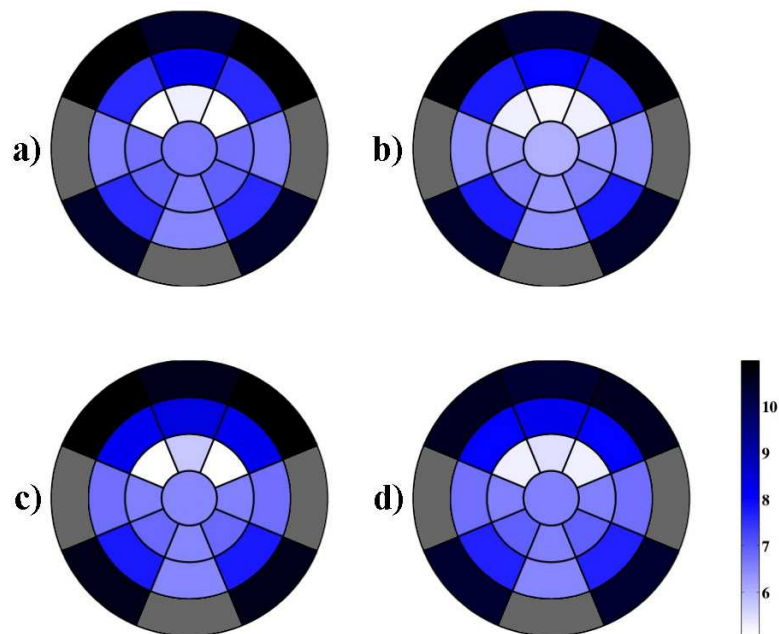
Figure C-5: Aircraft Terminal Fiber Power, increase in standard deviation due to disturbances (dB).
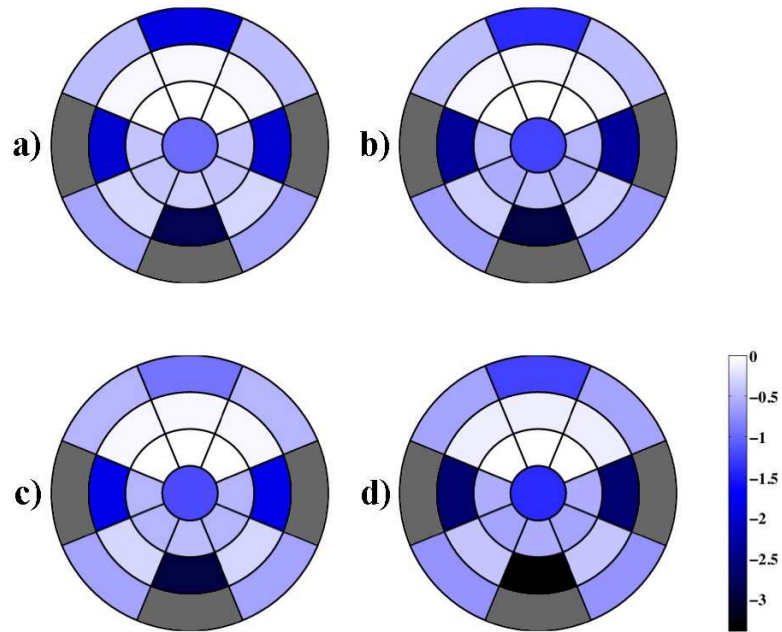
Figure C-6: Spacecraft Terminal Focal Plane Array Max Power, decrease in mean power due to disturbances (dB).
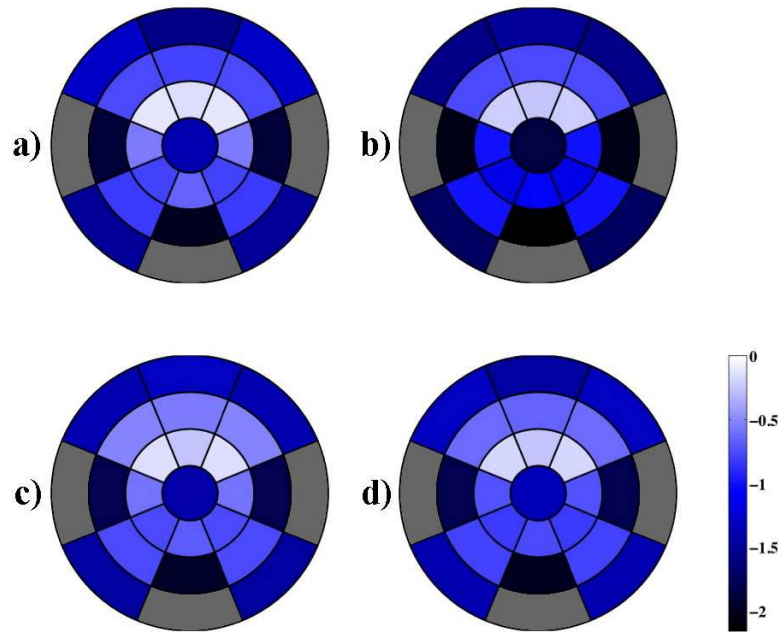
Figure C-7: Aircraft Terminal Focal Plane Array Max Power, decrease in mean power due to disturbances (dB).
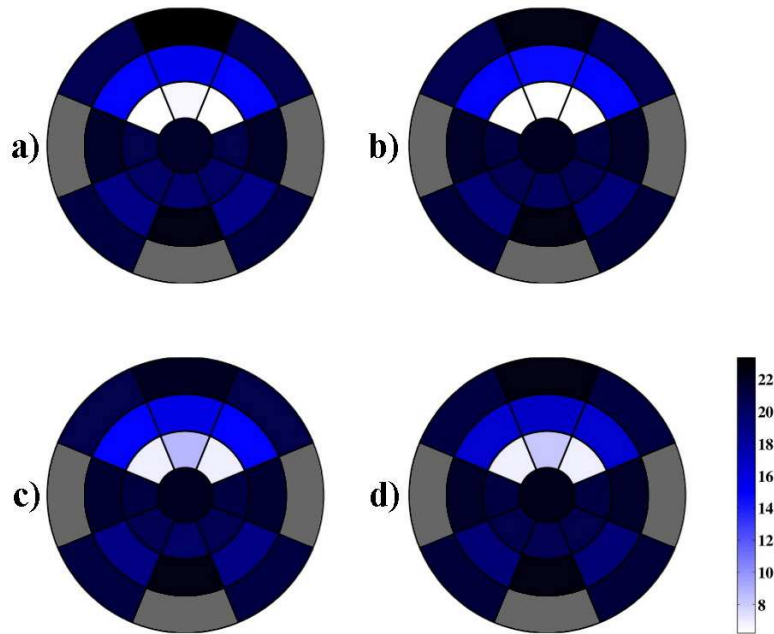
Figure C-8: Spacecraft Terminal Focal Plane Array Max Power, increase in standard deviation due to disturbances (dB).
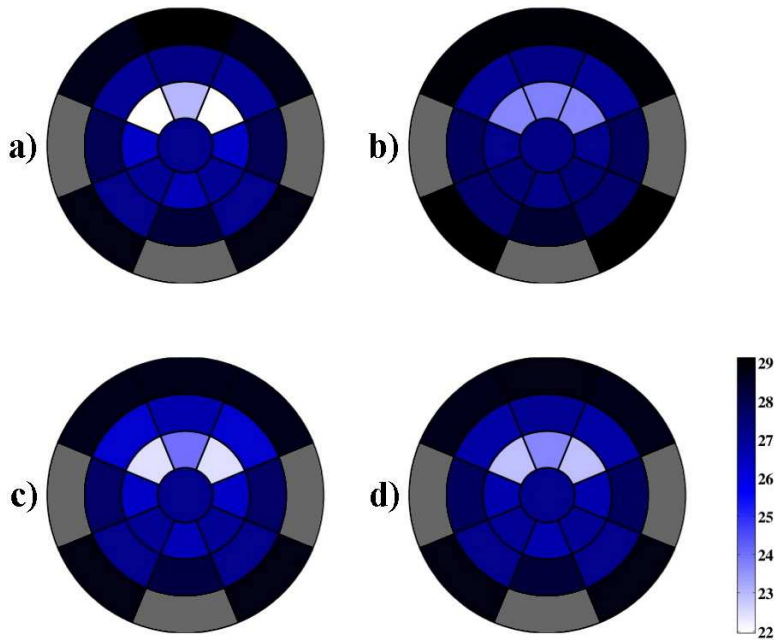
Figure C-9: Aircraft Terminal Focal Plane Array Max Power, increase in standard deviation due to disturbances (dB).
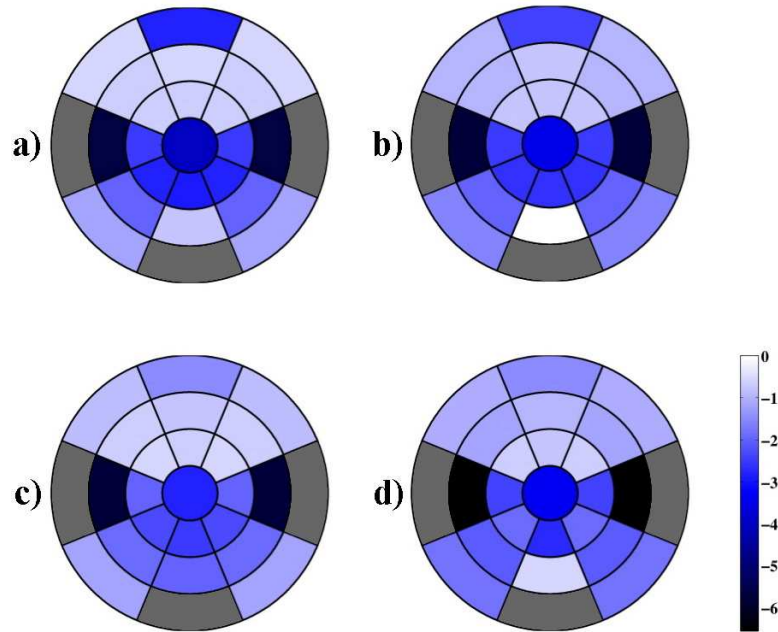
Figure C-10: Spacecraft Terminal Peak Power on Aperture, decrease in mean power due to disturbances (dB).
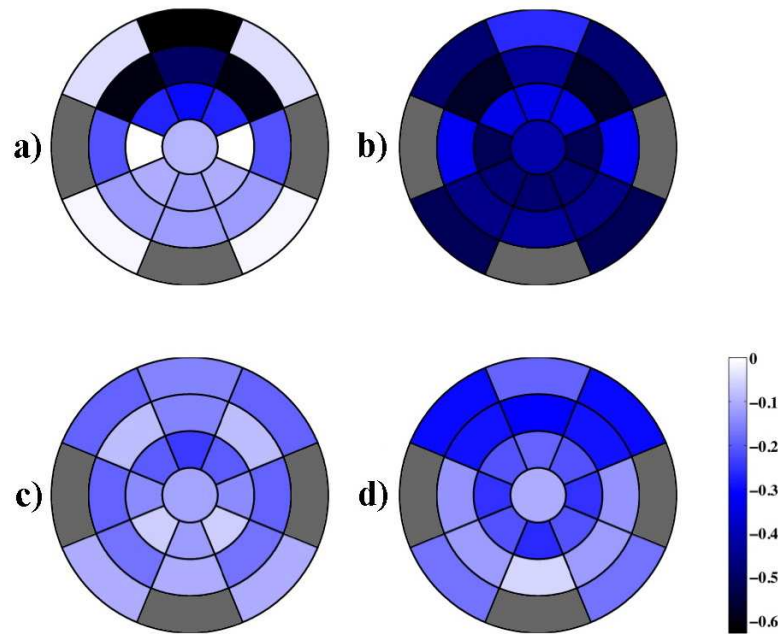
Figure C-11: Aircraft Terminal Peak Power on Aperture, decrease in mean power due to disturbances (dB).

101
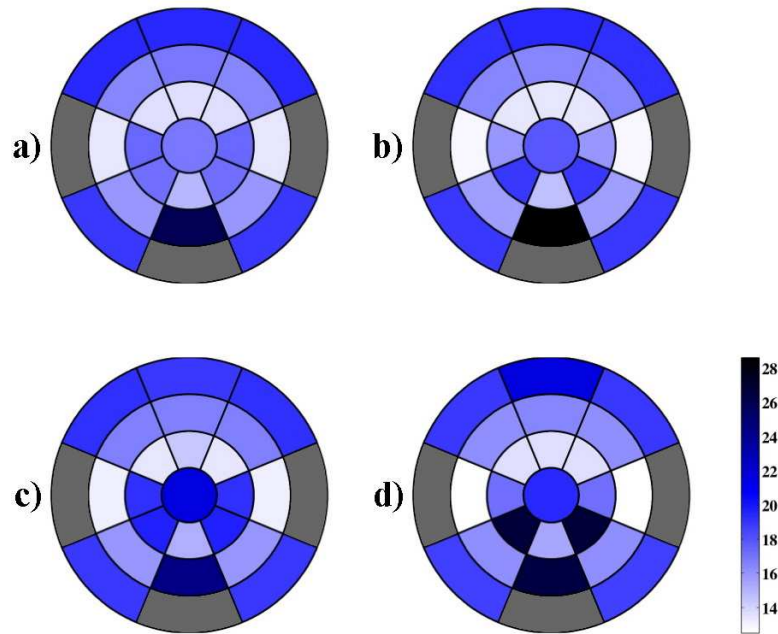
Figure C-12: Spacecraft Terminal Peak Power on Aperture, increase in standard deviation due to disturbances (dB).
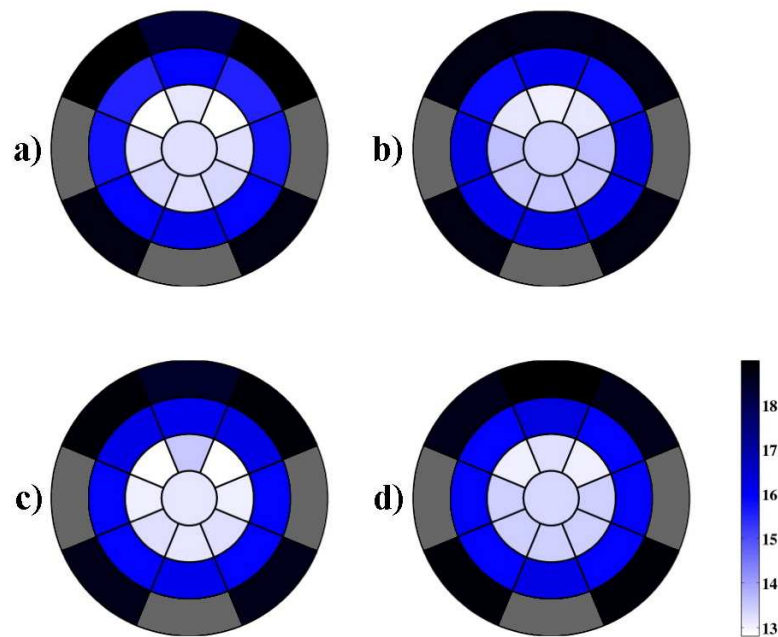
Figure C-13: Aircraft Terminal Peak Power on Aperture, increase in standard deviation due to disturbances (dB).

Table C.1: Spacecraft Terminal Fiber Power, decrease in mean power due to disturbances (dB).

Case	Jitter	Fading	BLE	Azimuth (deg)	Elevation (deg)	Slow Regression		Fast Regression	
						Centroid	Peak	Centroid	Peak
1.0						0.06		0.08	
1.1	x	x	x	0	45	0.61	0.56	0.71	0.82
1.2	x	x	x	45	45	0.64	0.54	0.61	0.80
1.3	x	x	x	90	45	2.61	2.58	1.88	2.81
1.4	x	x	x	135	45	2.97	2.75	2.14	3.00
1.5	x	x	x	180	45	2.88	2.64	2.14	2.93
1.6	x	x	x	0	90	4.17	3.72	3.07	4.00
2.1	x	x	x	0	20	0.67	0.70	0.61	1.35
2.2	x	x	x	45	20	0.86	0.90	0.60	1.37
2.3	x	x	x	90	20	5.80	5.83	5.39	6.10
2.4	x	x	x	135	20	1.95	2.02	1.73	2.10
2.5	x	x	x	180	20	6.27	5.75	5.73	5.64
3.1	x	x	x	0	10	3.26	2.87	1.55	1.99
3.2	x	x	x	45	10	0.75	1.18	0.80	1.11
3.3	x	x	x	90	10	8.24	7.82	7.11	4.86
3.4	x	x	x	135	10	1.31	1.79	1.15	1.47
3.5	x	x	x	180	10	10.47	8.70	8.33	6.07

Table C.2: Aircraft Terminal Fiber Power, decrease in mean power due to disturbances (dB).

Case	Jitter	Fading	BLE	Azimuth (deg)	Elevation (deg)	Slow Regression		Fast Regression	
						Centroid	Peak	Centroid	Peak
1.0						-0.02		0.01	
1.1	x	x	x	0	45	0.86	0.87	0.87	0.76
1.2	x	x	x	45	45	0.80	0.87	0.87	0.78
1.3	x	x	x	90	45	2.39	2.88	2.69	2.60
1.4	x	x	x	135	45	2.41	2.76	2.48	2.50
1.5	x	x	x	180	45	2.35	2.63	2.40	2.52
1.6	x	x	x	0	90	3.61	4.01	3.79	3.81
2.1	x	x	x	0	20	1.04	1.20	0.76	1.06
2.2	x	x	x	45	20	1.25	1.48	0.78	1.11
2.3	x	x	x	90	20	4.26	5.21	4.76	4.82
2.4	x	x	x	135	20	1.75	2.17	1.83	1.63
2.5	x	x	x	180	20	5.36	6.19	6.07	5.56
3.1	x	x	x	0	10	1.81	1.24	0.74	1.22
3.2	x	x	x	45	10	0.69	1.45	0.90	1.15
3.3	x	x	x	90	10	4.30	5.33	4.61	5.52
3.4	x	x	x	135	10	1.12	1.82	1.23	1.46
3.5	x	x	x	180	10	9.19	8.11	8.03	9.36

Table C.3: Spacecraft Terminal Fiber Power, increase in standard deviation due to disturbances (dB).

Case	Jitter	Fading	BLE	Azimuth (deg)	Elevation (deg)	Slow Regression Centroid	Peak	Fast Regression Centroid	Peak
1.0						0.24		0.66	
1.1	x	x	x	0	45	12.17	11.82	12.12	12.47
1.2	x	x	x	45	45	12.14	11.90	11.42	12.11
1.3	x	x	x	90	45	13.72	13.18	13.27	13.50
1.4	x	x	x	135	45	13.85	13.18	13.14	13.31
1.5	x	x	x	180	45	13.62	12.92	12.76	13.02
1.6	x	x	x	0	90	14.13	13.25	13.13	13.19
2.1	x	x	x	0	20	15.41	15.13	15.06	14.64
2.2	x	x	x	45	20	14.82	14.65	14.92	14.55
2.3	x	x	x	90	20	12.48	12.05	12.31	11.71
2.4	x	x	x	135	20	14.52	14.21	14.43	14.25
2.5	x	x	x	180	20	13.17	12.69	13.14	12.61
3.1	x	x	x	0	10	16.44	16.34	16.99	15.87
3.2	x	x	x	45	10	17.70	17.19	17.70	16.13
3.3	x	x	x	90	10	10.52	10.35	11.10	10.32
3.4	x	x	x	135	10	17.12	16.73	17.22	15.94
3.5	x	x	x	180	10	7.54	9.02	9.64	8.50

Table C.4: Aircraft Terminal Fiber Power, increase in standard deviation due to disturbances (dB).

Case	Jitter	Fading	BLE	Azimuth (deg)	Elevation (deg)	Slow Regression Centroid	Peak	Fast Regression Centroid	Peak
1.0						0.57		0.40	
1.1	x	x	x	0	45	5.25	5.24	5.76	5.43
1.2	x	x	x	45	45	5.06	5.29	5.10	5.27
1.3	x	x	x	90	45	6.74	6.31	6.54	6.62
1.4	x	x	x	135	45	6.99	6.60	6.83	6.95
1.5	x	x	x	180	45	6.58	6.32	6.49	6.54
1.6	x	x	x	0	90	6.64	6.07	6.47	6.60
2.1	x	x	x	0	20	8.22	8.06	8.45	8.23
2.2	x	x	x	45	20	7.59	7.78	8.26	8.09
2.3	x	x	x	90	20	6.62	6.41	6.73	6.78
2.4	x	x	x	135	20	7.60	7.77	7.76	7.69
2.5	x	x	x	180	20	6.52	6.37	6.53	6.53
3.1	x	x	x	0	10	10.49	10.34	10.66	10.39
3.2	x	x	x	45	10	10.97	10.79	10.93	10.58
3.3	x	x	x	90	10	8.47	7.83	8.08	7.74
3.4	x	x	x	135	10	10.50	10.43	10.63	10.41
3.5	x	x	x	180	10	3.94	5.23	5.11	4.98

Table C.5: Spacecraft Terminal Power Density on Aperture, decrease in mean power due to disturbances (dB).

Case	Jitter	Fading	BLE	Azimuth (deg)	Elevation (deg)	Slow Regression		Fast Regression	
						Centroid	Peak	Centroid	Peak
1.0						0.08		0.07	
1.1	x	x	x	0	45	0.62	0.54	0.67	0.73
1.2	x	x	x	45	45	0.63	0.54	0.59	0.69
1.3	x	x	x	90	45	2.46	2.33	2.05	2.36
1.4	x	x	x	135	45	2.82	2.42	2.29	1.87
1.5	x	x	x	180	45	2.96	2.48	2.47	2.71
1.6	x	x	x	0	90	4.03	3.38	2.77	3.40
2.1	x	x	x	0	20	0.55	0.59	0.75	1.01
2.2	x	x	x	45	20	0.68	0.73	0.68	1.16
2.3	x	x	x	90	20	5.73	5.74	5.79	6.56
2.4	x	x	x	135	20	1.96	1.87	1.92	2.06
2.5	x	x	x	180	20	0.76	-0.25	2.00	0.54
3.1	x	x	x	0	10	2.79	2.28	1.51	1.49
3.2	x	x	x	45	10	0.60	0.81	0.83	1.08
3.3	x	x	x	90	10	6.55	6.93	6.45	6.47
3.4	x	x	x	135	10	1.22	1.43	1.15	1.75
3.5	x	x	x	180	10	3.79	6.44	3.70	6.66

Table C.6: Aircraft Terminal Power Density on Aperture, decrease in mean power due to disturbances (dB).

Case	Jitter	Fading	BLE	Azimuth (deg)	Elevation (deg)	Slow Regression		Fast Regression	
						Centroid	Peak	Centroid	Peak
1.0						-0.02		0.01	
1.1	x	x	x	0	45	0.30	0.34	0.24	0.19
1.2	x	x	x	45	45	0.27	0.34	0.20	0.21
1.3	x	x	x	90	45	0.00	0.52	0.14	0.25
1.4	x	x	x	135	45	0.11	0.47	0.07	0.21
1.5	x	x	x	180	45	0.12	0.49	0.12	0.26
1.6	x	x	x	0	90	0.09	0.42	0.12	0.11
2.1	x	x	x	0	20	0.50	0.44	0.15	0.31
2.2	x	x	x	45	20	0.61	0.58	0.09	0.29
2.3	x	x	x	90	20	0.21	0.33	0.19	0.13
2.4	x	x	x	135	20	0.13	0.46	0.17	0.12
2.5	x	x	x	180	20	0.12	0.44	0.10	0.06
3.1	x	x	x	0	10	0.63	0.26	0.16	0.19
3.2	x	x	x	45	10	0.04	0.49	0.20	0.30
3.3	x	x	x	90	10	0.15	0.40	0.09	0.37
3.4	x	x	x	135	10	0.01	0.52	0.10	0.17
3.5	x	x	x	180	10	1.67	0.64	0.35	0.40

Table C.7: Spacecraft Terminal Power Density on Aperture, increase in standard deviation due to disturbances (dB).

Case	Jitter	Fading	BLE	Azimuth (deg)	Elevation (deg)	Slow Regression		Fast Regression	
						Centroid	Peak	Centroid	Peak
1.0						0.59		0.78	
1.1	x	x	x	0	45	13.75	13.51	14.30	13.71
1.2	x	x	x	45	45	13.72	13.47	13.38	13.58
1.3	x	x	x	90	45	17.48	15.87	19.08	17.12
1.4	x	x	x	135	45	17.16	18.90	19.68	26.82
1.5	x	x	x	180	45	14.89	14.63	15.10	15.36
1.6	x	x	x	0	90	17.03	17.87	21.72	19.55
2.1	x	x	x	0	20	16.82	16.51	16.69	16.44
2.2	x	x	x	45	20	16.50	16.33	16.64	16.26
2.3	x	x	x	90	20	13.31	12.96	13.15	12.52
2.4	x	x	x	135	20	15.87	15.67	15.92	16.11
2.5	x	x	x	180	20	26.08	28.60	24.45	26.36
3.1	x	x	x	0	10	19.54	19.45	18.94	21.77
3.2	x	x	x	45	10	19.42	19.13	19.21	18.94
3.3	x	x	x	90	10	20.70	18.77	19.47	20.66
3.4	x	x	x	135	10	18.86	18.81	18.95	18.80
3.5	x	x	x	180	10	27.06	20.07	27.20	22.77

Table C.8: Aircraft Terminal Power Density on Aperture, increase in standard deviation due to disturbances (dB).

Case	Jitter	Fading	BLE	Azimuth (deg)	Elevation (deg)	Slow Regression		Fast Regression	
						Centroid	Peak	Centroid	Peak
1.0						0.48		1.34	
1.1	x	x	x	0	45	13.11	13.04	13.54	13.25
1.2	x	x	x	45	45	12.81	13.19	12.89	13.05
1.3	x	x	x	90	45	13.28	13.59	13.01	13.42
1.4	x	x	x	135	45	13.32	13.49	13.22	13.43
1.5	x	x	x	180	45	13.29	13.49	13.15	13.46
1.6	x	x	x	0	90	13.22	13.43	13.19	13.39
2.1	x	x	x	0	20	16.03	16.12	16.19	16.33
2.2	x	x	x	45	20	15.56	15.83	16.20	16.00
2.3	x	x	x	90	20	15.73	16.24	16.03	16.07
2.4	x	x	x	135	20	15.96	16.16	15.95	15.98
2.5	x	x	x	180	20	16.11	16.23	16.19	16.22
3.1	x	x	x	0	10	18.30	18.79	18.43	18.99
3.2	x	x	x	45	10	18.92	18.74	18.85	18.64
3.3	x	x	x	90	10	18.87	18.91	18.76	18.27
3.4	x	x	x	135	10	18.71	18.75	18.70	18.84
3.5	x	x	x	180	10	17.71	18.46	18.50	18.78

Table C.9: Spacecraft Terminal Focal Plane Array Peak Power, decrease in mean power due to disturbances (dB).

Case	Jitter	Fading	BLE	Azimuth (deg)	Elevation (deg)	Slow Regression		Fast Regression	
						Centroid	Peak	Centroid	Peak
1.0						0.00		0.00	
1.1	x	x	x	0	45	0.02	0.02	0.03	0.03
1.2	x	x	x	45	45	0.01	0.02	0.02	0.03
1.3	x	x	x	90	45	0.42	0.52	0.50	0.57
1.4	x	x	x	135	45	0.42	0.53	0.51	0.63
1.5	x	x	x	180	45	0.34	0.48	0.43	0.58
1.6	x	x	x	0	90	0.97	1.24	1.18	1.41
2.1	x	x	x	0	20	0.08	0.07	0.09	0.14
2.2	x	x	x	45	20	0.08	0.09	0.08	0.15
2.3	x	x	x	90	20	1.97	2.37	1.86	2.63
2.4	x	x	x	135	20	0.27	0.33	0.30	0.38
2.5	x	x	x	180	20	2.86	2.96	2.96	3.40
3.1	x	x	x	0	10	1.87	1.40	0.94	1.23
3.2	x	x	x	45	10	0.44	0.47	0.51	0.61
3.3	x	x	x	90	10	3.89	3.91	3.56	3.49
3.4	x	x	x	135	10	0.59	0.68	0.59	0.71
3.5	x	x	x	180	10	7.13	5.80	5.51	5.85

Table C.10: Aircraft Terminal Focal Plane Array Peak Power, decrease in mean power due to disturbances (dB).

Case	Jitter	Fading	BLE	Azimuth (deg)	Elevation (deg)	Slow Regression		Fast Regression	
						Centroid	Peak	Centroid	Peak
1.0						0.00		0.00	
1.1	x	x	x	0	45	0.17	0.25	0.24	0.24
1.2	x	x	x	45	45	0.12	0.22	0.14	0.18
1.3	x	x	x	90	45	0.55	1.00	0.60	0.74
1.4	x	x	x	135	45	0.78	1.18	0.76	0.81
1.5	x	x	x	180	45	0.66	1.08	0.70	0.76
1.6	x	x	x	0	90	1.38	1.86	1.43	1.35
2.1	x	x	x	0	20	0.80	0.77	0.57	0.67
2.2	x	x	x	45	20	0.77	0.75	0.51	0.63
2.3	x	x	x	90	20	1.92	2.05	1.80	1.81
2.4	x	x	x	135	20	0.82	1.00	0.77	0.79
2.5	x	x	x	180	20	1.99	2.16	1.96	2.01
3.1	x	x	x	0	10	1.58	1.51	1.34	1.45
3.2	x	x	x	45	10	1.29	1.56	1.41	1.34
3.3	x	x	x	90	10	2.69	2.93	2.62	2.52
3.4	x	x	x	135	10	1.50	1.75	1.46	1.41
3.5	x	x	x	180	10	4.22	3.36	3.00	2.89

Table C.11: Spacecraft Terminal Focal Plane Array Peak Power, increase in standard deviation due to disturbances (dB).

Case	Jitter	Fading	BLE	Azimuth (deg)	Elevation (deg)	Slow Regression		Fast Regression	
						Centroid	Peak	Centroid	Peak
1.0						0.01		0.85	
1.1	x	x	x	0	45	6.61	6.49	8.89	8.11
1.2	x	x	x	45	45	6.33	6.22	6.79	6.96
1.3	x	x	x	90	45	20.71	20.93	20.93	21.08
1.4	x	x	x	135	45	20.05	20.46	20.41	20.87
1.5	x	x	x	180	45	19.66	20.14	19.85	20.47
1.6	x	x	x	0	90	21.94	22.13	22.21	22.40
2.1	x	x	x	0	20	15.37	14.74	15.58	16.67
2.2	x	x	x	45	20	15.04	15.25	14.91	16.58
2.3	x	x	x	90	20	21.86	21.85	21.68	21.92
2.4	x	x	x	135	20	18.79	19.32	19.03	19.49
2.5	x	x	x	180	20	22.70	22.56	22.59	22.57
3.1	x	x	x	0	10	23.30	22.56	22.16	22.52
3.2	x	x	x	45	10	20.46	20.51	20.65	20.97
3.3	x	x	x	90	10	21.34	21.11	21.42	21.55
3.4	x	x	x	135	10	21.03	21.25	20.96	21.26
3.5	x	x	x	180	10	20.28	20.79	21.06	20.82

Table C.12: Aircraft Terminal Focal Plane Array Peak Power, increase in standard deviation due to disturbances (dB).

Case	Jitter	Fading	BLE	Azimuth (deg)	Elevation (deg)	Slow Regression		Fast Regression	
						Centroid	Peak	Centroid	Peak
1.0						0.07		0.20	
1.1	x	x	x	0	45	22.99	23.83	24.02	23.71
1.2	x	x	x	45	45	21.96	23.65	22.46	22.96
1.3	x	x	x	90	45	26.33	27.21	26.37	26.75
1.4	x	x	x	135	45	27.06	27.49	27.05	27.10
1.5	x	x	x	180	45	26.59	27.25	26.64	26.73
1.6	x	x	x	0	90	27.20	27.30	27.18	27.21
2.1	x	x	x	0	20	27.31	27.23	26.68	27.05
2.2	x	x	x	45	20	27.07	27.08	26.30	26.78
2.3	x	x	x	90	20	27.91	27.89	27.78	27.88
2.4	x	x	x	135	20	27.17	27.61	27.12	27.21
2.5	x	x	x	180	20	28.28	28.35	28.21	28.25
3.1	x	x	x	0	10	29.13	28.93	28.72	28.90
3.2	x	x	x	45	10	28.69	28.92	28.77	28.69
3.3	x	x	x	90	10	28.84	28.80	28.86	28.80
3.4	x	x	x	135	10	28.84	29.06	28.84	28.83
3.5	x	x	x	180	10	28.61	29.02	28.92	29.01

Table C.13: Spacecraft Terminal Acquisition Time in seconds.

Case	Jitter	Fading	BLE	Azimuth (deg)	Elevation (deg)	Slow Regression Centroid	Peak	Fast Regression Centroid	Peak
1.0						0.40		0.40	
1.1	x	x	x	0	45	0.40	1.05	1.00	0.45
1.2	x	x	x	45	45	0.65	3.29	0.40	0.84
1.3	x	x	x	90	45	1.35	0.70	1.69	0.89
1.4	x	x	x	135	45	0.80	2.45	0.60	0.40
1.5	x	x	x	180	45	1.00	1.00	0.85	0.40
1.6	x	x	x	0	90	0.70	0.90	0.65	1.60
2.1	x	x	x	0	20	0.45	0.80	1.00	0.60
2.2	x	x	x	45	20	1.00	1.05	0.60	1.00
2.3	x	x	x	90	20	1.40	1.00	1.34	4.20
2.4	x	x	x	135	20	1.00	0.80	1.80	0.40
2.5	x	x	x	180	20	0.55	1.20	0.65	1.94
3.1	x	x	x	0	10	0.65	1.60	3.19	1.20
3.2	x	x	x	45	10	0.85	1.20	1.29	2.98
3.3	x	x	x	90	10	5.21	1.55	2.25	2.49
3.4	x	x	x	135	10	0.80	0.65	1.09	0.85
3.5	x	x	x	180	10	0.80	1.55	1.55	1.00

Table C.14: Aircraft Terminal Acquisition Time in seconds.

Case	Jitter	Fading	BLE	Azimuth (deg)	Elevation (deg)	Slow Regression Centroid	Peak	Fast Regression Centroid	Peak
1.0						0.26		0.26	
1.1	x	x	x	0	45	0.26	0.30	0.51	0.46
1.2	x	x	x	45	45	0.50	2.75	0.42	0.27
1.3	x	x	x	90	45	0.30	0.30	0.97	0.27
1.4	x	x	x	135	45	0.75	1.84	1.10	0.47
1.5	x	x	x	180	45	1.00	0.65	0.50	0.26
1.6	x	x	x	0	90	0.79	0.68	0.68	1.04
2.1	x	x	x	0	20	0.99	0.86	0.88	0.47
2.2	x	x	x	45	20	0.38	0.64	0.73	0.86
2.3	x	x	x	90	20	1.51	0.35	1.25	4.22
2.4	x	x	x	135	20	1.01	0.84	1.53	0.27
2.5	x	x	x	180	20	0.89	0.50	0.70	1.98
3.1	x	x	x	0	10	0.81	1.54	3.47	1.46
3.2	x	x	x	45	10	1.20	0.30	3.73	2.81
3.3	x	x	x	90	10	34.21	32.32	29.88	12.43
3.4	x	x	x	135	10	3.52	3.33	0.32	3.71
3.5	x	x	x	180	10	3.43	10.14	6.02	3.35

Table C.15: Spacecraft Terminal Maximum State Achieved.

Case	Jitter	Fading	BLE	Azimuth (deg)	Elevation (deg)	Slow Regression		Fast Regression	
						Centroid	Peak	Centroid	Peak
1.0						6		6	
1.1	x	x	x	0	45	6	6	6	6
1.2	x	x	x	45	45	6	6	6	6
1.3	x	x	x	90	45	5	5	5	5
1.4	x	x	x	135	45	5	5	5	5
1.5	x	x	x	180	45	5	5	5	5
1.6	x	x	x	0	90	5	5	5	5
2.1	x	x	x	0	20	6	6	5	5
2.2	x	x	x	45	20	6	6	5	5
2.3	x	x	x	90	20	5	5	5	5
2.4	x	x	x	135	20	5	5	5	5
2.5	x	x	x	180	20	5	5	5	5
3.1	x	x	x	0	10	5	5	5	5
3.2	x	x	x	45	10	5	5	5	5
3.3	x	x	x	90	10	5	5	5	5
3.4	x	x	x	135	10	5	5	5	5
3.5	x	x	x	180	10	5	5	5	5

Table C.16: Aircraft Terminal Maximum State Achieved.

Case	Jitter	Fading	BLE	Azimuth (deg)	Elevation (deg)	Slow Regression		Fast Regression	
						Centroid	Peak	Centroid	Peak
1.0						7		7	
1.1	x	x	x	0	45	7	7	7	7
1.2	x	x	x	45	45	7	7	7	7
1.3	x	x	x	90	45	6	6	6	6
1.4	x	x	x	135	45	6,7	6	6	6
1.5	x	x	x	180	45	6,7	6	6	6
1.6	x	x	x	0	90	6	6	6	6
2.1	x	x	x	0	20	6	6	6	6
2.2	x	x	x	45	20	6,7	6,7	6	6
2.3	x	x	x	90	20	6	6	6	6
2.4	x	x	x	135	20	6	6	6	6
2.5	x	x	x	180	20	6	6	6	6
3.1	x	x	x	0	10	6	6	6	6
3.2	x	x	x	45	10	6	6	6	6
3.3	x	x	x	90	10	4	4	4	4
3.4	x	x	x	135	10	6	6	6	6
3.5	x	x	x	180	10	4	4	4	4

Table C.17: Spacecraft Terminal Link Behavior: n=no drops, f=few drops, o=often, c=chattering between states.

Case	Jitter	Fading	BLE	Azimuth (deg)	Elevation (deg)	Slow Regression Centroid	Peak	Fast Regression Centroid	Peak
1.0						n		n	
1.1	x	x	x	0	45	n	n	n	n
1.2	x	x	x	45	45	n	n	n	n
1.3	x	x	x	90	45	f	n	n	n
1.4	x	x	x	135	45	f	n	n	n
1.5	x	x	x	180	45	f	n	n	n
1.6	x	x	x	0	90	n	n	n	n
2.1	x	x	x	0	20	f	n	nc	nc
2.2	x	x	x	45	20	f	f	nc	nc
2.3	x	x	x	90	20	n	n	n	n
2.4	x	x	x	135	20	f	n	n	n
2.5	x	x	x	180	20	n	n	n	n
3.1	x	x	x	0	10	f	f	n	n
3.2	x	x	x	45	10	n	n	n	n
3.3	x	x	x	90	10	n	f	n	f
3.4	x	x	x	135	10	n	n	n	n
3.5	x	x	x	180	10	o	o	f	o

Table C.18: Aircraft Terminal Link Behavior: n=no drops, f=few drops, o=often, c=chattering between states.

Case	Jitter	Fading	BLE	Azimuth (deg)	Elevation (deg)	Slow Regression Centroid	Peak	Fast Regression Centroid	Peak
1.0						n		n	
1.1	x	x	x	0	45	n	n	nc	nc
1.2	x	x	x	45	45	n	n	nc	nc
1.3	x	x	x	90	45	f	n	nc	nc
1.4	x	x	x	135	45	f	n	n	n
1.5	x	x	x	180	45	f	n	n	n
1.6	x	x	x	0	90	n	n	n	n
2.1	x	x	x	0	20	f	n	nc	nc
2.2	x	x	x	45	20	f	f	nc	nc
2.3	x	x	x	90	20	n	n	n	n
2.4	x	x	x	135	20	f	n	n	n
2.5	x	x	x	180	20	n	n	n	n
3.1	x	x	x	0	10	oc	oc	oc	oc
3.2	x	x	x	45	10	n	f	n	n
3.3	x	x	x	90	10	nc	oc	nc	o
3.4	x	x	x	135	10	n	n	n	n
3.5	x	x	x	180	10	oc	oc	oc	oc

Appendix D

List of Acronyms and Abbreviations

Table D.1: List of acronyms and abbreviations used in this work.

Abbreviation	Description
A/C	Aircraft
AFTS	Airborne Flight Test System
ALEX	Airborne Laser Experiment
BL	Boundary Layer
BLE	Boundary Layer Emulator
BMC	Boston Micromachines Corp.
BS	Beam-Splitter
CFD	Computational Fluid Dynamics
CHEM	Channel Emulator
COM	Center of Mass (centroid)
COTS	Commercial Off-the-Shelf
DAS	Data Acquisition System
dB	Decibel
dBm	Decibel Power (referenced to 1 mW)

DM, MDM	Deformable Mirror
DSM	Disturbance Mirror
DSP	Digital Signal Processor
FFS	Far-Field Simulator
FC/APC	Fiber connector type (angled)
FC/PC	Fiber connector type (planar)
FLA	Fiber Launch Assembly
FOR	Field of Regard
FOV	Field of View
FPA	Focal-Plane Array
FSM	Fast Steering Mirror
GEO	Geostationary Earth Orbit
GeoLITE	GEO Lightweight Tech. Experiment
GPS	Global Positioning System
HW, HWP	Half Wave-Plate
INS	Inertial Navigation System
L	Lens (schematic abbreviation)
LEO	Low Earth Orbit
LN	Lithium Niobate
LUT	Look-Up Table
MEMS	Micro-Electro-Mechanical System
MEO	Mid Earth Orbit
MIT LL	MIT Lincoln Laboratory
OC	Optical Circulator
O/E	Optical-to-Electrical Converter
OFLA	Over-filled Fiber Launch Assembly
OPD	Optical Path Difference
PAM	Point-Ahead Mirror
PAT	Pointing, Acquisition, and Tracking

PBS	Polarization Beam-Splitter
PM, PMF	Polarization-Maintaining Fiber
PSD	Power Spectral Density
PT	Peak Tracking algorithm
PV	Peak-to-Valley (error)
QC	Quad Cell
QW, QWP	Quarter Wave-Plate
RF	Radio Frequency
RMS	Root Mean Square (error)
Rx	Receiver
S/C	Spacecraft (or satellite)
SM	Single-Mode Fiber
SW	Switch (schematic abbreviation)
SWaP	Size, Weight, and Power
Terminal A	Spacecraft Terminal
Terminal B	Aircraft Terminal
TF	Turning Flat
TT	Tracking Testbed
Tx	Transmitter
UAV	Unmanned Aerial Vehicle
WFS	Wave-Front Sensor

Bibliography

[1] Nadya Travinin Bliss. Interactive grid computing at lincoln laboratory. *Lincoln Laboratory Journal*, 16(1), 2006.

[2] BMC. *Picture of Boston Micro Machines Corp. deformable mirror.* www.bostonmicromachines.com, 2007.

[3] J. M. Cicchiello, E. J. Fitzgerald, and E. J. Jumper. Far-field implications of laser transmission through a compressible shear layer. *Proc. SPIE*, 4272:245–249, 2001.

[4] Jay L. Devore. *Probability and Statistics for Engineering and the Sciences*. Thomson, 6th edition, 2004.

[5] Eugene Hecht. *Optics*. Pearson, 4th edition, 2002.

[6] Y. Hsia, W. Lin, H. Loh, and P. Lin. Cfd-based aero-optical performance prediciton of a turret. *Proc. SPIE*, 5792:143–154, 2005.

[7] Stephen G. Lambert and William L. Casey. *Laser Communications in Space*. Artech House, Inc., 1995.

[8] Lockheed-Martin. *Picture of Lockheed Martin U-2 Reconnaissance Aircraft*. www.lockheedmartin.com, 2007.

[9] John A. Maynard and David Begley. Airborne laser communications: Past, present and future. *Proc. SPIE*, 5892:1–13, 2005.

[10] Maurice M. McKinney. Transformational satellite (tsat) communications systems. *Wright Flyer Paper, Air University*, 2007.

[11] Paul McManamon. An overview of optical phased array technology and status. *Proc. SPIE*, 5947, 2005.

[12] Katie M. Morzinski. Characterizing mems deformable mirrors for open-loop operations: High-resolution measurements of thin-plate behavior. *Proc. SPIE*, 6888, 2008.

[13] Alics Nightingale, A. Duffin, Michael Lemmon, Bill Goodwine, and Eric J. Jumper. Adaptive-optic correction of a regularized compressible shear layer. In

Collection of Technical Papers - 37th AIAA Plasmadynamics and Lasers Conference, pages 280–291, 2006.

[14] Northrop-Grumman. *Picture of Northrop Grumman Global Hawk UAV*. www.northropgrumman.com, 2007.

[15] Ronald Parenti and et. al. Modeling the pdf for the irradiance of an uplink beam in the presence of beam wander. *Proc. SPIE*, 6215, 2006.

[16] Frank L. Pedrotti, Leno S. Pedrotti, and Leno M. Pedrotti. *Introduction to Optics*. Pearson, 3rd edition, 2007.

[17] H. M. Presby and et. al. Key elements of high-speed wdm terrestrial free-space optical communications systems. *Proc. SPIE*, 3932, 2000.

[18] Donald Russell, Homayoon Ansari, and Chien-C. Chen. Lasercom pointing acquisition and tracking control using a ccd-based tracker. *SPIE*, 2123, 1994.

[19] FLIR Systems. Thermacam phoenix. Product Brochure, 2004.

[20] J. D. Trolinger and W. C. Rose. Technique for simulating and evaluating aero-optical effects in optical systems. In *AIAA Paper, 42nd AIAA Aerospace Sciences Meeting and Exhibit*, pages 998–1008, 2004.

[21] Linda Wasiczho, Igor I. Smolyaninov, Stuart D. Milner, and Christopher C. Davis. Studies of free space optical links through simulated boundary layer and long-path turbulence. *Proc. SPIE*, 5327:127–135, 2004.

[22] Heinz Willebrand and Baksheesh S. Ghuman. *Free-Space Optics: Enabling Optical Connectivity in Today's Networks*. Sams Publishing, 2001.

[23] James C. Wyant. *Zernike Polynomials*. www.optics.arizona.edu, 2003.

[24] James C. Wyant and Katherine Creath. *Applied Optics and Optical Engineering*, volume XI. Academic Press, Inc., 1992.

[25] George Zogbi and Lawrence Candell. Signal acquisition and timing for a free space laser communications receiver. *Proc. SPIE*, 6457, 2007.

[26] Fazlul R. Zubair and et. al. Laser wavefront propogation through turbulent separated shear layers: Laboratory experiments, computations, and physical modeling. *Proc. SPIE*, 2006.

Vita

Ross A. Conrad was born and raised in the city of Wausau, WI. He graduated from D.C. Everest Senior High School in Schofield, WI, in May 2002. Upon graduation he attended the United States Air Force Academy in Colorado Springs, CO, where he graduated with distinction in May 2006 with a Bachelor of Science in Astronautical Engineering.

Ross was commissioned a Second Lieutenant in the United States Air Force as a developmental engineer. His first assignment was to pursue graduate studies at the Massachusetts Institute of Technology, through a research assistantship with MIT Lincoln Laboratory, for a Master of Science degree in Aeronautical & Astronautical Engineering. Upon graduation in 2008, he will be assigned to the Air Force Research Laboratory, Kirtland Air Force Base, NM.